WELL-CONTROLLED MODIFICATION OF EMISSION KINETICS OF COLLOIDAL SEMICONDUCTOR QUANTUM WELLS

A DISSERTATION SUBMITTED TO
THE GRADUATE SCHOOL OF ENGINEERING AND SCIENCE
OF BILKENT UNIVERSITY
IN PARTIAL FULFILLMENT OF THE REQUIREMENTS FOR
THE DEGREE OF
DOCTOR OF PHILOSOPHY
IN
ELECTRICAL AND ELECTRONICS ENGINEERING

By
Muhammad Hamza Humayun
September 2021

Well-Controlled Modification of Emission Kinetics of Colloidal Semiconductor Quantum Wells
By Muhammad Hamza Humayun
September 2021

We certify that we have read this dissertation and that in our opinion it is fully adequate, in scope and in quality, as a dissertation for the degree of Doctor of Philosophy.

Hilmi Volkan Demir(Advisor)

Vakur Behçet Ertürk

Dönüş Tuncel

Nihan Kosku Perkgöz

Talha Erdem

Approved for the Graduate School of Engineering and Science:

Ezhan Karaşan
Director of the Graduate School

ABSTRACT

WELL-CONTROLLED MODIFICATION OF EMISSION KINETICS OF COLLOIDAL SEMICONDUCTOR QUANTUM WELLS

Muhammad Hamza Humayun
Ph.D. in Electrical and Electronics Engineering
Advisor: Hilmi Volkan Demir
September 2021

Colloidal quantum wells (CQWs) belong to an important quasi-2-dimensional sub-family of semiconductor nanocrystals. Thanks to their uniquely tight quantum confinement of only few monolayers extending across their vertical thickness, CQWs possess giant oscillator strength, substantially increasing their absorption cross-section along with their large lateral size expanded over tens to hundreds of nm's on one side. These together make CQWs excellent candidates for light-harvesting applications. In this thesis, to utilize CQWs' superior light-harvesting capability, we investigated the alteration and control of photoluminescence decay lifetimes of the CQWs in a variety of hybrid absorbing systems. In particular, we proposed and demonstrated the nonradiative energy transfer from strongly-absorbing CQWs to indirect-bandgap bulk semiconductors as weak absorbers, e.g., bulk silicon. To this end, we systematically studied and showed the well-controlled modification of the emission kinetics of these CQWs that are self-assembled into a single-layer all-face-down oriented ensemble in the vicinity of silicon with a fine-tuned dielectric separator (of thickness d). We found the Förster resonance energy transfer (FRET) to be the chief underlying mechanism for the observed modifications in the emission kinetics of the CQWs, which we further modeled and explained using full electromagnetic solutions. We showed that the rate of the resultant energy transfer from these CQWs to the bulk silicon scales slowly with d^{-1} in space. Finite element method (FEM) based computation revealed that this inverse relationship is caused by the delocalization of the electric field in the CQW layer and the substrate due to strong in-plane dipoles present in the CQWs. To address the shortcomings of silicon-based photo-detecting platforms, in a proof-of-concept hybrid device we fabricated, we experimentally demonstrated that the photosensitization using such a single-layer CQW-film enhances the photocurrent collected in the silicon by up to 3-folds. The findings in this thesis are expected to help further exploit the amazing light-harvesting

potential of CQWs in optoelectronic applications.

Keywords: Semiconductor nanocrystals, colloidal quantum wells, nanoplatelets, energy transfer.

ÖZET

KOLLOİDAL YARIİLETKEN KUANTUM KUYULARI IŞIMA KİNETİKLERİNİN İYİ KONTROL EDİLEBİLEN DEĞİŞİKLİĞİ

Muhammad Hamza Humayun
Elektrik ve Elektronik Mühendisliği, Doktora
Tez Danışmanı: Hilmi Volkan Demir
Ekim 2021

Kolloidal kuantum kuyuları (KKK'ler), yarıiletken nanokristallerin önemli bir neredeyse-2 boyutlu alt ailesidir. Dikey kalınlıkları boyunca uzanan sadece birkaç tek katmanın benzersiz sıkı kuantum sınırlamaları sayesinde, KKK'ler çok yüksek osilatör gücüne sahiptirler ve bir tarafta onlarca ila yüzlerce nm arasında genişleyen büyük yan boyutlarıyla birlikte soğurma kesitlerini önemli ölçüde artırmaktadırlar. Bu özellikler KKK'leri ışık hasatı uygulamaları için mükemmel adaylar haline getirmektedir. Bu tezde, KKK'lerin üstün ışık toplama kapasitelerinden faydalanmak için, çeşitli melez soğurma sistemlerinde, KKK'lerin fotolüminesans ışıma sürelerinin farklılaştırılması ve kontrolü araştırılmıştır. Özellikle, güçlü soğurabilen KKK'lerden, zayıf soğurucular olan dolaylı bant aralığına sahip yığın yarıiletkenlere (örneğin, yığın silisyum) ışımasız enerji aktarımı önerilmiş ve gösterilmiştir. Bu amaçla, ince ayarlı bir dielektrik ayırıcı (d kalınlığında) ile silisyum yakınında tek katmanlı, tamamen yüzü aşağı dönük bir topluluğa kendiliğinden istiflenen bu KKK'lere ait ışıma kinetiklerinin iyi kontrol edilen modifikasyonları çalışılmış ve gösterilmiştir. Förster rezonans enerji aktarımı (FRET), tam elektromanyetik çözümler kullanarak da modellediğimiz ve açıkladığımız KKK'lerin ışıma kinetiğinde gözlemlenen değişikliklerin altında yatan temel mekanizma olarak bulunmuştur. Bu KKK'lerden yığın silisyuma elde edilen enerji transferinin hızının uzayda d^{-1} ile yavaş yavaş ölçeklendiği gösterilmiştir. Sonlu elemanlar yöntemine (FEM) dayalı hesaplama, bu ters orantılı ilişkinin, KKK katmanındaki elektrik alanının ve KKK'lerde bulunan güçlü düzlem içi dipoller nedeniyle alttaşın delokalizasyonundan kaynaklandığını ortaya koymuştur. Silisyum tabanlı foto-algılama platformlarının eksikliklerini gidermek için, ürettiğimiz bir kavram kanıtı melez cihazda, böyle bir tek katmanlı KKK filmi kullanılarak ışığa duyarlılaştırmanın silisyumda toplanan fotoakımı 3 kata kadar arttırdığını deneysel olarak gösterilmiştir. Bu tezdeki bulguların,

optoelektronik uygulamalarda KKK'lerin şaşırtıcı ışık toplama potansiyelinden daha fazla yararlanmaya yardımcı olması beklenmektedir.

Anahtar sözcükler: Yarıiletken nanokristaller, kolloidal kuantum kuyuları, nanolevhalar, enerji transferi.

Acknowledgement

As I approach the end of my Ph.D., I would like to thank all the people who have played a part in my journey. It has been an interesting ride that would not have been possible without the support of many people who I would like to acknowledge here.

Foremost, I would like to express my deepest gratitude to my supervisor Prof. Hilmi Volkan Demir for continuous support and encouragement. I would like to thank Prof. Demir for his patience and understanding, and most importantly for believing in me and making me a part of the Demir Research Group. I would like to thank my thesis committee members: Prof. Behçet Vakur Ertürk, Assoc. Prof. Dönüş Tuncel, Assoc. Prof. Nihan Kosku Perkgöz, and Assist. Prof. Talha Erdem for their time and guidance.

I also wish to acknowledge the important role played by the Higher Education Commission (HEC) of Pakistan. HEC helped me to finance my Ph.D. and allowed me to come to Turkey and study at such a prestigious university. I am highly grateful to them for that.

My sincere thanks to Özgün Akyüz and Emre Ünal for the technical support they provided. I also appreciate the help of Duygu Kazancı for assisting in addressing the administrative issues. I would like to thank the UNAM crew for the training and for helping me overcome technical issues in devices' handling. I wholeheartedly thank all the past and present members of the Demir Research Group, Dr. Pedro Ludwig Hernández-Martínez, Dr. Yusuf Keleştemur, Dr. Kıvanç Güngör, Dr. Savaş Delikanı, Dr. Manoj Sharma, Dr. Onur Erdem, Dr. Yemliha Altıntaş, Dr. Negar Gheshlaghi, Dr. Nina Sheremet, Dr. Volodymyr Sheremet, Dr. Satish Kumar, Dr. Betül Canımkurbey, Nima Taghipour, Didem Dede, Sina Foroutan-Barenji, Furkan Işık, Farzan Shabani, Ibrahim Tanrıover, Mustafa Sak, Ulviyya Quliyeva, Hamed Dehghanpour Baruj, Joudi Maskoun, Bilge Yağcı , Muhammad Ahmad, Taylan Bozkaya, Iklim Yurdakul, Rumon Miah, Ahmet Tarık Işık, Taha Haddadi, and Mohsin Waris. I would like to extend my honest gratitude to Dr. Hernández-Martínez for his patience with me in my simulation work, Onur for mentoring, Negar and Yemliha for encouraging me when the going got tough, Bilge for being ever ready to help in any capacity, Sina

for enlightening talks and weekend strolls, Hamed for agreeing to be my gym trainer, Farzan for his amazing sermons, and last but not least Ahmad for his companionship.

Finally, I would love to express my very profound gratitude to my beloved parents, my grandfather who kept praying for my success till his last breath, my wife, and my siblings for unconditional emotional support and continuous encouragement throughout the years.

Contents

List of Figures

List of Tables

Chapter 1

Introduction

Colloidal quantum wells (CQWs) belong to a family of solution-processed atomically-flat semiconductor nanocrystals (NCs) that have emerged as a potential substitute to the fundamental building block in contemporary photonics technologies: epitaxial thin-film semiconductors. Mostly in the last decade, extensive research on colloidal thin-film synthesis techniques has opened up opportunities for these photonic materials in optoelectronics field including photovoltaics [1], displays [2], lasers [3–7], LEDs [8–10], and bioimaging and medicine [11–14].

CQWs possess a high absorption cross-section and photoluminescence (PL) quantum yield possibly approaching unity for certain chemical routes and heterostructures. These characteristics make them suitable candidates as efficient exciton donors, creating an opportunity for us to explore energy transfer mechanisms in their hybrid structures. There is also a lack of research on the modification of emission kinetics of the CQWs using bulk-system energy transfer and plasmonic interactions. This thesis aims to show the modified emission kinetics of CQWs by using the anisotropy of CQWs to our advantage to transfer energy to weakly-absorbing bulk silicon via Förster resonance energy transfer (FRET). Also, we study the change in decay rates of these CQWs using plasmonic nanostructures.

This chapter will present an overview of this thesis work. We will start by providing the background, followed by the research objective and significance, and finish the chapter by outlining the structure of this thesis.

The 1980s were the decade that saw the birth of the science of colloidal semiconductor NCs [15, 16]. In three decades, immense research in the synthesis of these solution-processed NCs has expanded our comprehension and afforded us the control over the growth and emerging properties of the NCs. Advances in colloidal synthesis resulted in the formation of NCs with different shapes. The synthesis of monodisperse spherical NCs, also known as colloidal quantum dots (CQDs), was achieved in the early 1990s [17]. The synthesis of nanorods was reported a few years later [18]. The synthesis of CQWs, also known as semiconductor nanoplatelets (NPLs), was developed in the late 2000s [19]. Among all, cadmium chalcogenides (CdE, with E = sulfide, selenide, and telluride) have been the most researched semiconductor NCs [20–23].

CQWs are the quasi-two dimensional atomically-flat NCs. CQWs possess strong one-dimensional vertical confinement with lateral dimensions extended in the range of tens of nanometers [24]. Excitons in CQWs are typically confined only in one dimension because usually only this vertical thickness is smaller than the exciton Bohr radius [25]. CQWs exhibit fascinating optical properties including narrow emission linewidth [26], high photoluminescent quantum yield (PLQY) [27, 28], high absorption cross-sections [24, 29], giant oscillator strength [30,31], large exciton binding energy, and a lower rate of Auger recombination [32,33]. Heterostructuring can further tune the electronic structure of these CQWs. Vertical shell growth and crown growth in lateral directions have made it possible to synthesize their complex heterostructures such as core/crown/shell and core/multi-crown shell, which is unique to CQWs [34]. Further use of alloy-gradient shells and metal doping can be used to tune the optical properties making these cadmium chalcogenide-based CQWs and their heterostructures promising candidates for photonic applications [35].

Energy transfer-based hybrid photovoltaic devices, where these NCs act as light harvesters, define a promising NC-based research direction [36–39]. In such

devices, one component is characterized by its ability to interact with the light strongly, and the other is responsible for charge transport. The excitation energy funnels to the charge collecting component via electromagnetic (EM) interaction [40]. CQWs can be an excellent choice as a donor because these fluorophores are strong absorbers of light and, with bandgap tuning, can cover the visible spectrum.

The EM interaction responsible for energy transfer could result in nonradiative energy transfer (NRET) and radiative energy transfer (RET) [38]. NRET is a near-field EM interaction. One of its types is Förster resonance energy transfer (FRET) that occurs through dipole-dipole coupling between donor-acceptor pair [41, 42]. In FRET, oscillating transition dipole in the donor induces a transition dipole in the acceptor without emission of light. While FRET relies on Coulombic interaction, there is another NRET mechanism known as Dexter energy transfer (DET) which occurs through electron interactions between donor-acceptor pair [43]. In DET, wavefunctions of donor and acceptor species overlap resulting in electrons and holes tunneling from donor to acceptor [42]. On the other hand, RET involves the donor exciton decaying into photonic modes in the acceptor layer [44]. In RET, the donor emitter fluoresces and the emitted photon then excites the acceptor. D. L. Dexter was the first who proposed producing electron-hole pairs in semiconductors using NRET in 1979 [45]. The energy transfer also modifies the emission kinetics of the excited emitter dipole [46–48].

Another way of engineering the emission decay of NCs is through using metallic nanoparticles (NPs) [49]. Metallic nanoparticles can dramatically increase the interaction between light and matter at the dimensions much smaller than the wavelength of the EM wave. The light generates localized surfaces plasmon resonance (LSPR) in these NPs, resulting in an EM field enhancement in the vicinity of NPs [50]. The enhanced EM can affect the emission kinetics of a nearby fluorophore [51, 52].

The enhancement of fluorescence using metal was first reported in the 1970s [53]. Metal nanostructures both absorb and scatter light. PL of NCs is enhanced when its emission peak lies in the spectrum range of metal NP dominated by

scattering and is quenched when it lies in the spectrum range dominated by absorption and in the close proximity [54]. Whether the emitter's fluorescence may be quenched or enhanced also depends on the separation distance between the emitter and metallic nanoparticles (NPs). Generally, PL can be quenched when in contact or proximity (< 5 nm) of the metal surface and can be enhanced when moved beyond 5 nm [55–57].

Studies involving QDs as an energy donors with different acceptor platforms have previously been carried out [38–40, 58]. CQWs are likely to outperform QDs as energy donors because NPLs possess higher intrinsic absorption cross-sections [59]. So far, the energy transfer studies with CQWs involved have focused on the 2D-2D hybrid structures [60–62]. We have not come across a previous report where energy transfer from CQWs to a 3D acceptor structure was studied. Also, while the metal enhanced fluorescence has been studied for other NCs [63–67], little research has taken place to modify emission kinetics of CQWs using metal nanostructures. These studies could be beneficial for CQW-based nanophotonic applications. In particular, a study based on the FRET in a 2D-3D hybrid structure, with silicon as the exciton-sinking medium, has not been explored. Silicon is generally used for building solar cells and photodetectors. Silicon has poor light absorption. Sensitization with CWQs can substantially enhance the absorption of silicon.

In this thesis, we studied energy transfer in a 2D-3D hybrid structure involving CQWs acting as an energy donor and silicon acting as an exciton acceptor medium. We used the self-assembly deposition technique to gain control over CQWs' orientation. FRET was shown to be the effective energy transfer mechanism involved up to a separation of 50 nm, modifying the emission kinetics of CQWs in a controlled way. We found the energy transfer rate to be varying slowly with the electric field delocalization in the donor and acceptor regions. We also demonstrated enhancement of photocurrent due to CQWs sensitization. Also, we studied plasmon-exciton interaction using a hybrid system comprising CQWs (as an exciton source with high exciton binding energy) and plasmonic structures. We used random nano-islands and periodic arrays to observe the modification in the emission kinetics of these CQWs.

1.1 Outline of the Thesis

This thesis work is organized as follows:

In Chapter 2, we introduce and explain all the underlying basic material background and physics concepts that were used in this thesis. This includes a brief introduction of NCs. Then we discuss the properties of CQWs. We also discuss the basics of energy transfer and finally we introduce the light-matter interaction with a focus on plasmonics and how plasmonics can be used to enhance the light-matter interaction.

In Chapter 3, we present different fabrication tools that we used in this thesis. We briefly explain the techniques used to fabricate our structures including thermal evaporation, rapid thermal annealing, and electron beam lithography. We also discuss optical characterization tools including steady-state and time-resolved spectroscopy used to analyze emission kinetics of our structures.

In Chapter 4, we show our results from our journal paper on FRET from CQWs to bulk silicon. In this study, we used the self-assembly technique to deposit CQWs in all-face-down orientation on our substrate using alumina spacing to study distance-dependent energy transfer.

In Chapter 5, we present the results from our study involving distance-dependent modification of emission kinetics of CQWs using gold nano-islands and periodic patterned silver arrays.

Chapter 6 concludes our thesis where we sum up our thesis work and highlight the possible future directions.

Chapter 2

Scientific Background

2.1 Colloidal Semiconductor Nanocrystals

Inorganic semiconductors are crucial building blocks for optoelectronic devices. They offer superior light absorption, carrier mobilities, and photostability. However, their fabrication processes involve a high thermal budget, high cost, and compatibility issues with substrates. Low-dimensional semiconductor materials, which are solution-processed, have emerged as an inexpensive alternative. Optoelectronic device fabrication using novel materials like organic semiconductors [68], carbon nanotube [69], colloidal quantum dots [17], nanowires [18, 70], and nanoplatelets [19] is possible now. The history of colloidal nanosized inorganic materials goes back to the 19th century; however, current nanoscience with nanocrystals (NCs) started in the early 1980s [16]. Colloidal synthesis of inorganic nanostructures has seen impressive progress in the last few years. It is emerging as a new branch of synthetic chemistry with innovative methods to materials design. By bandgap engineering of the nanostructures using precise tuning of shape and size, and by introducing heterostructuring during synthesis, we can control the spatial localization of electrons and holes within the NCs [71]. The NC form can be tailored from almost spherical to highly anisotropic by gaining expertise in growth kinetics. Colloidal synthesis allows us to prepare a wide range

of multi-component nanostructures. The colloidal synthesis also allows to manipulate and tune the wavefunctions, plasmonic resonances, spin, and other material properties to make novel functional blocks for optoelectronic applications.

NCs are tiny crystals made up of hundreds to a few thousand atoms. These crystals belong to a size regime that manifests quantum confinement effect. The quantum confinement produces quantization of the electron and hole states. For this reason, NCs are also referred to as artificial atoms. The bandgap of semiconductor NCs changes systematically with their size.

The effect of quantum confinement on the material is exhibited in the semiconductor energy band diagram. For a bulk semiconductor, an E-K diagram is continuous, as shown in Figure 2.1a. But in the case of semiconductor NCs, due to quantization, energy levels are discretized as shown in Figure 2.1b [72]. In the case of these NCs, allowed transitions are limited. The energy bandgap is increased in this scenario because interacting electrons and holes occupy higher energy states. The quantum confinement effect prevails when the physical dimensions become comparable to the Bohr radius of semiconductor material [73]. An exciton in a semiconductor resembles a hydrogen atom. This is because exciton, which is a quasi-particle, is an electron-hole pair bound via Coulomb attraction. For bulk semiconductors, the exciton energy $E_{excition}$ and Bohr radius a_B of the exciton are found as follows:

$$E_{exciton} = \frac{1}{4\pi\varepsilon_0}\frac{\mu e^4}{2\varepsilon^2\hbar^2} \tag{2.1}$$

$$a_B = 4\pi\varepsilon_0\frac{\varepsilon\hbar^2}{\mu e^2} \tag{2.2}$$

where μ is the reduced effective mass of the electron-hole pair, e is the elementary charge, ε is the dielectric constant of the semiconductor medium, ε_0 is the permittivity of free space, and $\hbar$ is the reduced Planck's constant. The binding energy of the carrier is increased when it is restricted in a physical space smaller than its defined Bohr radius. For example, under 1D confinement, exciton binding energy is increased by fourfold compared to the bulk exciton energy in Equation 2.1. Bohr radius due to the 1D confinement is reduced to half its bulk Bohr radius value.

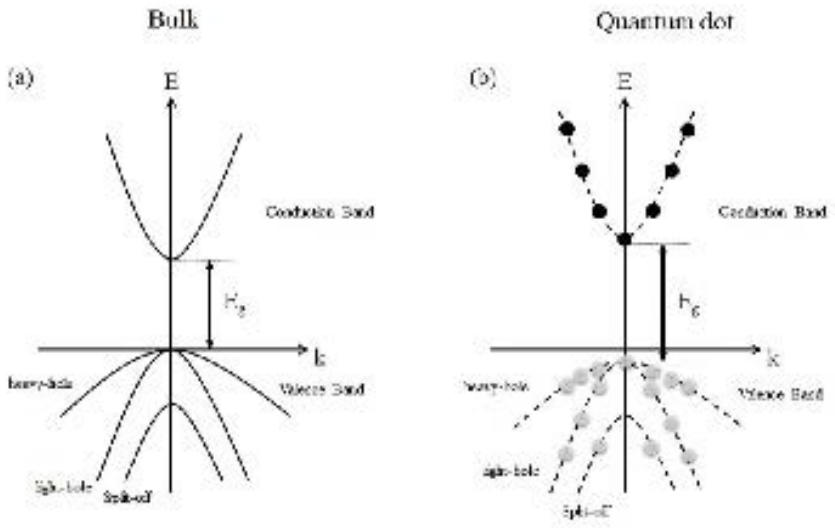

Figure 2.1: E-k diagram of (a) a bulk semiconductor and (b) a quantum dot.

The electronic structure of semiconductors is closely related to the optical properties of the semiconductors including their absorption and emission. The energy bandgap can tell us whether the material is an insulator, a metal, or a semiconductor. From the E-k diagram, we can find out about the nature of the bandgap, whether it is direct or indirect. The shape of energy bands can be used to find effective mass and density of states. These details can be used to estimate whether optical transitions, such as absorption and emission, are permissible or not and the oscillator strength of these optical transitions.

One parameter of critical importance for these optical transitions is the density of states (DOS). The optical properties of these NCs can be understood by understanding the DOS of carriers in these confined nanostructures. In solid-state physics, a system's density of states (DOS) describes the number of distinct states available to a particle to occupy at a given energy level [74]. The number of different states corresponding to given energy strongly depends on the dimensionality of the system (Figure 2.2) [75]. In three-dimensional space (3D), an electron with the same speed but pointing at any direction on a sphere will have

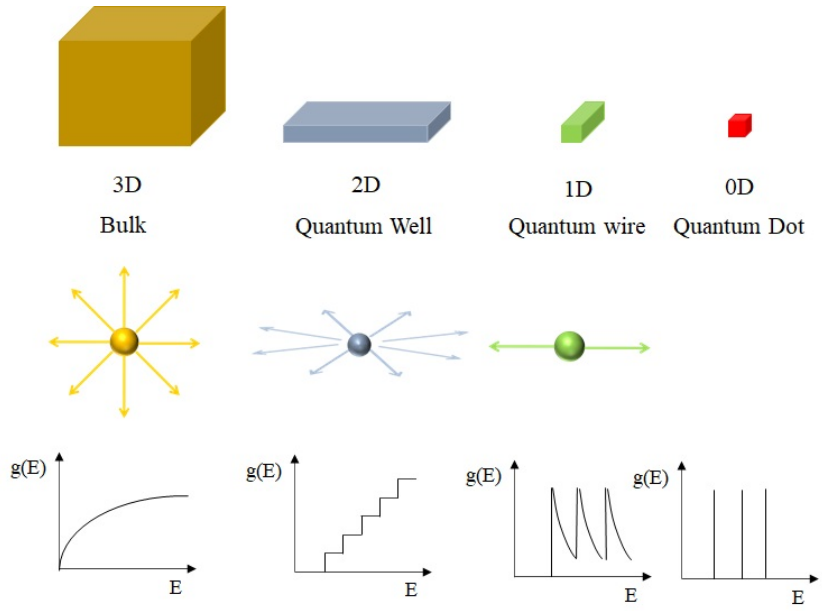

Figure 2.2: Density of states vs. dimensionality of materials.

the same energy. The DOS for a bulk semiconductor is given as:

$$g_{bulk}(E) = \frac{\sqrt{2m^3(E - E_g)}}{\pi^2\hbar^3} \tag{2.3}$$

where E_g is the bandgap of the material, and m is the effective mass of the electron. In bulk semiconductors, DOS varies with $^1/_2$ power dependence on the energy. In 2D space, the available states form a circle of directions and are given as:

$$g_{2D}(E) = \frac{m}{\pi\hbar^2} \tag{2.4}$$

where DOS in 2D is independent of the energy. In 1D space, there are only two distinct possibilities to have the same energy, and DOS is given as:

$$g_{1D}(E) = \frac{1}{\pi\hbar}\sqrt{\frac{m}{2(E - E_g)}} \tag{2.5}$$

which shows the inverse square root energy dependence of 1D DOS. In 0D, carriers are confined in all directions, and DOS is given as delta functions at the quantized energies. Both absorption and emission processes in quantum emitters are dependent on the DOS and thus on the dimensionality of the quantum confinement.

2.1.1 Colloidal Quantum Wells

Colloidal Quantum Wells (CQWs), also known as nanoplatelets (NPLs), are quasi-2D flat semiconductor NCs. Their unique feature is their vertical thickness, consisting of a few discrete number of monolayers (MLs). These atomically flat NPLs have "magic-sized" vertical thickness (e.g., 3,4 and 5 MLs). NPLs are confined in only one direction, and their lateral dimensions can range to tens of nanometers (Figure 2.3) [19].

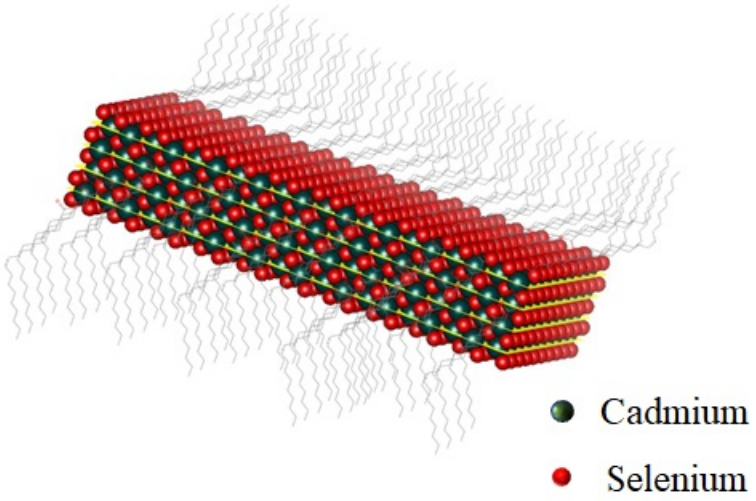

Figure 2.3: A schematic representation of a 4 ML CdSe NPL with an additional Se layer.

The atomic precision present enables the synthesis of monodisperse ensembles. Monodispersity reduces the inhomogeneous broadening and enables NPLs to yield very narrow emission linewidths [30]. Also, NPLs display smaller Stoke's shift as compared to quantum dots. In QDs, we can have practically continuous spectral tuning by varying the QD radius. But this continuous spectral tuning is not possible in NPLs. Instead, NPLs have discretized increments with the addition of MLs. Figure 2.4 shows the photoluminescence (PL) emission spectra of 3, 4, and 5 MLs of CdSe core NPLs. These NPLs have their emission peaks at 463, 513, and 551 nm, respectively.

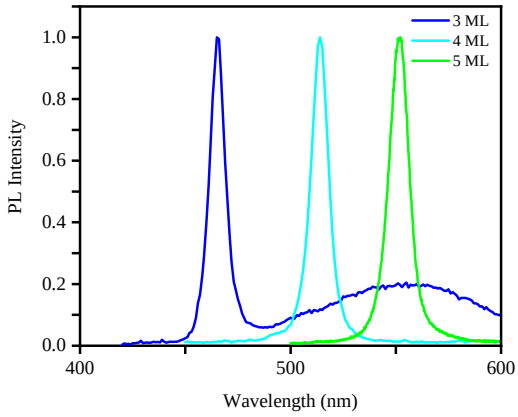

Figure 2.4: PL emission spectra of 3, 4, and 5 ML thick CdSe nanoplatelets.

Figure 2.5 shows the absorption spectrum of 4 ML CdSe NPLs. We can see the peaks corresponding to the heavy hole, light hole, and split-off states in the absorption spectrum.

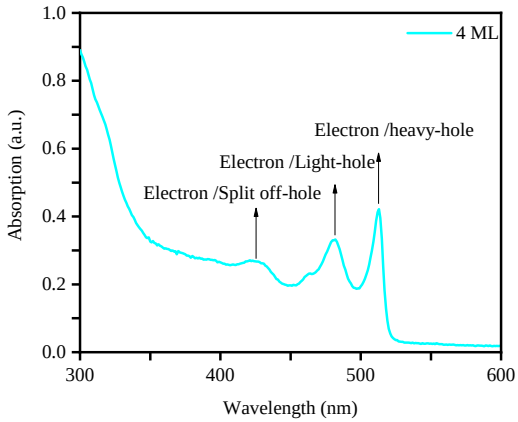

Figure 2.5: Absorption spectra of 4 ML thick CdSe NPLs.

The excitonic properties of NPLs can be further tailored by synthesizing heterostructured NPLs [76]. To date, different architectures have been synthesized (Figure 2.6) [77–79]. These heterostructures offer improved optical properties—for example, the growth of crown results in increased absorption cross-section. The growth of the shell extends the fluorescence lifetime as well as stability.

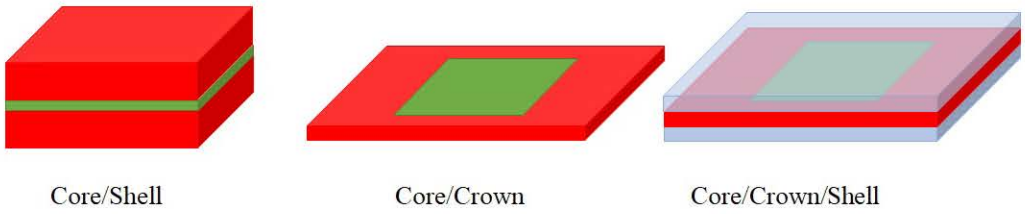

Figure 2.6: Schematic image of different heterostructures of NPLs.

2.2 Deposition Techniques of Colloidal Quantum Wells

Colloidal quantum wells can be deposited using traditional techniques such as drop-cast and spin-coating. However, forming a uniform layer of CQWs on the substrate with full substrate coverage is not easy. Nor do these conventional techniques provide us with control over the orientation of the deposited NPLs. Using these techniques, the deposited NPLs will have mixed orientations. There is a self-assembly method developed in our group which addresses the issues mentioned above. This section will briefly discuss the spin-coating technique and self-assembly process as these were used in this thesis work.

2.2.1 Spin-Coating Method

Spin coating is a deposition technique for making thin-film coating on a flat substrate. In this technique, a substrate is rotated at high speeds and a solution with known particle concentration is dropped into the center of the substrate. Spin coating stages are shown in Figure 2.7. The thickness of the deposited film depends on the following parameters:

- Rotation speed,
- The solution viscosity,
- The spinning time and

- The solvent evaporation time.

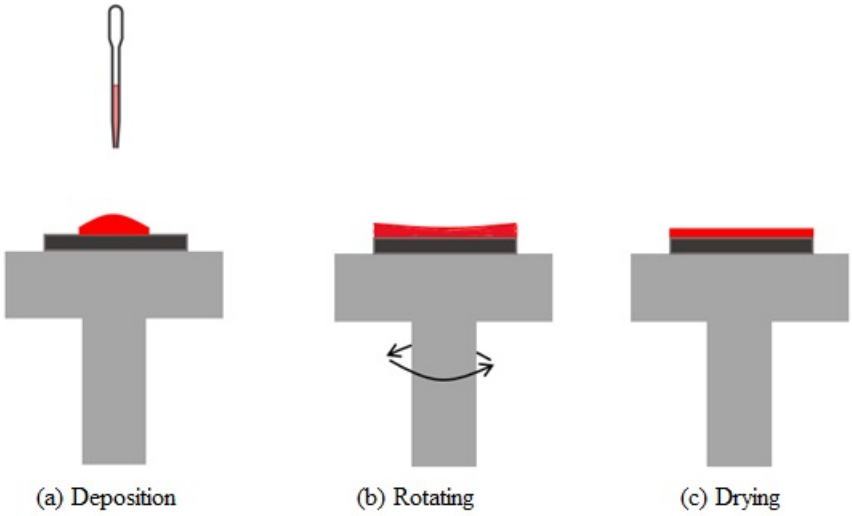

Figure 2.7: Stages in thin-film deposition using spin-coating.

The main advantage of the spin-coating technique is that thin layers can be deposited easily and quickly. However, one disadvantage of this technique is that it is impossible to create ultra-thin films (less than 10 nm). Also, most of the material is thrown off the substrate. About 2–5% of the material is distributed onto the substrate. In the NPL-plasmonic coupling study, we opted for spin-coating because of the simplicity of the technique. Both quartz and silicon substrates were used. We observed that more uniform thin films were produced with this technique when the solvent used was toluene.

As already mentioned, various independent factors are involved in spin-coating, which raises a question regarding reproducibility. In one of the studies, we were interested in depositing a single monolayer of CQWs (about 5 nm thick) with full surface coverage and complete control over the orientation. The spin coating technique was not possible, which led us to deploy a different deposition method known as self-assembly procedure that will be briefly explained in the next section.

2.2.2 Self-Assembly Method

In this thesis work, we adopted self-assembly to study the energy transfer from NPLs to the silicon substrate [80]. The prime reason for choosing this method was that it allowed us to deposit NPLs with uniform single monolayer thickness throughout the sample. Also, with this deposition methodology, we were sure about the orientation of the deposited NPLs [81]. Unlike spin-coating, with this procedure, we can deposit NPLs in all facing-down configuration.

The schematic is illustrated in Figure 2.8. The recipe we used was as follows: The substrates were placed in a Teflon well with a tilt angle of $\sim 10^{\circ}$. The well was then immersed in the subphase of diethylene glycol (DEG). 25 μL of NPL solution in hexane was then dropped onto the DEG surface. Upon the complete evaporation of the hexane, one drop of silicone oil dissolved in hexane was dropped onto the DEG surface to compress the NPL film [82]. This step was to ensure that there were no voids present in the NPL film. The DEG was then slowly drained with the help of a peristaltic pump at a very slow rate of 50 μL/min. After the draining was complete, the samples were put under vacuum to be completely dried to ensure no residual DEG droplets were present on the top surface of the substrate.

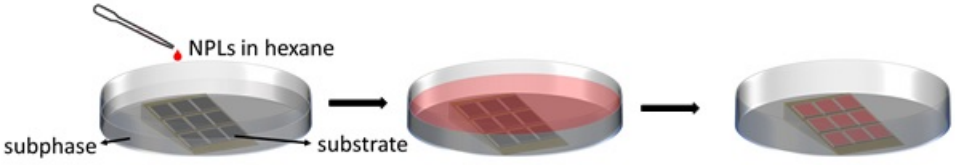

Figure 2.8: Schematic illustration of self-assembly of NPLs at the liquid-air interface. Diethylene glycol subphase was used as the subphase, which was drained by the peristaltic pump to transfer NPLs on the substrates. Reproduced with permission. [83] Copyright 2021, Wiley

NPLs are usually dispersed in a non-polar organic solvent such as hexane. In our work, the colloidal solution was dropped onto a polar liquid subphase denser than the solvent, e.g., water and diethylene glycol. NPLs are capped with organic ligands. Hence neither NPLs nor solvent can dissolve in the subphase. Therefore, the NPL solution spreads across the surface of the polar liquid. After the

evaporation of the hexane, NPLs were left as a thin film on the liquid interface (Figure 2.9). The subphase is slowly drained to transfer these NPLs onto solid substrates. The residual subphase between the substrates and the NPL membrane is evaporated by putting it under vacuum. By tuning the amount of NPL solution dropped, domains with controlled NPL orientation, covering a few square millimeters, were created. This area can be extended up to tens of square centimeters using a surfactant (silicone oil). When silicone oil is added, the domains get compressed, reducing the crack formation and voids during the transfer process.

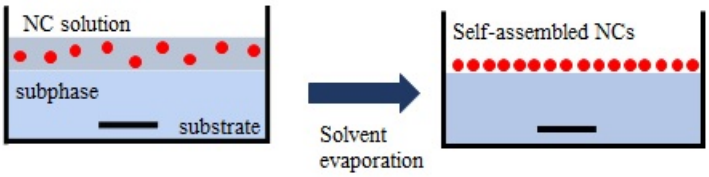

Figure 2.9: Schematic illustration of the formation of self-assembled NCs on the subphase interface.

In this approach, we exploit surface tensions and polarities of the subphases to control the NPL orientation on the interface. Paik *et al.* studied the orientation of self-assembled GdF_3 platelets with glycol-type subphases. They observed that vertically oriented platelets were deposited with the ethylene glycol, which was the most polar solvent they used. As the solvent polarity was weakened, platelets formed a face-down oriented assembly. Recently it has been reported that even solvent evaporation rate affects the CQW orientation. According to reported results, fast evaporation supports the face-down CQW assembly, whereas slow evaporation leads to edge-up assembly.

To summarize, several factors can influence the orientation of the CQW thin film, such as choice of the subphase, the evaporation rate, the solvent used for dispersing the NPLs, and the type of ligands attached to the NPLs. There are still investigations ongoing to understand the mechanisms involved fully. In this study, we deposited a complete, single, close-packed monolayer of face-down oriented NPLs to study energy transfer from them.

2.3 Energy Transfer Mechanisms

In the donor-acceptor system, an excited donor can transfer energy to the acceptor through three different processes and return to the ground state (Figure 2.10). Those are: (1) Dexter energy transfer (DET) [43], (2) Förster (or fluorescence) resonance energy transfer (FRET) [41,84], and (3) radiative energy transfer (RET) [48]. DET and FRET are nonradiative energy transfer (NRET) processes and, hence, produce fluorescence quenching. In DET, electron exchange between molecules takes place. DET requires very close proximity (<1 nm) between the two systems, requiring wavefunction overlap [42]. Electrons and holes are transferred to the acceptor through tunneling. In FRET, exciton transfer happens via electromagnetic dipole-dipole interaction, also called Coulombic coupling. It is a short-ranged, high efficient process. DET and FRET are NRET processes because no photons are emitted nor absorbed during energy transfer. Lastly, there is RET process, in which the donor emitter fluoresces and the emitted photon then excites the acceptor. The range of RET can be very long; however, its efficiency is typically low as it involves two different emission and absorption events. Table 2.1 lists the donor emission rate (k_D), lifetime (τ_D) and quantum yield (QY) with and without FRET.

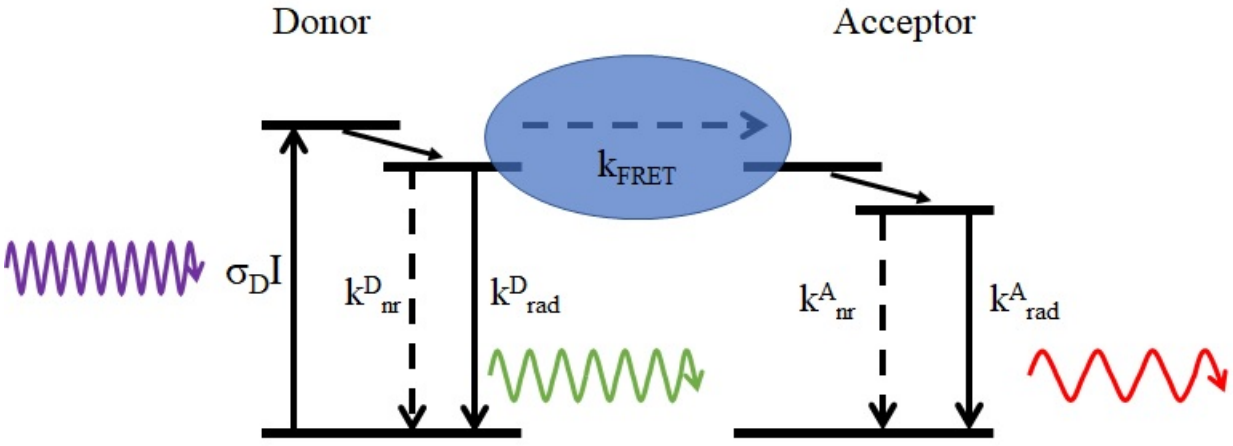

Figure 2.10: FRET: an additional pathway between a donor and an acceptor for energy transfer.

Table 2.1: Donor emission rate (k_D), lifetime (τ_D) and quantum yield (QY) with and without FRET.

$k_D = k_{rad} + k_{nr} + k_{FRET}$	$k_D = k_{rad} + k_{nr}$
$\tau_D = 1/k_D = \tau_{rad} + \tau_{nr} + \tau_{FRET}$	$\tau_D = 1/k_D = \tau_{rad} + \tau_{nr}$
$QY = \frac{k_{rad}}{k_{rad}+k_{nr}+k_{FRET}}$	$QY = \frac{k_{rad}}{k_{rad}+k_{nr}}$

2.3.1 Förster Resonance Energy Transfer(FRET)

Förster resonance energy transfer (FRET) governs energy transfer at a nano-scale range. One of the critical conditions is that the separation distance should be much shorter than the wavelength of light. The mathematical framework for FRET is developed by taking dipole approximation for the donor and the acceptor. Both the donor and the acceptor are assumed to be point dipoles (Figure 2.11). In doing so, it is assumed that their separation distance R is much larger than the physical dipole length.

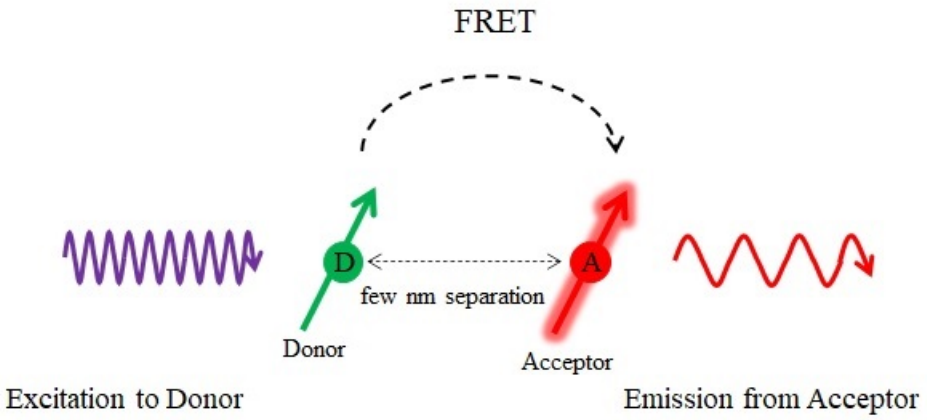

Figure 2.11: Transfer of donor excitation energy to an acceptor through distance-dependent FRET.

The electric potential of discrete electric charges interacting with the incident

electromagnetic field $\boldsymbol{E}_{inc}$ is given as follows [48]:

$$V_E = -\sum_n q_n \boldsymbol{r}_n.\boldsymbol{E}_{inc}(0) - \sum_n \frac{q_n}{2!}\boldsymbol{r}_n.(\boldsymbol{r}_n.\nabla)\boldsymbol{E}_{inc}(0) - \sum_n \frac{q_n}{3!}\boldsymbol{r}_n.(\boldsymbol{r}_n.\nabla)^2\boldsymbol{E}_{inc}(0) - ... \tag{2.6}$$

where $\boldsymbol{r}_n$ is the position vector of the n^{th} charge q_n and the origin is taken at $\mathbf{r} = 0$. The first term in Equation 2.6 is the the electric dipole interaction term. The second term is the electric quadrupole expansion. We neglect the discussion on the next higher-order terms for simplification. The pertinent conclusion drawn from the Equation 2.6 is the underlying physics represented by the first two terms. The first term is the outcome of the absolute value of the electric field at the center of the charge distribution. In contrast, the second term is the effect of the gradient of the electric field at the center of the charge distribution. Therefore, if the particle size is tiny, the electric field is approximated to be homogeneous over the particle volume, neglecting higher-order terms. This is the fundamental reasoning for the dipole approximation of small systems of charge such as nanoparticles.

Due to the proximity, FRET is governed by the near-field coupling between evanescent waves. The reactive electromagnetic field of an oscillating transition dipole in a donor induces transition dipole in an acceptor. The power transferred from a donor to an acceptor can be defined as [48]:

$$P_{D\to A} = \frac{\omega_0}{2} Im\{\boldsymbol{\mu}_A^*.\boldsymbol{E}_D(\boldsymbol{r}_A)\} \tag{2.7}$$

where $\boldsymbol{\mu}_A^*$ is the induced transition dipole moment in the acceptor, $\boldsymbol{E}_D(\boldsymbol{r}_A)$ is the local electric field generated by the donor at the location of the acceptor (Figure 2.12). Equation 2.7 accounts for both radiative as well as nonradiative component. When the separation distance is very small, the nonradiative component dominates.

The energy transfer rate is related to the power transferred as follows:

$$\frac{k_{D\to A}}{k_0} = \frac{P_{D\to A}}{P_0} \tag{2.8}$$

where k_0 is the decay rate of the donor in the absence of acceptor, and P_0 is the power dissipation in the absence of the acceptor and is defined as:

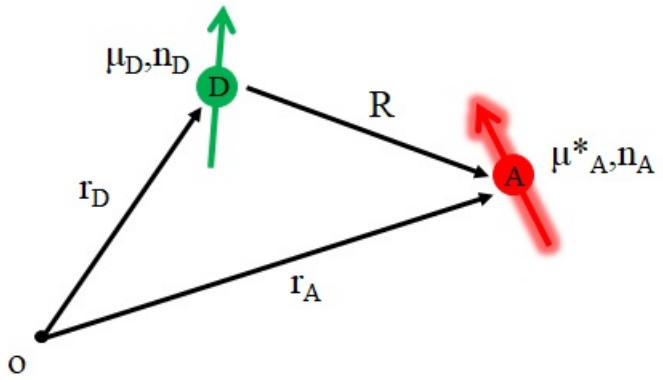

Figure 2.12: Energy transfer between a donor (D) and an acceptor (A) via dipole-dipole coupling.

$$P_0 = \frac{|\boldsymbol{\mu}_D|^2 n(w_0)}{12\varepsilon_0 c^3} w_0^4 \tag{2.9}$$

where $\boldsymbol{\mu}_D$ is the transition dipole moment of the donor, w_0 is the radiating frequency of the donor dipole, c is the speed of light in vacuum, ε_0 is the permittivity of free space, and $n(w_0)$ is the refractive index of the medium where the donor and the acceptor are located. In the linear regime, the induced dipole moment can be written as:

$$\boldsymbol{\mu}_A = \overleftrightarrow{\alpha}_A \, \boldsymbol{E}_D(\boldsymbol{r}_A) \tag{2.10}$$

where $\overleftrightarrow{\alpha}_A$ is the acceptor polarizability tensor. After expressing polarizability in terms of the absorption cross-section, expanding the donor's field, $\boldsymbol{E}_D$, in terms of the free space Green's function, we can eventually express Equation 2.8 as what is known as Förster resonance energy transfer [49]:

$$\frac{k_{D\to A}}{k_0} = \left[\frac{R_0}{R}\right]^6, R_0^6 = \frac{9c^4\kappa^2}{8\pi} \int_0^\infty \frac{f_D(w)\sigma_A(w)}{n^4(w)w^4} dw \tag{2.11}$$

where $n(w)$ is the refractive index of the environment, R is the distance between the donor and the acceptor, and R_0 is the Förster radius, R_0 is the distance at which FRET efficiency falls to 50 %, κ^2 is the relative orientation between the donor and the acceptor and lies in the range of $\kappa^2 = [0...4]$. The random orientation is represented by its average value of $\frac{2}{3}$. The integrand terms in Equation 2.11 suggest that energy transfer rate depends on the overlap of the donor's emission spectrum, $f_D(w)$, and the acceptor's cross-section, $\sigma_A(w)$.

FRET efficiency represents the modification in the fluorescence emission of the donor and is expressed as:

$$\eta_{FRET} = \frac{P_0}{P_0 + P_{D\to A}} = \frac{1}{1 + (R/R_0)^6} \tag{2.12}$$

If there are more acceptors per donor then the equation becomes:

$$\eta_{FRET} = \frac{nR_0^6}{nR_0^6 + R^6} \tag{2.13}$$

where n is the number of acceptors per donor. FRET transfer efficiency can also be defined as:

$$\eta_{FRET} = \frac{k_{FRET}}{k_{FRET} + k_{rad}} \tag{2.14}$$

Combining Equation 2.12 and Equation 2.14, we obtain:

$$k_{FRET} = \frac{1}{\tau_{rad}} \left(\frac{R_0}{R}\right)^6 \tag{2.15}$$

where τ_{rad} is the radiative decay lifetime of the donor. This is also the donor's lifetime in the absence of the acceptor and taken equal to τ_D while ignoring other nonradiative processes. From Equation 2.15, it is apparent that FRET is a distance-sensitive mechanism. One key distinction between FRET rate and FRET efficiency is that while the former tends to be directly related to the donor's decay rate, FRET efficiency does not. FRET efficiency is primarily affected by the donor-acceptor separation and the oscillator strength of the absorbing system. The energy transfer efficiency can also be defined in terms of the donor lifetime or emission intensity [49]:

$$\eta_{FRET} = 1 - \frac{\tau_{DA}}{\tau_D} = 1 - \frac{F_{DA}}{F_D} \tag{2.16}$$

where τ_{DA} is the donor lifetime in the presence of an acceptor and τ_D is the lifetime in the absence of the acceptor. F_{DA} is the emission intensity in the presence of the acceptor, and F_D is the intensity in the absence of the acceptor. From Equation 2.15, it can be seen that FRET rate scales with R^{-6}. This distance dependency holds when both the donor and the acceptor are point dipoles, i.e., zero-dimensional (OD). FRET rate's distance scaling is dependent on the acceptor geometry [85–88]. Table 2.2 summarizes the distance scaling of the FRET rate for the different acceptor dimensionalities.

Table 2.2: Effect of the dimensionality of acceptor on the distance dependency of FRET.

Distance dependency	acceptor geometry
R^{-6}	point-like dipoles
R^{-5}	1D acceptor, e.g., nanowire
R^{-4}	2D acceptor, e.g., quantum well
R^{-3}	3D acceptor, e.g., bulk

2.3.2 Plasmonics

Plasmons are coherent oscillations of free electrons in metals. They are called surface plasmons (SPs) when excited at the surface of the metal. SPs are quasi-particles. They exist at the metal-dielectric interface. These quantized oscillations of electrons are generated due to the interaction with the electromagnetic (EM) waves. Figure 2.13 provides the summary of how the light-metal interaction is affected by the increasing confinement in the metal. The coupling between plasmons and photons results in the generation of another quasiparticle called a polariton. In 2D and 1D systems, these polaritons have the freedom to propagate along the surface and are called surface plasmon polaritons (SPPs) [89]. When the metal particle has dimensions smaller than the surface plasmon polariton (SPP) propagation length, the surface plasmons are localized around the metal particle and produce localized surface plasmon resonance (LSPR) [90].

Metal nanoparticles (MNPs), with a much smaller size than the wavelength of the light, can enhance the light-matter interaction. When illuminated, plasmons are excited in the MNPs. These plasmons boost the strength of the local EM field in the close vicinity of the MNP. MNPs are called optical nano-antenna because of this amplification effect. This amplified EM field leads to EM enhancement. The region with enhanced EM field define the hot spots of the EM field as shown in Figure 2.14. These SPs have a resonance response at a specific wavelength known as the plasmon resonance. Since the resonance is localized around the particle, these resonances are also called localized surface plasmon resonance (LSPR). The metal NPs could be suspended in a liquid, can be a rough edge on the surface,

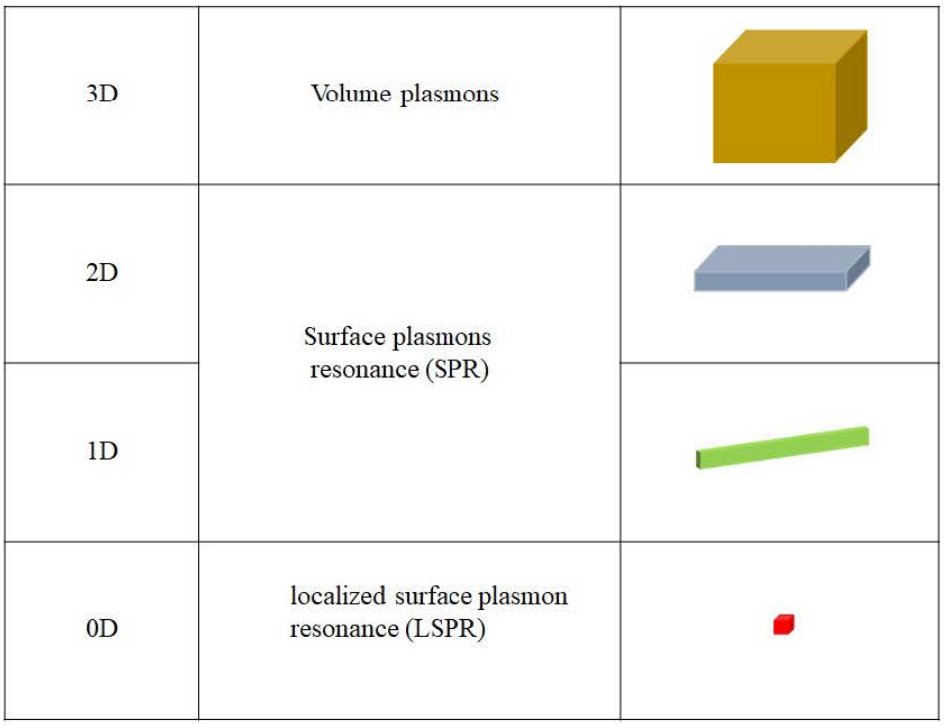

Figure 2.13: Effect of dimensionality of the metal structure on the light-metal interaction.

or maybe placed periodically on a surface. This resonance wavelength depends on the material property, shape and size of the metal (Figure 2.15), and the local dielectric environment around the MNP [91, 92]. Spectral shifts related to the LSPR are influenced more strongly by the deviation from spherical geometry than by increased dimensions.The morphology of the MNP determines how the EM field is distributed around the nanostructure. The electric field is tightly confined at the corners and sharp edges of the NP. The effect is easily seen in Figure 2.14b where a plane wave illuminated the nano-triangular plate and the enhanced field can be seen to be concentrated on its vertices. An increase in edges or sharpness of an MNP also shifts its extinction spectra to the red because of the increased charge separation.

The question arises why these MNPs behave in this resonant manner. Metal has a sea of free mobile electrons, i.e., they are released from their atoms. These electrons are free to move around. Overall, metal is neutrally charged; so, it has an equal number of positively charged atomic nuclei. The word plasmonic

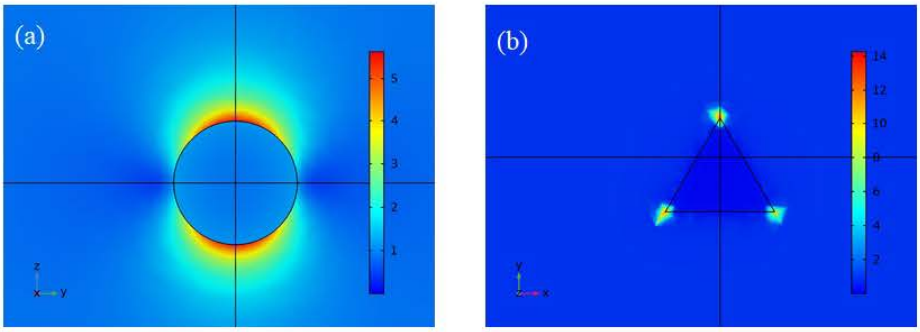

Figure 2.14: Plasmonic hotspots around the MNPs of different shapes (a) Spherical NP and (b) Metal nanoprism.

is derived from the plasma, which means a system where many positively and negatively charged particles are present and are free to move independently of each other. When an electric field is applied, negative and positive charges are pulled apart as shown in Figure 2.16 [93]. This electric field creates a force causing separation. However, this electric field also exposes charges at the surface of the metal. These exposed charges are of the opposite type and produce a restoring force opposite in direction to the original driving field because of attraction. The strength of this restoring electric field depends on the material property, such as the density of the roaming charges. This field can be stronger than the initial field creating it.

This resonant field inside the MNP creates a dipole field outside the NP. The strength of this dipole field diminishes much quickly with the distance, hence making extreme light confinement in the sub-wavelength region surrounding the MNP. This dipole field results in the increased absorption and scattering cross-sections and EM enhancement surrounding the MNP. Since the electric field is oscillating in the EM wave, the MNP acts like a driven harmonic oscillator with a natural frequency, the resonant frequency. When the frequency of the incident light matches the natural frequency of the MNP resonator, we observe the LSPR. The effectiveness of how strongly surface charges are exposed and exert the restoring force on the opposite charge is affected by the dielectric property of surrounding material filling the space, increasingly with the increased dielectric constant of the surrounding environment. The LSPR redshifts with increasing

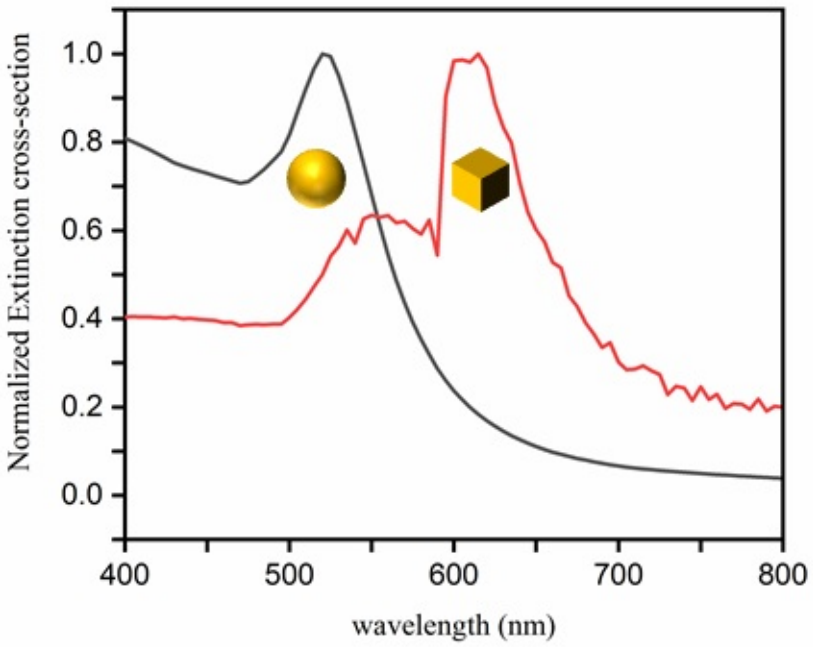

Figure 2.15: Influence of the morphology on the LSPR wavelength.

dielectric constant of the surrounding medium. This is due to the buildup of polarization charges on the dielectric that reduces the restoring force inside MNP. Nano-sized metal particles experience the LSPR because the entire metal volume should experience a uniform electric field. If the particle were to be larger than the wavelength of the EM wave, there would not be the same average electric field over the whole material. In a nutshell, the oscillation frequency of these NPs is influenced by the electron density, the effective electron mass, and the size and shape of the charge distribution.

The discussion presented in the previous section on spherical particles is valid for metal particles as well. The extinction spectrum of a metal sphere is given as [94]:

$$E(\lambda) = \frac{24\pi^2 N a^3 \varepsilon_m^{3/2}}{\lambda ln(10)} \left[\frac{\varepsilon_i(\lambda)}{(\varepsilon_r(\lambda) + \chi\varepsilon_m)^2 + \varepsilon_i(\lambda)^2} \right] \tag{2.17}$$

where $\varepsilon_r(\lambda)$ and $\varepsilon_i(\lambda)$ are real and imaginary parts of the complex dielectric constant $\varepsilon(\omega)$ of the metal, and the dielectric constant of the environment, ε_m is real, and χ is a constant determined by the shape of the particle. $\chi = 2$ for

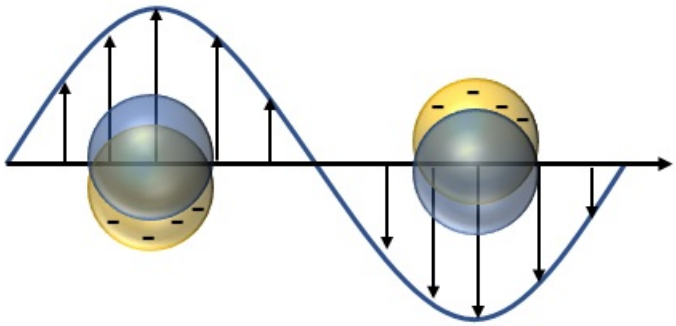

Figure 2.16: Dipole creation in MNP due to the impinging light.

spherical particle [95]. When the real part of the dielectric function of metal equals $-2\varepsilon_m$, the EM field surrounding the metal NP is enhanced.

For metals, the contribution of free electrons has to be incorporated in Equation 2.41. The Drude model essentially states that the optical properties of the metals are described by the response of the conduction electrons. The model is based on the behavior of the quasi-free electrons. The resulting model is expressed as:

$$\varepsilon(\omega) = 1 - \frac{\omega_p^2}{\omega^2 + i\gamma\omega} \tag{2.18}$$

$$\omega_p^2 = \frac{Ne^2}{\varepsilon_0 m_e} \tag{2.19}$$

where ω_p is the bulk plasma frequency, γ is the damping constant of the bulk plasma originating from the lossy behavior of the metal, N is the electrons per unit volume, e is the charge of the electron, ε_0 is the vacuum permittivity, and m_e is the mass of the electron. We need to include the interband transitions of bound electrons as well to accurately account for all the contributions. The resultant Drude-Lorentz model is expressed as [96]:

$$\varepsilon(\omega) = 1 - \frac{\omega_p^2}{\omega^2 + i\gamma_d\omega} + \sum_{n=1}^{k} \frac{f_n\omega_n^2}{\omega_n^2 - \omega^2 + i\gamma_n\omega} \tag{2.20}$$

where k is the total number of oscillators with resonant frequency ω_n, f_n is the weighting coefficient, $1/\gamma_n$ is the lifetime, ω_p is the plasma frequency of intraband transition with the damping constant γ_d.

The position of the plasmonic resonance depends on the electron density. The more electrons per unit volume a material has, the more plasmonic resonance shifts to the blue. LSPR for gold and silver is in the visible range of the spectrum. ω_p is the maximum frequency of the light reflected into the atmosphere by the metal. ω_p is responsible for the metallic sheen. Beyond ω_p, the real part of the metal's dielectric function becomes positive, and metal behaves as a transparent material. Broadly speaking, a material having a negative real and positive imaginary (small in magnitude) dielectric constant can support SPR [94]. The size of the MNP affects the overall extinction cross-sectional spectrum of the MNP. The absorption cross-section is the dominant electromagnetic cross-section for a small MNP ($<$ 30 nm), whereas the scattering cross-section dominates for the large-sized MNPs.

To summarize, LSPR is a nanoscale process that occurs when light interacts with the metal nanoparticles. Due to the coupling between the incident EM field and metal surface, there is a local EM field enhancement in the near-field of the nanoparticle. The resonance produces strong spectral absorption and scattering peaks.

2.3.2.1 Metal-Modified Fluorescence

Fluorescence is the emission of light by a particle after absorbing EM radiation. One difference between scattering and fluorescence is the time scale of each process. Scattering is an instantaneous process, whereas fluorescence is a nanosecond scale process involving absorption and spontaneous emission. Modification of the fluorescence intensity is regulated by relative enhancements of radiative and nonradiative decay rates.

Metal surfaces can affect both the radiative and the nonradiative rates of the fluorophores. The increased local field intensities in the vicinity of metal causes a change in Photon Mode Density (PMD) which boosts the spontaneous emission rate of the emitter. PMD gives the number of EM states per unit volume per unit frequency accessible to the emitter to exchange energy. Also, MNPs create an

additional nonradiative channel through which energy is transferred between the emitter and the metal nanostructure (Figure 2.17). Thus, the relative magnitude of increase in the decay rates determines whether the fluorescence intensity is quenched or enhanced. When fluorophores and MNPs are closely spaced, nonradiative decay dominates. In this separation regime, energy is transferred from excited fluorophores to the metal via FRET. As a result, there is a reduction in the radiative lifetime and quenching of the fluorescence intensity. The excitation energy is dissipated as heat in the metal but as the separation increases, radiative decay starts dominating and enhances the fluorescence intensity [51]. As the fluorophore is moved further away, coupling of excited fluorophores with the plasmonic mode takes place. With optimized distance, resonant energy transfer can enhance the fluorescence [97, 98]. However, if the separation is too large, fluorescent molecules will not experience the plasmonic field and hence not couple to it.

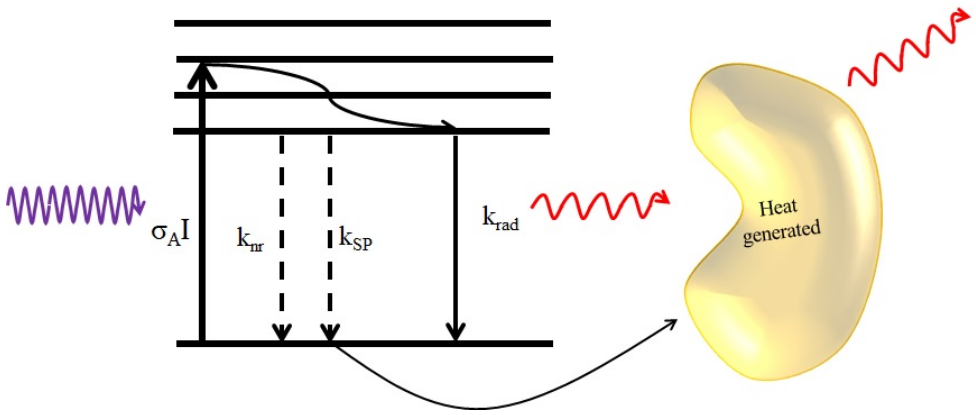

Figure 2.17: Additional decay channels in an emitter due to the nearby plasmonic nanostructure.

Let $k_{rad}^{0'}$ be the radiative decay rate of the emitter to the free space in the presence of MNP. This is the uncoupled component. Let k_{rad}^{MNP} and k_{nr}^{MNP} be the radiative and nonradiative decay rates of the MNP. The rate at which an emitter radiates into the far field in the presence of the MNP is given by:

$$k_{far} = k_{rad}^{0'} + k_g \frac{k_{rad}^{MNP}}{k_{rad}^{MNP} + k_{nr}^{MNP}} \tag{2.21}$$

where k_g represents the decay of the emitter by the MNP. The radiative enhancement factor, F_{rad}, is defined as:

$$F_{rad} = \frac{k_{far}}{k^0_{rad}} \tag{2.22}$$

The Purcell factor is defined as:

$$F_P = \frac{k^{0'}_{rad} + k_g}{k^0_{rad}} \tag{2.23}$$

The total decay rate of the emitter is defined as:

$$k_{tot} = k^{0'}_{rad} + k_g + k^0_{nr} + k^{e-m}_{nr} \tag{2.24}$$

where k^0_{nr} is the nonradiative decay in the emitter in the absence of the MNP and k^{e-m}_{nr} is the quenching due to charge transfer from the emitter to the metal. The total lifetime reduction is given as:

$$F_{tot} = \frac{k_{tot}}{k^0_{rad} + k^0_{nr}} \tag{2.25}$$

The quantum yield in the absence of metal NP is given by:

$$QY_0 = \frac{k^0_{rad}}{k^0_{rad} + k^0_{nr}} \tag{2.26}$$

The quantum yield in the presence of metal nanostructure is therefore:

$$QY = F_{rad}/F_{tot} = k_{far}/k_{tot} = \frac{k^{0'}_{rad}}{k_{tot}} + \frac{k_g}{k_{tot}} \frac{k^{MNP}_{rad}}{k^{MNP}_{rad} + k^{MNP}_{nr}} \tag{2.27}$$

Fluorescence enhancement can thus be produced through: (i) increasing absorption and (ii) increasing PMD. If plasmonic resonance overlaps with the absorption of the molecule, then the absorption rate is enhanced. If the plasmonic mode spectrally coincides with the molecule's emission, then additional decay channels may be created for the molecule. In this case, besides the molecule spontaneously emitting, the excited molecule can excite surface plasmon, scattering light into free space. This will shorten the lifetime of the fluorescent molecule and increase efficiency.

Research has shown that fluorophore's emission maximum should be marginally redshifted with reference to the LSPR peak for maximum fluorescence enhancements. Both the radiative and nonradiative decay rates are increased on the resonance condition. When the fluorophore's emission peak is slightly redshifted, the nonradiative decay rate is suppressed more, leading to overall fluorescence enhancement.

To summarize, the key variables which can be controlled to manipulate fluorescence intensity are:

- Spectral overlap of MNP resonance with excitation or emission spectra of the fluorophore.
- MNP–fluorophore separation distance.
- Use of larger MNPs (60-80 nm).
- Anisotropic MNPs, which are more effective in comparison to spherical MNPs.
- Choice of metal.

2.4 Role of the Environment on the Emission of an Emitter

The surrounding environment can strongly modify the radiation properties of an emitter [99]. E.M. Purcell was the first scientist who established that the surrounding environment impacts the spontaneous emission of emitters [100]. The ratio of the modified spontaneous emission rate to that of the free space emission rate is known as the Purcell factor. Subsequently, Chance, Prock, and Silbey presented a model explaining the interaction between the emitting dipole and the nearby metallic surface [46]. D. L. Dexter extended the work and proposed the possibility of the energy transfer from an excited molecule to the nearby

semiconductor [45]. Fermi's golden rule describes the decay rate of the emitter quantum mechanically. The transition rates are given as follows [101]:

$$\gamma_{ij} = |\boldsymbol{M}_{ij}|^2 \rho(\nu_{ij}) \tag{2.28}$$

where γ_{ij} represents the transition rate from the i^{th} energy state to the j^{th} energy state, $\boldsymbol{M}_{ij}$ is the transition matrix element determined by the wavefunctions connecting the energy levels. The quantity $\rho(\nu_{ij})$ in Equation 2.28 represents the density of photon states at the transition frequency, which is the photon mode density (PMD). According to Equation 2.28, the decay rate is proportional to the PMD. Decay rates can also be manipulated through $\boldsymbol{M}_{ij}$ term in Equation 2.28; however, that requires the interface to be extremely close to the emitter. On the contrary, the separation distance over which PMD can affect the decay of the emitter is typically equal to emission wavelength. The preceding concepts use the quantum mechanical interpretation of the radiation properties of the emitter. However, subsequently, we will be restricting our explanation to a more semi-classical viewpoint that looks at the media's ability surrounding the emitter to support the electromagnetic modes.

When the emitter is brought closer to the planar interface, the reflection at the interface results in interference with the incident wave causing constructive or destructive interference depending on the phase of the reflected wave. If the interference is constructive, the PMD at the emitter location is increased, and the spontaneous emission is enhanced; otherwise, the emission is quenched. Another way to explain it is that the introduction of the interface provides additional paths to support the electromagnetic modes, resulting in the modification of the spontaneous emission of the emitter.

In the classical approach, the emitter is taken to be a forced damped electric dipole oscillator (Figure 2.18). The electric field at the dipole's position can be decomposed as:

$$\boldsymbol{E}(\boldsymbol{r}_0) = \boldsymbol{E}_d(\boldsymbol{r}_0) + \boldsymbol{E}_s(\boldsymbol{r}_0) \tag{2.29}$$

where $\boldsymbol{E}_d(\boldsymbol{r}_0)$ is the primary dipole field and $\boldsymbol{E}_s(\boldsymbol{r}_0)$ is the scattered field at the position of the dipole, $\boldsymbol{r}_0$, after it has been scattered from the surrounding.

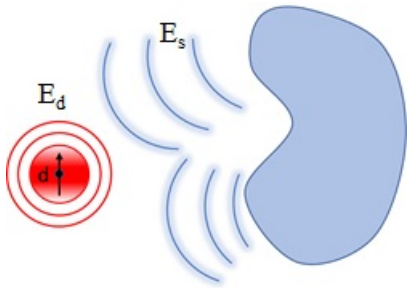

Figure 2.18: Interaction of the dipole with an inhomogeneous environment in its vicinity.

Purcell factor or Purcell enhancement, the ratio of the modified decay rate of the radiating dipole and the free space decay rate, is given by [48]:

$$\frac{\gamma}{\gamma_0} = 1 + \frac{6\pi\varepsilon_1}{|\boldsymbol{\mu}|^2 k_0^3} Im[\boldsymbol{\mu}^*.\boldsymbol{E}_s(r_0)] \tag{2.30}$$

$$= 1 + \frac{\mu_x^2 + \mu_y^2}{\mu^2} \int_0^\infty Re\left(\frac{s}{s_z}[r^s - s_z^2 r^p] e^{(2ik_1 z_0 s_z)}\right) ds \tag{2.31}$$

$$+ \frac{3\mu_z^2}{2\mu^2} \int_0^\infty Re\left(\frac{s^3}{s_z} r^p e^{(2ik_1 z_0 s_z)}\right) ds$$

where z_0 is the height of the dipole above the layered medium, the integration variable s represents the normalized in-plane wavenumber: $s = k_\rho/k_1$ in the medium 1, $s_z = \sqrt{(1-s^2)} = k_{z1}/k_1$ is the perpendicular component of wavenumber at the interface, r^s and r^p are the Fresnel reflection coefficient for s- and p- polarizations at the interface, and $\boldsymbol{\mu}_x, \boldsymbol{\mu}_y, \boldsymbol{\mu}_z$ are the cartesian components of the dipole moment $\boldsymbol{\mu}$. From Equation 2.30, it can be seen that Purcell enhancement is proportional to the imaginary part of the scalar product between the dipole moment and the scattered field. Purcell effect can be termed as the back action of the dipole on itself through the interaction with the medium. The dipole emits the wave, and this emitted wave polarizes the medium. The polarizability generated in the medium radiates the scattered fields which come back and interact with the dipole. Depending on the interaction, PMD can increase or decrease. The imaginary part of the product in Equation 2.30 describes that interaction.

Equation 2.31 represents the total decay rate. The contributions from all possible channels can be acquired by splitting the integration variable s into different

integration ranges. The integration range [0...1] corresponds to the electromagnetic modes associated with plane waves. These modes can propagate in the entire space. This contribution is radiative. The integration range $[1...\sqrt{\varepsilon'}]$ corresponds to the component which is evanescent in the upper half-space but propagates in the Si substrate (lower half). Here, ε' is the real component of silicon's dielectric function. This contribution is also radiative. The integration range $[\sqrt{\varepsilon'}...\infty]$ corresponds to the nonradiative component. The last contribution is what we are interested in as far as FRET analysis is concerned. This integration limit describes the creation of electron-hole pairs in the medium directly through near-field of emitter dipole without the participation of a photon [38].

2.4.1 Generalized Fresnel Reflection Coefficients (3 Layers)

Figure 2.19: Reflection from (a) a three-layer medium and (b) a four-layer medium.

For a three-layered structure (Figure 2.19a), the generalized reflection coefficient for s- and p- polarized waves are given by:

$$r^{(s,p)} = \frac{r_{1,2}^{(s,p)} + r_{2,3}^{(s,p)} e^{2ik_{2z}d}}{1 + r_{1,2}^{(s,p)} r_{2,3}^{(s,p)} e^{2ik_{2z}d}} \tag{2.32}$$

$$r_{i,j}^{s} = \frac{k_{zi} - k_{zj}}{k_{zi} + k_{zj}} \tag{2.33}$$

$$r_{i,j}^{p} = \frac{\varepsilon_j k_{zi} - \varepsilon_i k_{zj}}{\varepsilon_j k_{zi} + \varepsilon_i k_{zj}} \tag{2.34}$$

where $d = d_2 - d_1$ is the film thickness, $r_{(i,j)}^{(s,p)}$ is the reflection coefficient at the

single planar interface (i, j) as defined in Equations 2.33 and Equation 2.34 and k_{2z} is the longitudinal wavenumber in the thin film. The longitudinal wavenumber in each medium can be defined as:

$$k_{zi} = \sqrt{k_i^2 - (k_x^2 + k_y^2)} = \sqrt{(k_i^2 - s^2 k_1^2)} \tag{2.35}$$

where (k_x, k_y) are conserved across each region and can be defined in terms of the wave-vector in the 1^{st} medium as:

$$k_{\parallel} = k_{\rho} = \sqrt{(k_x^2 + k_y^2)} = k_1 sin\theta_1 = sk_1 \tag{2.36}$$

2.4.2 Generalized Fresnel Reflection Coefficients (4 Layers)

For a geometry in Figure 2.19b, with two thin layers, the generalized reflection coefficient for s- and p- polarized waves are given by:

$$\bar{r}^{(s,p)} = \frac{r_{1,2}^{(s,p)} + \bar{r}_{2,3}^{(s,p)} e^{2ik_{2z}(d_2 - d_1)}}{1 + r_{1,2}^{(s,p)} r_{2,3}^{(s,p)} e^{2ik_2 z(d_2 - d_1)}} \tag{2.37}$$

$$\bar{r_{2,3}}^{(s,p)} = \frac{r_{2,3}^{(s,p)} + r_{3,4}^{(s,p)} e^{2ik_{3z}(d_3 - d_2)}}{1 + r_{2,3}^{(s,p)} r_{3,4}^{(s,p)} e^{2ik_{3z}(d_3 - d_2)}} \tag{2.38}$$

where $r_{i,j}^{(s,p)}$ is the reflection coefficient for the single interface (i, j) as defined in Equation 2.33 and Equation 2.34. Equation 2.37 and Equation 2.38 form recursive relationships between $\bar{r}_{i,i+1}$ and $\bar{r}_{i+1,i+2}$. These models can be used to calculate FRET efficiency [102].

2.5 Photosensitization of Silicon

One crucial utilization of the FRET process is in light-harvesting applications. Crystalline silicon is the typically used semiconductor in photovoltaic and photodetector devices. However, silicon cannot efficiently utilize sunlight due to

its low absorption coefficient. The main reason for poor performance in photogenerated charge carriers is that silicon has an indirect bandgap. Photosensitization of the semiconductor can help in the enhancement of electron-hole pair generation [103,104]. The increase in carrier generation in silicon can be achieved by placing a strongly absorbing scintillator close to the surface of silicon [105, 106]. The essential criterion for choosing the external light sensitizers is that they should possess a large absorption cross-section. In a FRET-based hybrid system, once exposed to light, the excitons are generated. Then, the energy transfer to the proximal semiconductor layer through near-field dipole-dipole coupling occurs. The essential advantage of using FRET as an energy transfer mechanism is that excitation energy is directly coupled to silicon, bypassing the exciton recombination step in the donor [39]. In this process, there are three steps: (1) absorption of incident light, (2) transfer of the excitation energy, and (3) charge generation in the silicon layer. Despite being a poor absorber, silicon is the vital material platform not only because it offers a mature fabrication technology platform but also because it possesses high carrier mobility and good charge separation and transport [38]. Such novel hybrid systems are interesting as they enable us to combine the strengths of two material systems.

2.6 Absorption and Scattering

When the incident electromagnetic field interacts with particles, electrons inside them oscillate in response to the impinging light. The oscillation induces polarization (induced dipole) in the particles followed by re-radiation of the field, which combines with the incident field and produces the scattered field (Figure 2.20). Some of the incident energy is absorbed by the particle as well and turned into heat.

These processes are represented in terms of cross-sections as follows:

$$\sigma_{sca} = \frac{P_{sca}}{I_{inc}}, \sigma_{abs} = \frac{P_{abs}}{I_{inc}} \tag{2.39}$$

$$\sigma_{ext} = \sigma_{sca} + \sigma_{abs} \tag{2.40}$$

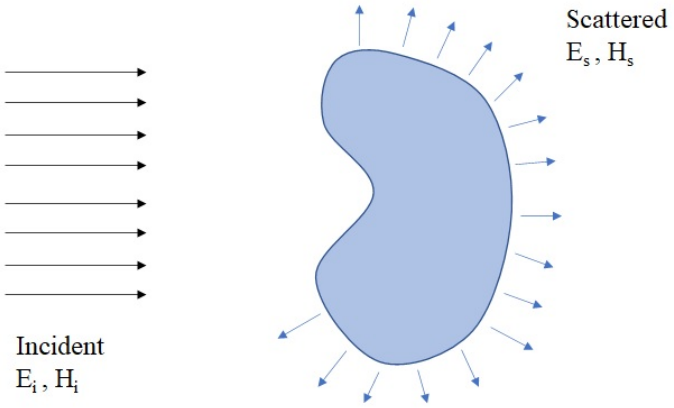

Figure 2.20: Scattering of EM field by an obstacle in response to the incident EM wave.

where σ_{sca} is the scattering cross-section, σ_{abs} is the absorption cross-section and σ_{ext} is the extinction cross-section.

The dielectric function of the material determines its polarization induced by the incident electromagnetic field, and the dielectric function hinges on the material's electronic structure [107]. However, the optical properties of solids can be accurately approximated using classical harmonic oscillator modeling that Lorentz introduced. Using the Lorentz mode, the dielectric function for non-conducting materials is given by [108]:

$$\varepsilon = 1 + \frac{f}{\omega_0^2 - \omega^2 + i\gamma\omega} \tag{2.41}$$

where f is the oscillator strength, ω_0 is the resonant frequency of the bound electrons, and γ is the damping constant.

Similar to any other linear optical phenomenon, Maxwell's equations need to be solved to obtain the solution of this interaction. In general, the solution is very complex for an arbitrarily shaped particle. The simplest case with an analytic solution available is light scattering by sphere embedded in a homogeneous medium developed by Mie in 1908 [109]. For the small particles, the electric field is taken to be the same over the entire volume of the particle. The laws of electrostatics are adequate to describe this interaction. Light scattering by spherical particles is described by solving the Laplace equation with continuous boundary conditions

using the quasi-static approximation. When illuminated by an electromagnetic wave with an electric field denoted by the vector $\mathbf{E_0}$, the dipole moment can be expressed as:

$$P = 4\pi\varepsilon_m a^3 \left(\frac{\varepsilon_p - \varepsilon_m}{\varepsilon_p + 2\varepsilon_m}\right) E_0 \tag{2.42}$$

where a is the particle's radius, ε_p is the permittivity of the particle, and ε_m is the permittivity of the surrounding medium. The resulting expressions for scattering (C_{sc}) and absorption (C_{abs}) cross-sections are:

$$C_{sc} = \frac{8}{3}\pi k^4 a^6 \left|\frac{\varepsilon_p - \varepsilon_m}{\varepsilon_p + 2\varepsilon_m}\right|^2 \tag{2.43}$$

$$C_{abs} = 4\pi k a^3 Im\left(\frac{\varepsilon_p - \varepsilon_m}{\varepsilon_p + 2\varepsilon_m}\right) \tag{2.44}$$

Chapter 3

Fabrication and Characterization Techniques

In this Chapter, we will give an overview of the fabrication tools used in this thesis work. The essential requirement of nanofabrication is an extremely clean environment. Therefore, most of the fabrication in this thesis work was performed in the cleanroom.

There are many ways to deposit thin films onto the substrates, including physical vapor deposition (PVD), electrochemical deposition, and chemical vapor deposition (CVD). We used PVD and CVD techniques in this thesis; therefore, they will be the subject of our discussion in this chapter.

Another key process in nanofabrication is patterning, which is typically used along with thin film deposition. The standard patterning techniques are photolithography, electron-beam lithography (EBL), and nano-imprint lithography. We made use of EBL, of which operating principles we will briefly explain.

Another critical aspect is to characterize the fabricated structures precisely. Therefore, we will also introduce imaging and optical spectroscopy techniques.

3.1 Deposition Techniques

This thesis work involved thin film deposition (metal and dielectrics) and patterning. In nanofabrication, ambient environment itself could result in defects that could affect the purity of our deposited films. Therefore, primary requirement for depositing thin-film layers of high purity materials is to use vacuum systems. For this purpose, specialized equipment is needed.

3.1.1 Thermal Deposition

There are different techniques available for depositing films on a wafer. One such method is physical vapor deposition (PVD). There are two types of PVD: (1) sputtering and (2) evaporation. We will restrict our discussion to evaporation, which we used in this thesis. In this technique, the source (the material we want to deposit) is put in a thermal boat and melted through resistive heating. When in vacuum, it will start evaporating in all directions after melting (Figure 3.1). When the vapor hits the cold substrate, it condenses and forms a thin film on the substrate. This technique is primarily used for metal and dielectric deposition. This study used thermal evaporation for gold and silver deposition since these metals melt at low temperatures and produce steady deposition rates.

The boat is made of highly resistive material, typically tungsten. The boat heats up when current flows through it and melts the material placed on it in the process. Deposition control is key to depositing a film of uniform thicknesses. The deposition rate depends on the melt temperature, which is difficult to control. In the thermal deposition, we measure the deposited thickness in real time. The quartz crystal monitor sensor is used to measure the deposition thickness. The quartz crystal oscillates at a particular frequency. The oscillation of quartz crystal dampens as a result of the mass increase with material deposition. We close the shutter when the target thickness is reached. It is a line-of-sight deposition technique.

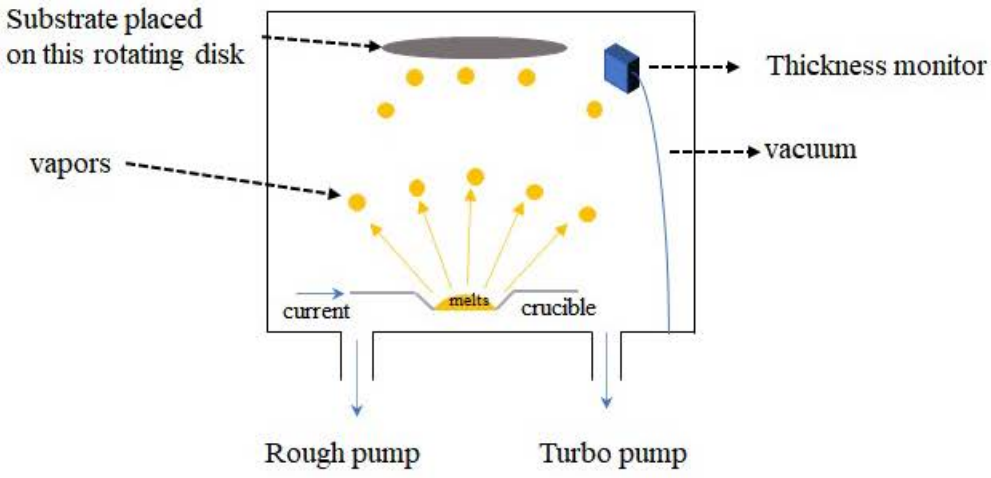

Figure 3.1: General illustration of the thermal deposition technique.

Low chamber pressure ($\approx 10^{-6}$ torr) is used to reduce the contamination because air molecules present during the deposition will become impurities in our deposited films. Roughing pump brings the pressure down to $\approx 10^{-3}$ torr. Then, the turbopump reduces it further down to the desired level. These turbopumps cannot operate at atmospheric pressures, thus we need to use a roughing pump initially.

3.1.2 Atomic Layer Deposition (ALD)

ALD is a thin film deposition technique from the vapor phase. The goal of this technique is to deposit multiple layers with atomic precision on the substrate. In the thesis, we needed to deposit dielectric spacer layers. Hence, we required a method to deposit thin uniform films with complete control. ALD is a conformal coating technique (Figure 3.2). With this technique, we can fully cover a complex 3D surfaces.

The ALD is a type of CVD method. It is a two-step cyclic process where layer-by-layer film is built. First, one gas phase precursor is introduced inside the vacuum chamber and adsorbed on the entire surface through chemisorption. Film growth is based on the saturated surface reactions of the gas and the surface

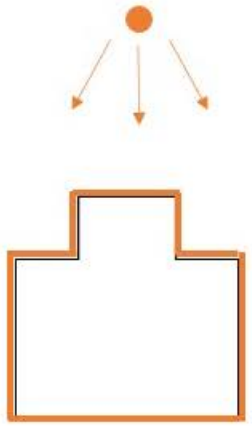

Figure 3.2: Illustration of the conformal coating.

species. Then another gaseous reactant is brought into the chamber, and a second layer is formed. Then the elements from the two layers react to develop the material of choice. With this technique, only a single molecular layer can be deposited in one cycle.

In a typical ALD deposition, first, the chamber is put under vacuum. Then we heat the chamber according to our recipe (80-250 ° C). Subsequently, the first gas comes in and reacts with the surface as long as it can find a free surface site. Eventually, all the surface sites will be occupied (the surface is then saturated). Next we purge the system and flush out the unreacted gas molecules. Afterwards we introduce the second gas reactant that will react with the surface until it saturates as well. Finally we purge the system again and repeat the ALD cycle until desired thickness is reached. ALD is a slow deposition method.

3.2 Rapid Thermal Annealing (RTA)

Thermal dewetting is a technique used to create metal nanoparticles. At first, a thin continuous metal film is deposited. Then thermal dewetting is applied to develop metal islands. The purpose of thermal annealing is to rupture the film, which then agglomerates at high temperatures.

To perform thermal dewetting, we used rapid thermal processing (RTP). In this process, a bank of very bright lamps rapidly heats a single wafer using optical energy. RTA uses radiative heating from the front side and/or backside. The sample to be exposed to annealing is placed on the wafer. The lamps are energized to ramp to the high temperatures very quickly (ramp rates of 200 °C/s or more are possible), unlike a furnace where the temperature ramp rate is slow. Interestingly in the RTA system, the chamber is enclosed in a cold wall. The purpose is only to heat the wafer and not the entire chamber. The RTA systems can ramp down temperature very quickly, too. Thus, compared to the regular furnace annealing, we can anneal at a very high temperature with different ramping-up and ramping-down rates very fast. Unlike furnace annealing, RTA can typically be applied for minutes only, depending on the target temperature. The higher the temperature, the shorter the annealing duration.

3.3 Electron Beam Lithography (EBL)

EBL is a lithography technique that uses exposure to the electron beam to form patterns. The advantage of using the EBL system is that we can pattern sub-wavelength features down to tens of nanometers without a mask, making it easier to change the design. Computer-aided design (CAD) tools are used to layout the patterns that we want to transfer to the substrate, and that pattern is directly loaded into the EBL machine. EBL systems use an electron beam to write each feature in the pattern sequentially. This is in contrast to the photolithography where all the pattern is illuminated at the same time.

The general procedure for metal array formation using EBL technique is shown in Figure 3.3. To begin with, we spin-coat the EBL resist on the substrate, which is sensitive to electrons. The quality of the resist material determines the minimum feature size. Then the substrate is loaded into the EBL machine. When the EBL resist is exposed to the electrons, the polymer undergoes a chemical change. An electromagnetic lens system is used to focus the electron beam. The advantage of using an electron beam is that it can be focused to a very narrow

spot size (< 5 nm in diameter). The beam deflectors can electronically deflect the focused beam at high speed based on the pattern fed to the machine, allowing the beam to be steered to different substrate regions. After electron exposure, the substrate is submerged in a chemical bath known as a developer. The developer will dissolve the EBL resist that was exposed and leave the unexposed regions as it is. After a couple of minutes, we remove the substrate from the developer solution, rinse with isopropanol alcohol, and dry with nitrogen gas. If we want to deposit a patterned metal, for instance, we can use any deposition process. Metal will stick to the substrate anywhere where the resist was removed during development. Finally, we carry out the liftoff process to remove the resist and have our patterned metal device.

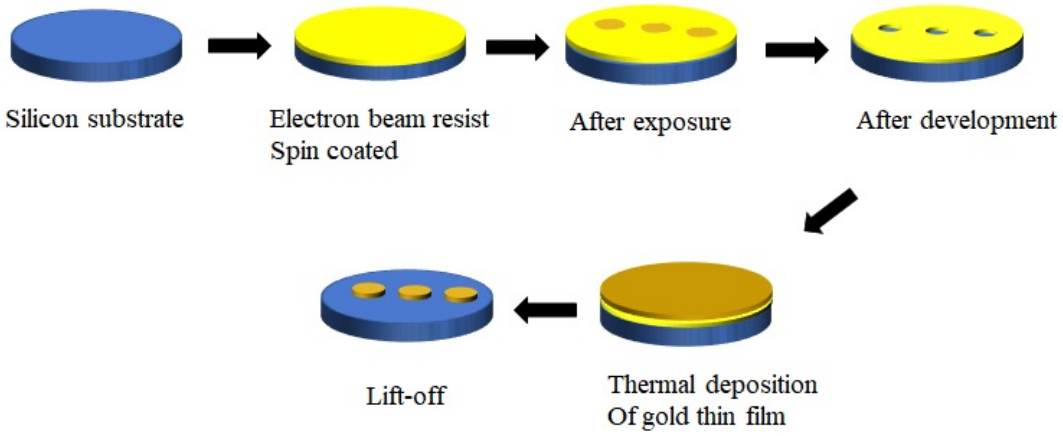

Figure 3.3: Illustration of the gold array fabrication on a substrate using the EBL technique.

3.4 Imaging Methods and Optical Spectroscopy

At present times, there is a wide variety of nanoscale imaging tools. The typical imaging techniques include electron microscopy, high-resolution optical microscopy, and scanning probe microscopy. As nanoscale research advances, these tools have become necessary to examine and manipulate nanoscale materials. Nanoscale imaging instruments are a crucial part of research in nanotechnology.

Optical microscopes are best suited to image structures that can be seen with the naked eye. Micron-sized objects can also be imaged; however, the diffraction limits its use for resolving nanostructures features that are typically less below 200 nm. To resolve such small elements, we need powerful microscopes such as scanning electron microscope (SEM), transmission electron microscope (TEM), and atomic force microscope (AFM).

3.4.1 Electron Microscopy

SEM is a microscope that produces images using electrons instead of visible light. The wavelength of light limits the resolution in an optical microscope. SEM can typically image a feature as small as a few nanometers. Electrons can interact with the sample in several different ways (Figure 3.4). In an electron microscope, we can detect backscattered and secondary electrons. When an electron beam strikes the sample, some of the electrons are absorbed. Some electrons are backscattered after elastic interaction with the sample, while some electrons are ejected from the atoms of the sample, which are called secondary electrons. These secondary electrons are a result of inelastic interaction between the incident electron beam and the sample. Secondary electrons have lower energies than the backscattered electrons.

Backscattered SEM images show fewer surface features than secondary electron SEM images. The contrast seen in the backscatter image is due to the differences in average atomic number. Regions with a higher atomic number will produce more backscattered electrons and will appear bright.

SEM operates in the vacuum; otherwise, the incident electrons will scatter the gas molecules and prevent us from focusing the beam on the sample. As a result, we can image only dry samples in a standard SEM. An environment SEM (ESEM) allows a controllable amount of water molecules inside the chamber at the expense of losing some of the beam focus. Therefore, the advantage of ESEM is that wet samples can be imaged as well.

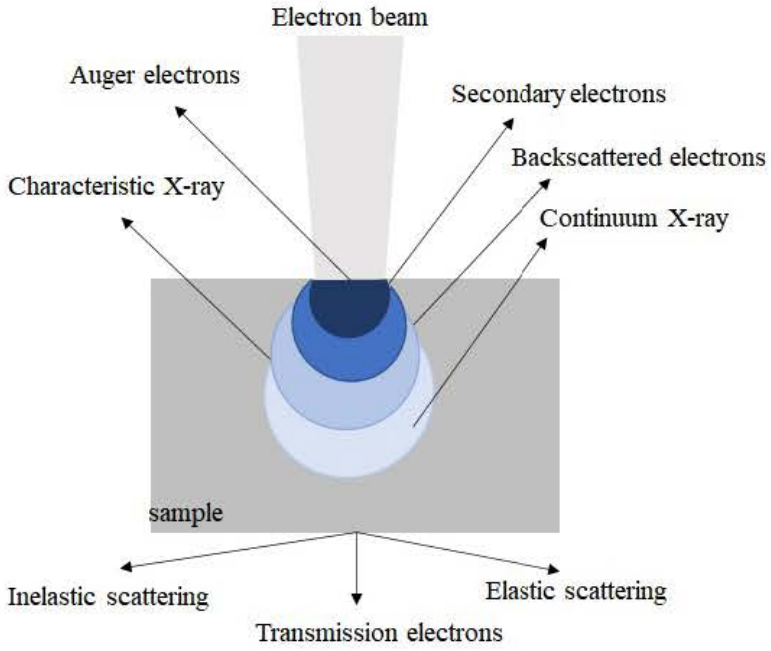

Figure 3.4: Occurrence of different phenomenon as a result of high energetic electron beam interacting with the sample material.

If the sample is absorbing incoming electrons, then it will build up a charge. Charging negatively impacts the quality of the image. One way to prevent charging is to coat a thin layer of metal on the SEM sample.

3.4.2 Confocal Microscopy

The drawback of a simple fluorescence microscope is that it excites all the fluorescence within the field of view in all dimensions with the same efficiency. However, the microscope objective has a small depth of focus. Thus there is fluorescence present outside the focused region of the sample. A microscope will collect all the signals, and out-of-focus fluorescence can cause blurriness in the images.

Confocal microscopy is a specialized fluorescence imaging technique designed to deal with the interference between the out-of-focus light and the in-focus light. Instead of using white light sources, confocal microscopes use laser sources for excitation. Lasers act as the point source of light, restricting the illumination

to a diffraction-limited spot within the field of view. In contrast, a fluorescence microscope illuminates everything unrestricted within the objective's field of view. Therefore, the illumination laser excites a tiny spot within the field of view (Figure 3.5). The confocal microscope also uses a pinhole to reject out-of-focus light.

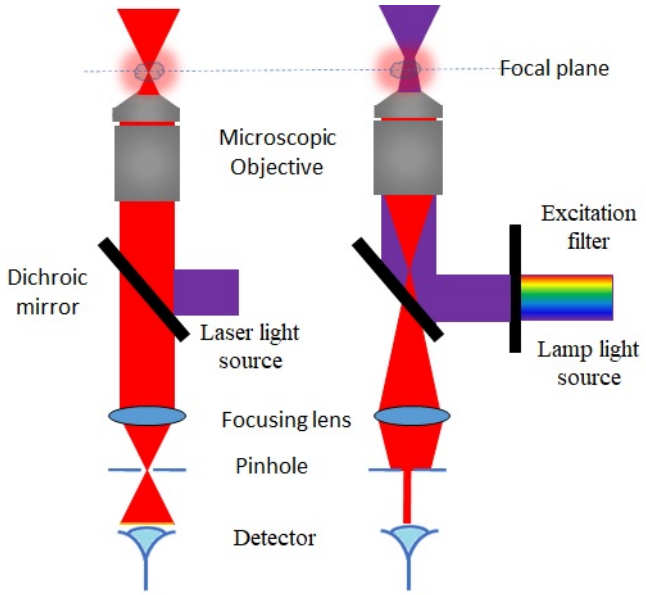

Figure 3.5: Illustration of spot size on the focal plane (a) conformal microscopy and (b) conventional microscopy.

3.4.3 Absorption and Photoluminescence Measurements

Steady-state optical characterization helps us to understand the optical properties of materials. Absorption and photoluminescence (PL) spectroscopies are crucial tools for investigating nanocrystals and plasmonic materials. The spectra of samples provide vital information about the electronic and chemical structure of materials. These absorption spectra can tell us a lot regarding the material under test, including the type of material, the nanoparticles' size, the sample's quality, and concentration quickly and easily.

UV-VIS is a technique that measures the absorption of the sample (solid or liquid) across the ultra-violet (UV) and visible regions of the electromagnetic spectrum. A broadband light source such as a Xe lamp is used together with

a monochromator to excite the sample, solid or in solution. A blank sample is used as a reference. The modification in the transmission in comparison to the reference sample gives the absorption spectrum of the sample. Absorbance is also known as optical density (OD). The instrument measures transmission (T). From the transmittance, we can calculate absorbance as $A = -log(T)$.

A hot body that emits emissions solely because of its temperature is said to be incandescent. All other forms of emissions are called luminescence. Excitation by absorbance of light leads to the emission of light, and this phenomenon is called photoluminescence (PL). PL has two types: (1) fluorescence and (2) phosphorescence. PL always involves Stoke's shift, which means that the emission wavelength is redshifted with respect to the excitation wavelength. In PL spectroscopy, the sample is excited by a predetermined wavelength of light, and the monochromator unit at the collection end spectrally scans the PL spectrum. PL spectroscopy provides information on the radiative characteristics of the sample.

3.4.4 Time-Resolved Fluorescence Measurements

In the previous section, we discussed steady-state measurements. Another powerful technique to study the excited-state decay kinetics is time-resolved fluorescence (TRF) spectroscopy. PL decay conveys the timescale of photoluminescence. For nanomaterials with PL decays, we can obtain much useful information including energy transfer, electron or hole transfer, quenching as well as insight about trap states. PL decay can give us the lifetime, τ, which is related to radiative (k_r) and nonradiative (k_{nr}) decay constants as follows:

$$\tau = \frac{1}{k_r + k_{nr}} \tag{3.1}$$

If we find out quantum yield, which is given by:

$$\Phi = \frac{number of photons emitted}{number of photons absorbed} = \frac{k_{nr}}{k_r + k_{nr}} \tag{3.2}$$

TRF spectroscopy gives us information regarding weighting and lifetime values

for individual components:

$$I(t) = \sum_i \alpha_i exp(-t/\tau_i) \tag{3.3}$$

The amplitude-averaged fluorescence lifetime τ_{avg} is given by:

$$\tau_{avg} = \frac{\sum_i \alpha_i \tau_i}{\sum_i \alpha_i} \tag{3.4}$$

Let $n(t)$ be the number of excited species and is expressed as:

$$n(t) = n_0 exp(-t/\tau) \tag{3.5}$$

comparing Equation 3.5 and Equation 3.3 suggests that number of excited species is proportional to the intensity seen by the detector.

In TRF spectroscopy, we count photons and place them in bins to build a histogram where each data point corresponds to a histogram bin. The TRF system performs time-correlated single-photon counting (TCSPC). We record when those photons arrive and putting them in time bins. We stop counting once the highest histogram point reaches the target count.

In a typical TSCPC system, a laser driver sends a signal to both the laser excitation source and timing electronics. The signal triggers the laser to generate a pulse. Light is going to hit the sample and then the sample will fluoresce. The emission will go to the monochromator and then to the detector. The electronics circuitry will time this event. A cutoff filter is placed before the monochromator to block any light from the laser source.

Laser pulse acts as a start signal. Later, the photon is detected, and the time difference from the start of the pulse is calculated (Figure 3.6) [110]. An excitation source is a pulse train at a constant repetition rate. And the system counts the photons in time bins. Photon count must be kept low to avoid double-counting, which is known as pulse pile-up. The detector and electronics have a deadtime (about 100 ns) after a photon is detected. In this dead time, they

do not respond. Any photon arriving during the dead time is missed, and the decay count is skewed. To avoid the situation count rate is kept low (2%) to keep photon yield low.

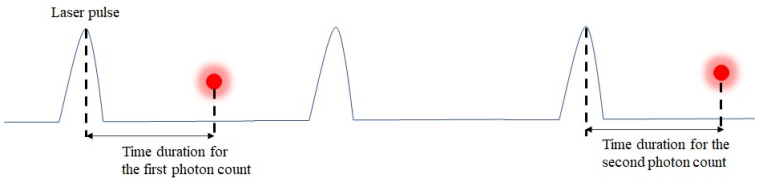

Figure 3.6: Schematic explaining the working principle of the time-correlated single-photon counting technique [110].

The instrument response function (IRF) sets the limit of resolution. Ideally, we would like to use a delta function as the excitation source. In reality, the excitation source has a finite pulse width. Thus the output is the convolution of excitation and the response. IRF sets the lower bound of the detection.

Chapter 4

Modified Emission Kinetics of Colloidal Quantum Wells via Energy Transfer to Bulk Silicon

This chapter is based on the journal publication "Near-Field Energy Transfer into Silicon Inversely Proportional to Distance using Quasi-2D Colloidal Quantum Well Donors," by M. H. Humayun, P. L. Hernandez-Martinez, N. Gheshlaghi, O. Erdem, Y. Altintas, F. Shabani, and H. V. Demir, which appeared in Small ([83]). (https://doi.org/10.1002/smll.202103524.)

As explained in Chapter 2 (see Section 2.3.1), the Förster resonance energy transfer (FRET) rate's distance scaling is dependent on the dimensions of the acceptor. However, recently, it has been reported by Taghipour *et al.* [61] that donor geometry also influences the FRET distance scaling. The distance scaling reported was d^{-2} for a 2D acceptor geometry against the expected one, d^{-4}. From a fundamental perspective, this poses questions regarding the role of donor geometry in affecting the FRET rate. Therefore, with this motivation, here we investigate the distance scaling of FRET in the case of colloidal quantum wells coupled to bulk silicon.

In addition to the dependence on the distance between the donor and acceptor, other parameters that affect the strength of the FRET are spectral overlap of the donor's emission spectrum and the acceptor's absorption spectrum, photoluminescence (PL) quantum yield of the donor, absorption cross-section of the acceptor, the relative orientation factor between donor and acceptor dipoles, and the refractive index of the surrounding medium [87,111,112]. The energy transfer rate (k_{ET}) from the donor to the acceptor follows the power relationship given as follows:

$$k_{ET} \propto d^{-n} \tag{4.1}$$

where d is the distance between the donor and the acceptor and n is a positive real number. Here, n is dependent on the geometry of the acceptor. It is expected to be 6 for point-like dipole pairs, 4 for 0D-2D pairs, 2 for 2D-2D pairs, and 3 for 0D-3D pairs [113, 114]. Such hybrid structures, fabricated by carefully selecting donor-acceptor pairs, can produce efficient energy transfer (ET)-based optoelectronic devices.

Colloidal semiconductor quantum wells (CQWs), or nanoplatelets (NPLs), which belong to the quasi-2D nanocrystals (NCs) family, are emerging as a new class of optoelectronic materials with excellent properties. NPLs are promising solution-processed atomically-flat NCs [115,116]. One salient feature is that these CQWs possess a large absorption cross-section [29]. These CQWs possess strong anisotropy in their physical dimensions [117,118]. NPLs have a vertical thickness of only a few nm's [119]. Their lateral dimension is several tens to hundreds of nm's, which is larger than the excitonic Bohr radius. The few monolayer vertical thickness results in strong one-dimensional confinement of excitons in these NPLs.

Quasi zero-dimensional colloidal quantum dots (QDs) have been adopted as an effective energy donor to pair with different acceptor platforms, including bulk silicon [38, 39], thin silicon membranes [40], 2D transition metal dichalcogenides (TMDCs) [58], and semimetals (e.g., graphene) [120], to name a few. NPLs are likely to outperform QDs as energy donors because NPLs possess higher intrinsic absorption cross-sections [59]. So far, the energy transfer studies with NPLs

involved have focused on the 2D-2D hybrid structures. There have been studies where NPLs act as the donor and the acceptor is also made of NPLs [60] or a 2D TMDC film [61]. Recently O. Erdem *et al.* have studied a 0D-2D hybrid structure in which QDs serve as the energy donors and NPLs form the acceptor layer [62].

A study based on the FRET in a 2D-3D hybrid structure, with silicon as the exciton-sinking medium, has not been explored at all to date. Silicon is generally used for building solar cells and photodetectors. Even though silicon is widely deployed for photovoltaic applications, it is a weak absorber. Silicon being an indirect-bandgap material, suffers from such relatively weak light absorption and this reduces the efficiency of such silicon-based light-harvesting systems. Sensitization with a strong light absorber like NPLs wherein these NPLs can absorb photons and, subsequently, transfer their energy through NRET to silicon can substantially enhance the poor absorption of silicon [40, 103, 104, 121].

We formed a 2D self-assembled array of CdSe/CdZnS core-shell NPLs on the silicon substrate in this thesis work. NPLs were deposited as a single monolayer using liquid-air interface self-assembly as explained in Section 2.2.2. Through this technique, we achieved the deposition of NPLs in the desired orientation of all face-down. Also, this technique helped in the formation of a single monolayer throughout the sample with minimum voids. Here FRET was studied as a function of the distance between CQWs and the silicon substrate. Thin alumina spacer was deposited with varying thicknesses using atomic layer deposition (ALD). This enabled us to systematically investigate the effect of separation on the decay kinetics of the donor NPLs. The FRET rate and efficiency were calculated from the measurements conducted using time-resolved fluorescence (TRF) spectroscopy. We found the distance scaling to be d^{-1}, where d is the distance between the donor NPLs and the surface of the silicon substrate. We performed full electromagnetic modeling to explain these results. The simulated trend of decay rates follows the experimental results. The expected distance scaling for FRET from a point-like donor to a 3D acceptor is d^{-3}. The FRET rate's distance scaling is expected to drop further to d^{-2} when the donor has 2-D geometry instead of being point-like. From simulations, we concluded that the observed distance

scaling of d^{-1} results from: (i) delocalized electric field due to the self-assembled monolayer of NPLs and (ii) the strong in-plane dipole present in the anisotropic NPLs.

4.1 Experimental Results and Discussion

The schematic representation of our proposed hybrid structure used in this thesis work is sketched in Figure 4.1a. Our system comprises NPLs and the silicon substrate separated by an alumina spacer. The separation between NPL dipole and the silicon substrate surface is defined as $d = d_L + t_{NPL/2} + t_{Al_2O_3} + t_{SiO_2}$. The length of the organic ligands is taken as $d_L = 2\ nm$, the thickness of the core/shell NPLs is $t_{NPL} = 4\ nm$, and the thickness of the native oxide layer present on the substrate is $t_{SiO_2} = 1.8\ nm$. Native oxide thickness was measured using ellipsometry. $t_{Al_2O_3}$ is the thickness of the Al_2O_3 spacer. The spacer was deposited using atomic layer deposition with thickness ranging from 1 to 50 nm. These thicknesses were regulated also using an ellipsometer.

The E-k diagrams of the direct-bandgap NPLs and the indirect-bandgap silicon are shown in Figure 4.1b. The photogenerated excitons in the NPLs can decay either through FRET or RET channels and return to the ground state. Since silicon is an indirect bandgap semiconductor, transitions from the ground to the excited state in silicon require a phonon to compensate for the momentum mismatch. As explained before, NPLs were deposited onto the substrates through our self-assembly method [122]. The purpose of using this deposition process was to make sure that the deposited NPLs was in the face-down orientation. Self-assembly also helped to avoid the formation of NPL multilayers, as shown in the scanning electron microscopy image in Figure 4.1c. The NPLs used in this study are made of $CdSe/Cd_{0.25}Zn_{0.75}S$ core/shell heterostructure. The synthesis was carried out using the hot injection method our group previously developed [123]. These NPLs have a square-like lateral area, with 17.2 ± 1.8 nm on a single side. Their vertical thickness was 4.4 ± 0.5 nm (with its TEM image shown in Figure 4.1d). Absorption and photoluminescence (PL) spectra of these

NPLs and the optical absorption of silicon are shown in Figure 4.1e. The absorption peak centered at 633 nm represents the electron-heavy hole transition. The absorption feature centered at 575 nm in the NPL absorption is attributed to the electron-light hole transition. The PL spectrum of the NPLs peaks at 640 nm with a full-width-half-maximum (FWHM) of 24 nm. Lastly, Figure 4.1f displays the photograph of all the samples irradiated by a UV lamp. Here, it can be seen that when NPLs are closer to the substrate, the emitted light is more quenched than when the emitters are further away from the substrate.

PL decay rates were collected through time-correlated single-photon counting (TCSPC) measurements at room temperature using a time-resolved fluorescence spectrometer (FluoTime 200, PicoQuant) as shown in Figure 4.2. The excitation source was a pulsed pump laser at a wavelength of 375 nm, having a pulse width 200 ps and a pulse repetition rate of 2.5 MHz. Fluorescence lifetimes were measured at the peak emission wavelength of the NPLs. The decays were fit to bi-exponential decays convolved with the instrument response function.

For calculating the rate and efficiency of the FRET, we needed PL decays of our samples. TRF measurements were performed on the set of samples shown in Figure 4.1f. The donor-only sample was prepared by depositing NPL film on the quartz. The decays are plotted in Figure 4.3a. It can be seen that donor lifetime progressively reduces with the decreasing spacer thickness. This result manifests the increasing strength of FRET from the NPL to the silicon substrate as the spacing shrinks. The NPLs-on-quartz structure is our reference sample where NPLs were deposited on a semi-infinite dielectric medium with no FRET possible. Decay kinetics of the donor exhibit a reduction in the lifetime as the emitters come nearer to the substrate. This demonstration suggests that the distance-dependent energy transfer is taking place.

From the decay curves, the decay lifetimes are extracted by using bi-exponential decay fitting curves:

$$I(t) = A_1 e^{(-t/\tau_1)} + A_2 e^{(-t/\tau_2)} \tag{4.2}$$

where A_i and τ_i are the amplitude and lifetime of the i^{th} decay component. After

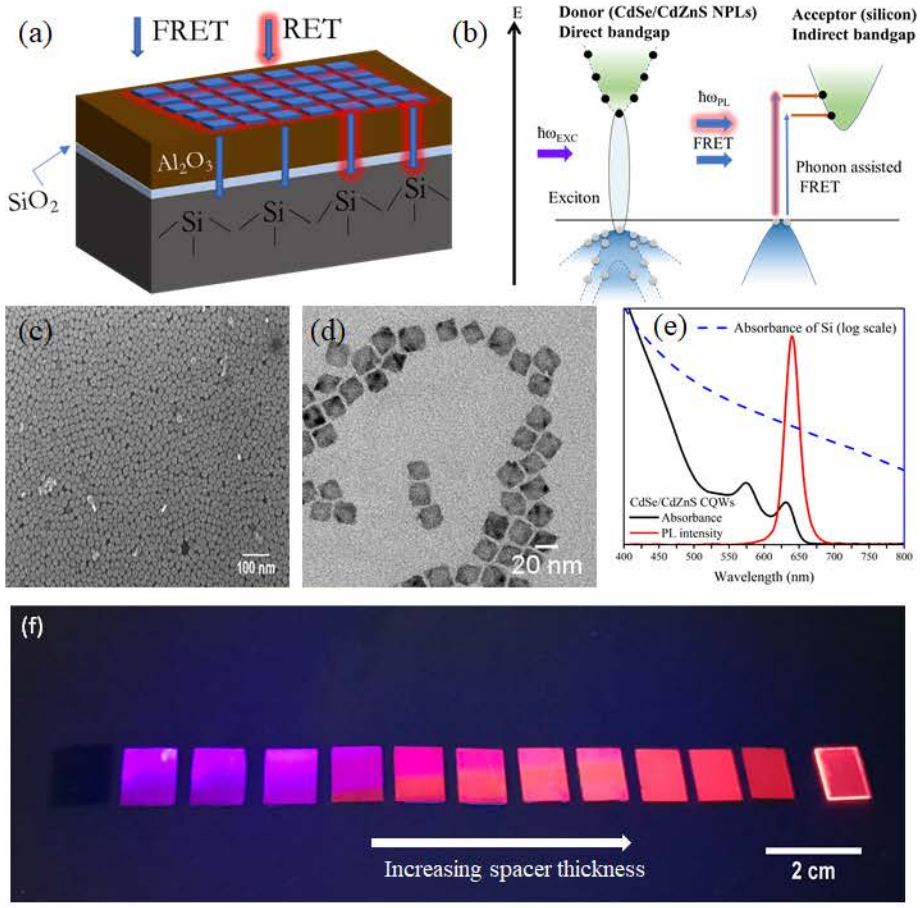

Figure 4.1: (a) Schematic depiction of our hybrid NPL-Al_2O_3-Si system. (b) Energy band diagram illustrating the energy transfer from NPLs to crystalline silicon. (c) Scanning electron microscopy image of self-assembled NPLs on the silicon substrate. (d) Transmission electron microscopy image of CdSe/CdZnS core/shell NPLs. (e) Normalized photoluminescence and UV-VIS absorption spectra of CdSe/CdZnS core/hot-injection grown shell NPLs (donor) and absorption spectrum of silicon. (f) Photography of the samples illuminated by a 365 nm UV lamp: Samples are placed from left to right in the order of increasing Al_2O_3 spacer thicknesses. Reproduced with permission from Ref. [83] Copyright 2021, Wiley.

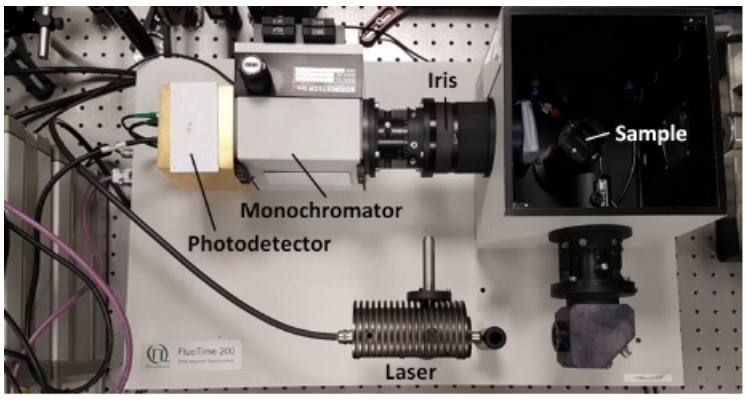

Figure 4.2: Photograph of the time-resolved spectrometer. Reprinted with permission from Ref. [80].

fitting, we obtained amplitude-averaged lifetimes which are found by using the following expression:

$$\tau_{avg} = \frac{A_1\tau_1 + A_2\tau_2}{A_1 + A_2} \tag{4.3}$$

The amplitude-averaged lifetimes are plotted in Figure 4.3b. The data fittings are shown in Table 4.1. The donor-only sample was found to have an average lifetime of 10.93 ns. The average lifetime reduces to 5.86 ns when the spacer thickness is only 1 nm. From Figure 4.3b, it can be observed that the magnitude of the average lifetime increases as the spacer thickness is increased, which means that the coupling of the NPL dipole field with the silicon is growing progressively stronger. This coupling produces an additional nonradiative channel. As previously discussed, both DET and FRET are nonradiative processes. Therefore, this new channel could be due to the charge transfer between NPLs and the silicon substrate. However, we know that charge transfer requires distance separation on the order of 1 nm, which is impossible in our hybrid configuration since a native oxide layer (2 nm) is present on the substrate [42]. NPLs have also been passivated by organic ligands, which are approximately 2 nm long.

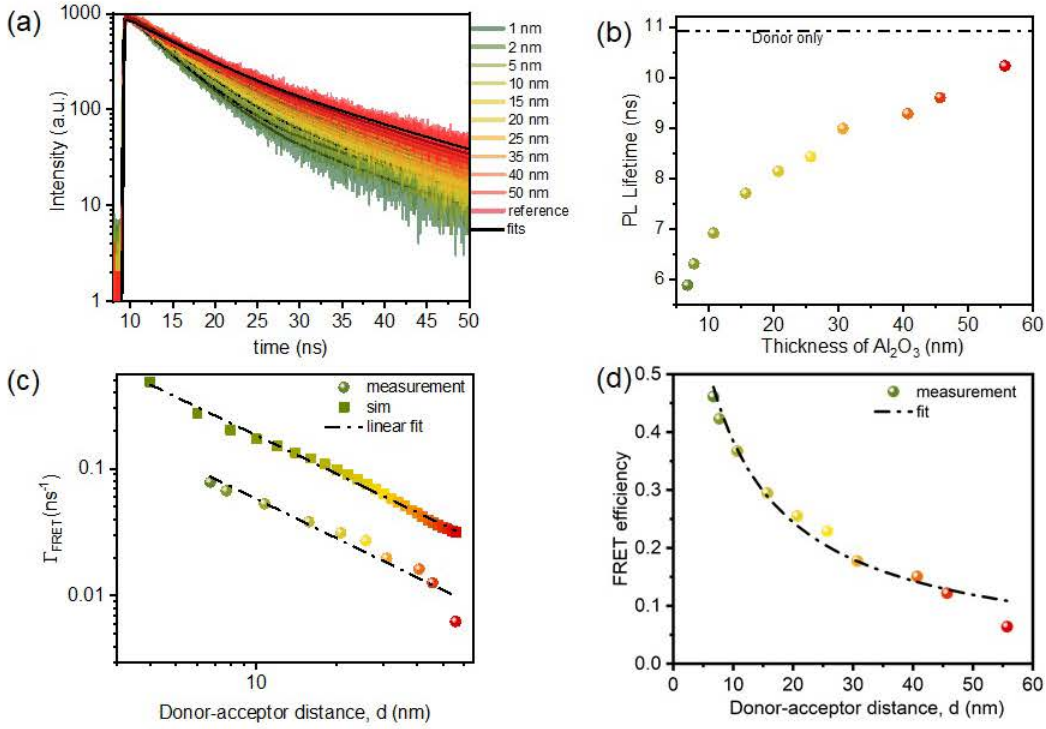

Figure 4.3: (a) PL decay curves of the solid films collected at the donor PL emission peak with varying thickness of the Al_2O_3 separation layer. The solid black lines represent the fits of the curves. (b) Amplitude-averaged lifetimes of the solid samples as a function of the spacer thickness. The dashed line indicates the donor-only lifetime. (c) FRET rates, obtained from measured lifetimes and through electromagnetic solutions, as a function of the center-to-surface distance between the donor and the acceptor plotted on a logarithmic scale. The black dashed line is the linear fitting. (d) FRET efficiency as a function of the center-to-surface distance between the donor and the acceptor. The black dashed line is the fitting obtained using Equation 4.6. Reproduced with permission from Ref. [83] Copyright 2021, Wiley.

Table 4.1: TRF decay parameters. Reproduced with permission from Ref. [83] Copyright 2021, Wiley.

Sample (spacer thickness)	A_1	τ_1 (ns)	$A_1 * \tau_1(\%)$	A_2	τ_2 (ns)	$A_2 * \tau_2(\%)$	τ_{avg} (ns)
1	1015.4	4.87	90.00	112.9	15.07	10.00	5.89
2	961.1	4.87	88.13	129.4	17.00	11.87	6.31
5	981.4	5.49	86.47	153.5	16.05	13.53	6.92
10	936.0	5.96	83.43	185.9	16.53	16.57	7.71
15	923.5	6.35	82.62	194.2	16.64	17.38	8.14
20	897.9	6.43	80.62	215.8	16.76	19.38	8.43
25	803.4	6.60	77.63	231.5	17.30	22.37	8.99
35	849.3	6.78	77.64	244.7	17.96	22.36	9.28
40	860.1	6.93	76.77	260.2	18.43	23.23	9.60
50	814.1	7.36	75.60	262.8	19.12	24.40	10.23
reference	701.1	7.32	69.55	306.9	19.17	30.45	10.93

From the decay lifetimes, we can calculate the experimental FRET rates, k_{FRET}, as:

$$k_{FRET} = \frac{1}{\tau_{FRET}} = \frac{1}{\tau_{DA}} - \frac{1}{\tau_D} \tag{4.4}$$

where τ_D is the lifetime of the donor-only sample (quartz substrate) and τ_{DA} is the donor lifetime when the substrate is silicon. k_{FRET} as a function of the donor-acceptor distance (d) is shown in Figure 4.3c. The logarithmic scale was used for plotting and a slope of -1.02 was obtained using the linear fitting. This slope represents the distance scaling. In our NPL-Al_2O_3-Si hybrid system, we observe that the strength of FRET is noticeably less sensitive to the distance.

FRET efficiency, η_{FRET}, is calculated as follows:

$$\eta_{FRET} = 1 - \frac{\tau_{DA}}{\tau_D} \tag{4.5}$$

For distance dependency, we can use the following FRET efficiency expression:

$$\eta_{FRET} = \frac{1}{1 + (d/d_0)^n} \tag{4.6}$$

where d_0 is the Förster radius and n is the exponent representing the distance dependency of the FRET. By numerically fitting Equation 4.6 to the data obtained from Equation 4.5, we found d_0 to be 6.1 nm and n = 0.95. Therefore, we conclude that: (i) FRET prevails in our system and (ii) the energy transfer scales with the inverse of the NPL dipole-silicon separation.

4.2 Numerical Results

The full numerical electromagnetic solution was performed to develop insight into these measurement results. From the simulations, we computed the FRET rates using the following expression [61, 124–127]:

$$k_{FRET} = \frac{2Im(\varepsilon_{si}(\omega))}{4\pi\hbar} \int \boldsymbol{E}.\boldsymbol{E}^{*} dv \tag{4.7}$$

where $\varepsilon_{si}(\omega) = 16 + j0.3$ is the complex dielectric constant of silicon at the peak emission wavelength of the donor NPLs [128] and $\boldsymbol{E}$ is the induced electric field distribution. The integration is performed over the acceptor region. The dielectric constant of NPLs was taken to be that of bulk CdSe at the peak emission wavelength of the NPL. To model multiple dipoles case, simulations were carried out by placing four dipoles at the center of the NPL layer. They form vertices of a unit square whose side lengths equal the center-to-center distance between the two neighboring NPLs. The presence of the ligands was taken into account. We also simulated a single dipole present in the NPL layer. By simulating the electric field distribution, we evaluated the FRET rate using Equation 4.7, from which it can be seen that the decay rate is proportional to the imaginary component of the dielectric function of the acceptor medium and the integrated intensity in the acceptor layer due to the radiating dipole. All simulations were carried out for both in-plane and out-of-plane dipole orientation. The average FRET rate is [87]:

$$k_{FRET} = \frac{(2k_{\parallel} + k_{\perp})}{3} \tag{4.8}$$

where $k_{\parallel}$ and $k_{\perp}$ are the rate of FRET due to the in-plane and out-of-plane dipoles, respectively.

It is essential to point out that the donor-acceptor separation in our system is considerably smaller than the emission wavelength of the NPL dipole. Therefore, the presence of the far-field ET mechanism can be ruled out. Thus, we do not expect the generation of electron-hole pairs in the silicon layer due to photons emitted by the excited NPLs. The comparison between the measured and simulated FRET rates is shown in Figure 4.3c. The slope obtained from linear fitting

of the simulated FRET rate data is -1.01, hence, following the same trend as the experimental results. There is a mismatch in the magnitude which can be attributed to the simplifications we adopted to facilitate our simulations. In setting up our numerical model, we did not include the thin native oxide layer. Also, we did not model the ligands attached to the NPLs. Additionally, we assumed that nanocrystals form a perfect 2D layer. We have left out the possibility of the presence of voids and edge effects from individual NPLs.

In addition, we obtained the electric field intensity inside our hybrid structure to investigate field distribution inside our system. We analyzed the field distributions for both in-plane and out-of-plane dipole orientations. We also examined the effect of varying spacer thickness. We found that the silicon's electric field intensity is more delocalized for the in-plane orientated dipole. Also, when the source is an in-plane orientated dipole, fields in the silicon region penetrate deeper and drop more gradually than an out-of-plane dipole. From this, we concluded that it is the in-plane dipole orientation that favours slowly declining energy transfer over space.

Figure 4.4 exhibits the electric field intensity inside the NPL layer when dipoles are oriented in-plane. Figure 4.5 exhibits the electric field intensity inside the NPL layer when dipoles are oriented out-of-plane. We observe the enhancement in the electric field delocalization with the multiple dipoles present and oriented in-plane. Figure 4.6 displays the electric field distribution inside the silicon region in the xy-plane 2 nm below the surface for Al_2O_3 thicknesses of 2, 20, and 50 nm for the in-plane oriented dipole. Figure 4.7 displays the electric field distribution inside the silicon region in the xy-plane 2 nm below the surface for Al_2O_3 thicknesses of 2, 20, and 50 nm for the out-of-plane oriented dipole. We find out that the electric field spreads more across the silicon layer for multiple dipoles sources. The reduction in the electric field intensity for multiple in-plane oriented model is lesser compared to the rest. We also look at field maps along the xz cross-section inside the silicon layer for the spacer thickness of 2, 20, and 50 nm. The in-plane and out-of-plane field maps are shown in Figure 4.8 and Figure 4.9, respectively. When the dipole is oriented in-plane, the electric field enters farther inside the silicon layer. At the same time, the field intensity is stronger and delocalized.

In our previous work, it was shown that the FRET rate's distance dependence to be d^{-2} for a hybrid structure consisting of NPLs and 2D MoS_2 monolayer [61]. Herein, we have extended the acceptor geometry in the 3^{rd} dimension by using a bulk silicon substrate. We see that the FRET rate distance sensitivity decreases. We observe that the dominant dipole components are oriented along lateral dimensions of the NPL in these self-assembled 2D NPL layers. Therefore, (i) the electric field delocalization due to the coupling in the NPL layer and (ii) electric field distribution in the bulk silicon layer induced by the in-plane oriented dipoles present in the NPL layer is credited for the energy transfer rate scaling with 1/d.

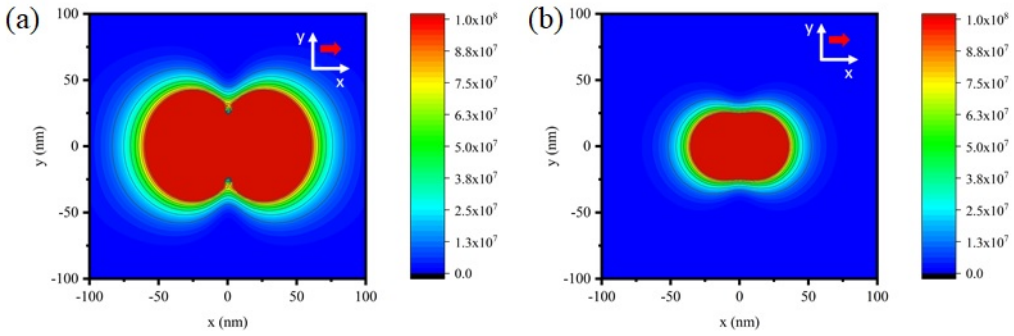

Figure 4.4: Electric-field intensity at the NPL layer: (a) 4 uniformly distributed dipoles present when oriented in-plane and (b) single dipole oriented in-plane. Reproduced with permission from Ref. [83] Copyright 2021, Wiley.

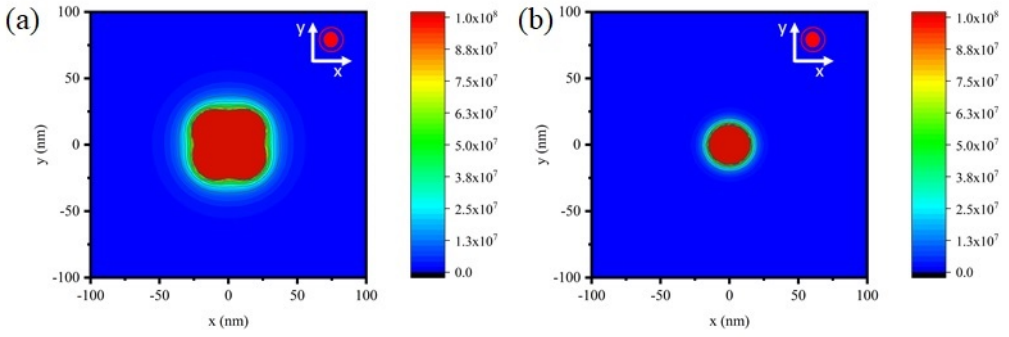

Figure 4.5: Electric-field intensity at the NPL layer: (a) 4 uniformly distributed dipoles present when oriented out-of-plane and (b) single dipole oriented out-of-plane. Reproduced with permission from Ref. [83] Copyright 2021, Wiley.

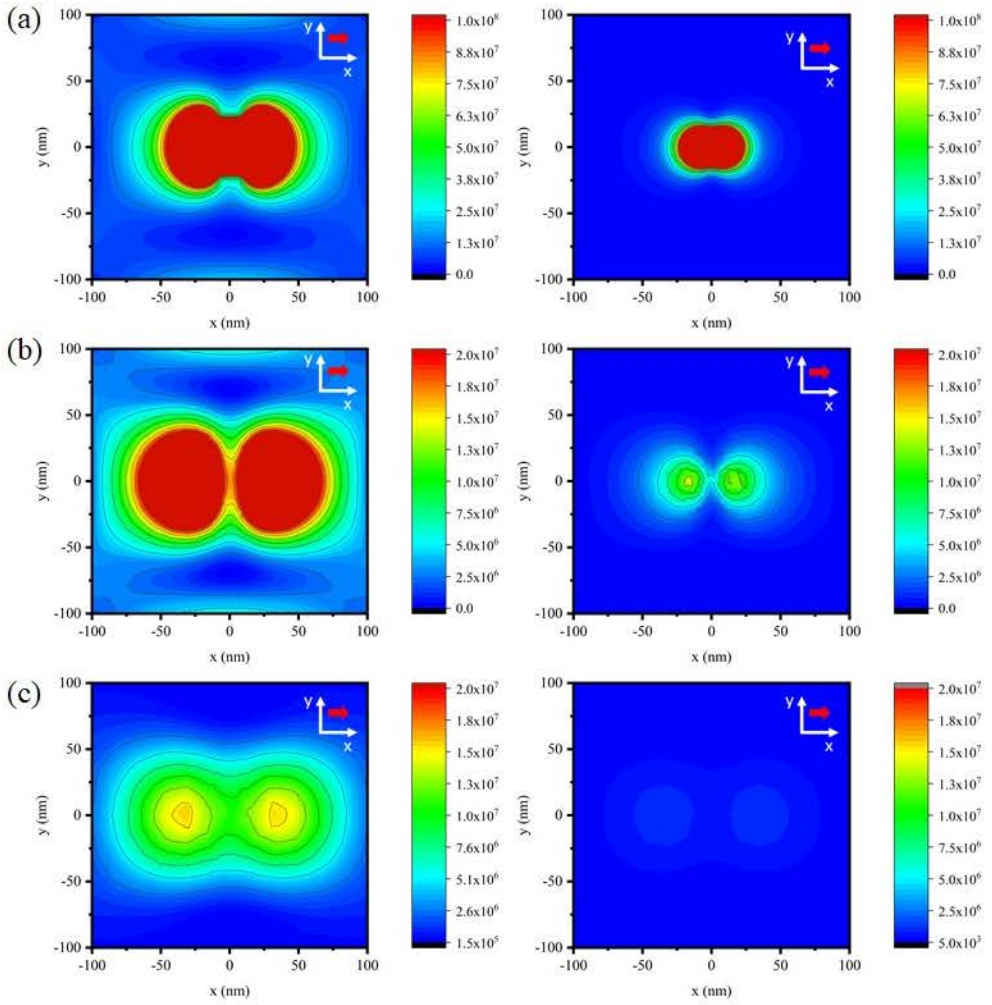

Figure 4.6: Comparison between $|\mathbf{E}|^2$ field distribution on the xy-plane within silicon region 2 nm below the surface for 4 uniformly distributed dipoles present, when oriented in the plane (left column), with that of single dipole oriented in-plane (right column) with Al_2O_3 spacer thickness of (a) 2 nm, (b) 20 nm, and (c) 50 nm. Reproduced with permission from Ref. [83] Copyright 2021, Wiley.

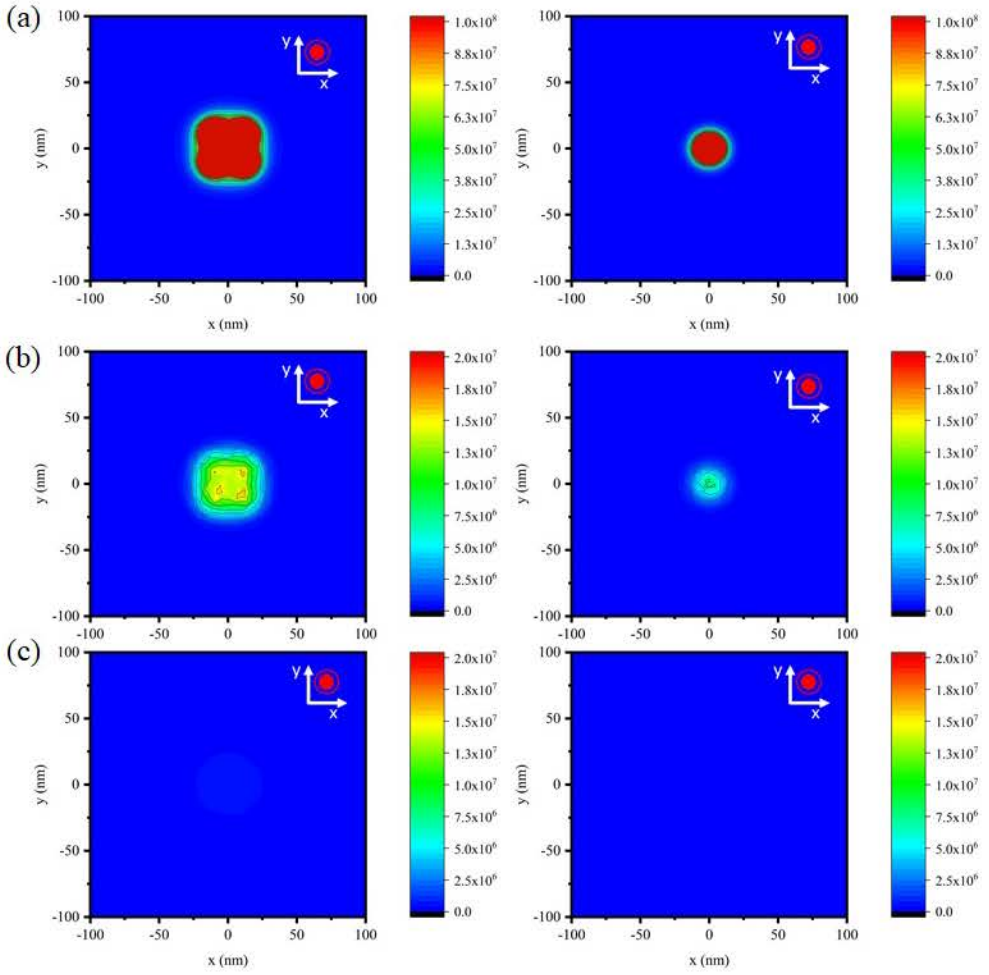

Figure 4.7: Comparison between $|\mathbf{E}|^2$ field distribution on the xy-plane within silicon region 2 nm below the surface for 4 uniformly distributed dipoles present, when oriented out-of-plane (left column), with that of single dipole oriented out-of-plane (right column) with Al_2O_3 spacer thickness of (a) 2 nm, (b) 20 nm, and (c) 50 nm. Reproduced with permission from Ref. [83] Copyright 2021, Wiley.

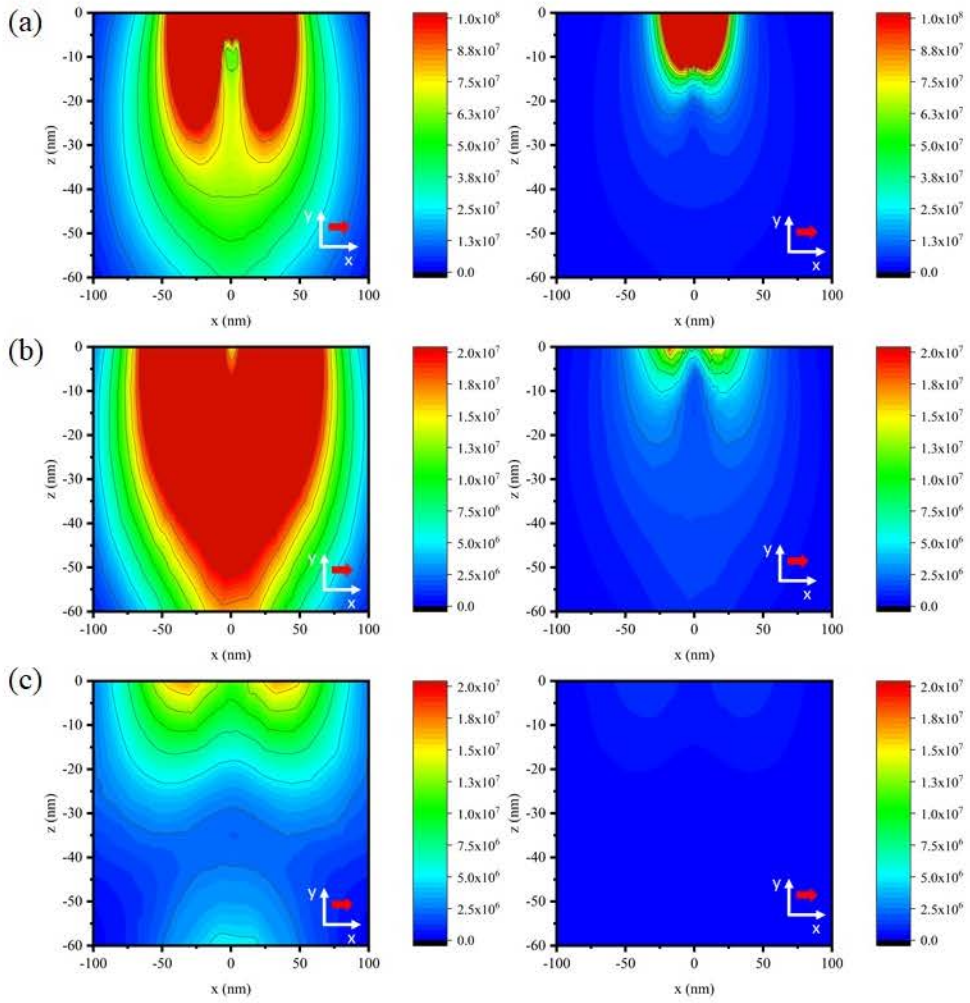

Figure 4.8: Electric field intensity distribution on the xz-plane (y = 0) within silicon region for 4 uniformly distributed dipoles present, when oriented in the plane (left column), with that of single dipole oriented in-plane (right column) with Al_2O_3 spacer thickness of (a) 2 nm, (b) 20 nm, and (c) 50 nm. Reproduced with permission from Ref. [83] Copyright 2021, Wiley.

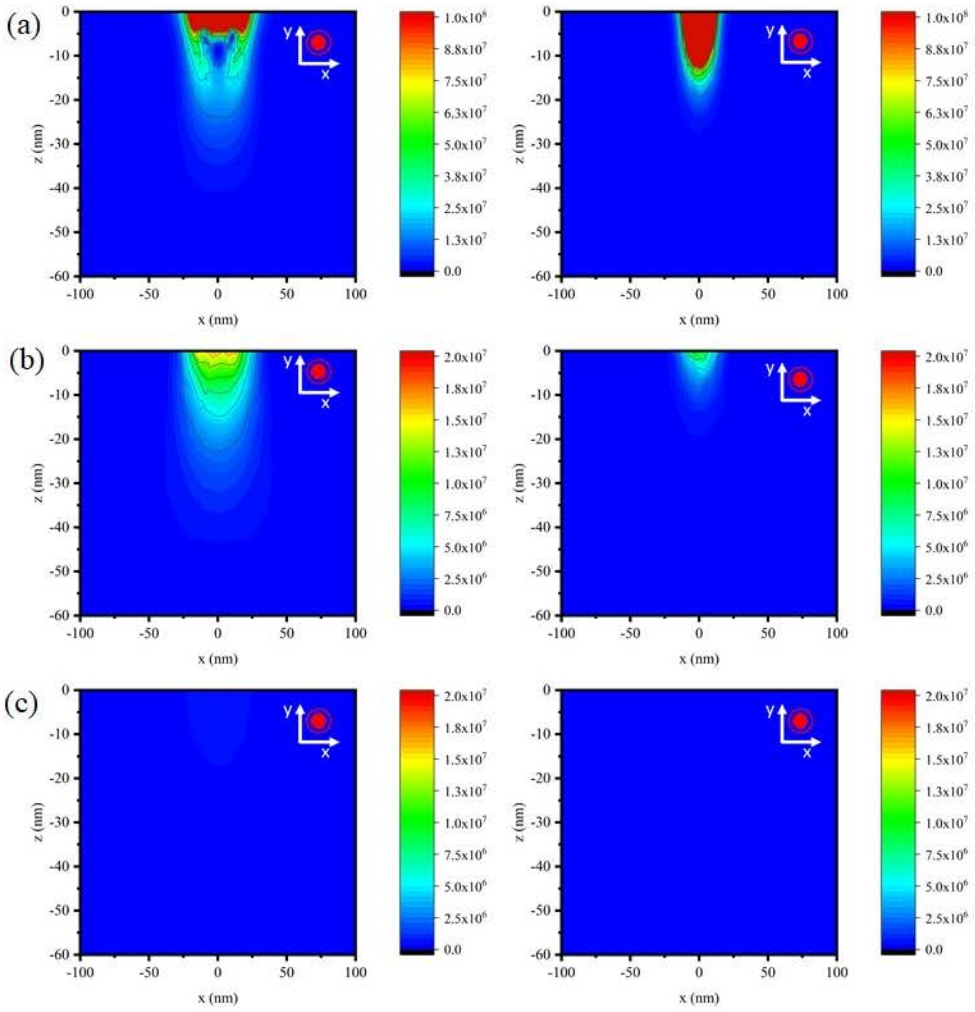

Figure 4.9: Electric field intensity distribution on the xz-plane (y = 0) within silicon region for 4 uniformly distributed dipoles present, when oriented out-of-plane (left column), with that of single dipole oriented out-of-plane (right column) with Al_2O_3 spacer thickness of (a) 2 nm, (b) 20 nm, and (c) 50 nm. Reproduced with permission from Ref. [83] Copyright 2021, Wiley.

Energy transfer can also be computed by using Purcell effect calculations. The expressions have been explained in detail in Section 2.4. We will henceforth be referring to the model as the CPS model. The electrodynamic framework was built to evaluate the emission of a dipole in the presence of the lossy medium [129]. A complex dielectric function characterizes the environment. The excitons in the NPLs are modeled as oscillating dipoles. A three-layer stratified model is set up to compute the decay rate of electric dipole placed in the upper half-space (Figure 4.10). The implementation of the CPS model on the three-layer stratified model provides closed-form integral expressions for the total, radiative, and non-radiative components of the decay rates normalized by the decay rate in the free space as expressed in detail in Section 2.4.

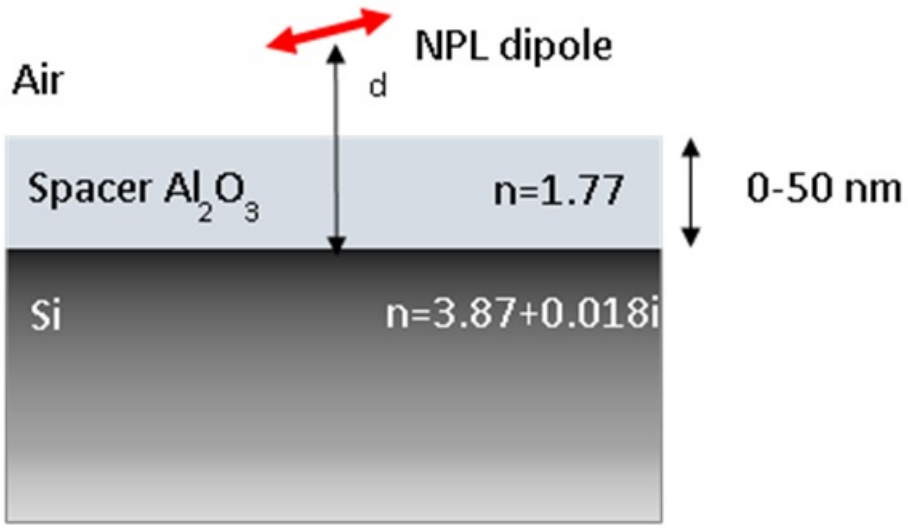

Figure 4.10: Cross-sectional diagram of the hybrid NPL-Al_2O_3-Si system for rate modification calculations.

To obtain the absolute rates, we need the decay rate of NPLs in the free space. To this end, we use the average lifetime obtained for the reference sample in the experiment. We extract theoretical lifetimes, τ_{DA}, from Equation 2.31 by utilizing the reference lifetime, 10.9 ns. Then τ_{DA} values are placed in Equation 4.5 to obtain the theoretical FRET efficiency. These results are numerically fitted using Equation 4.6. To extract the value of distance scaling parameter n that best matches the experimental distance dependency, we expressed the FRET efficiency as a parametric function of n only by keeping the d_0 value constant. Here d_0 was

fixed at the value obtained from experimental results, and a parametric sweep of variable n was performed. By varying n from 0.95 (which was the value found using experimental data) to 3 (which is distance scaling found in the literature for energy transfer between point-like dipoles to bulk acceptor), we found a family of curves that were plotted alongside the measurement results in Figure 4.11. The results obtained from the CPS theory are in close agreement with experimental results.

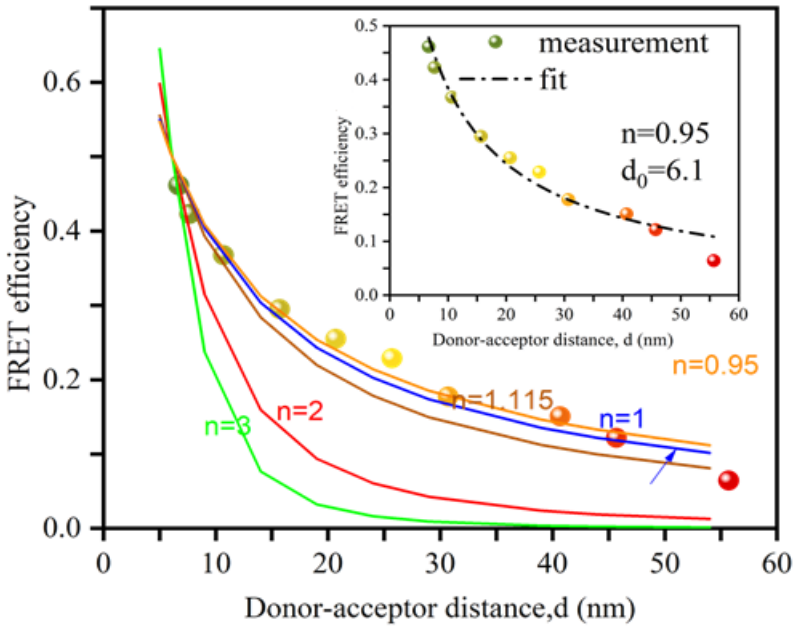

Figure 4.11: FRET efficiency as a function of the center-to-surface distance between the donor and the acceptor. The solid lines are FRET efficiency curves found using the lifetimes calculated based on the CPS model. Inset shows the FRET efficiency as a function of the center-to-surface distance with numerical fitting.

We perform a proof-of-concept demonstration by fabricating an NPL-sensitized silicon photodetector as shown in Figure 4.12a. An SOI wafer (50 nm thick Si device layer with a resistivity level of 8–11 ohm-cm, 200 nm thick buried oxide, and 0.75 mm handling layer) was used for fabricating NPL-sensitized silicon photodetector. The process flow is shown in Figure 4.13. P-type silicon-on-insulator (SOI) substrate was used for fabricating the device. RCA cleaning was employed

before the fabrication. Schottky contacts were made by thermally evaporating aluminum with a thickness of 100 nm using a photomask. The dimensions of the active region were 2.5 mm (width) × 1.5 cm (length). The alumina layer with the carefully controlled thickness (5, 10, and 50 nm) was deposited using ALD. Before ALD deposition Kapton tape was used to cover the AL contacts. Finally, a single monolayer of CdSe/CdZnS core-shell NPL film was deposited using our self-assembly method.

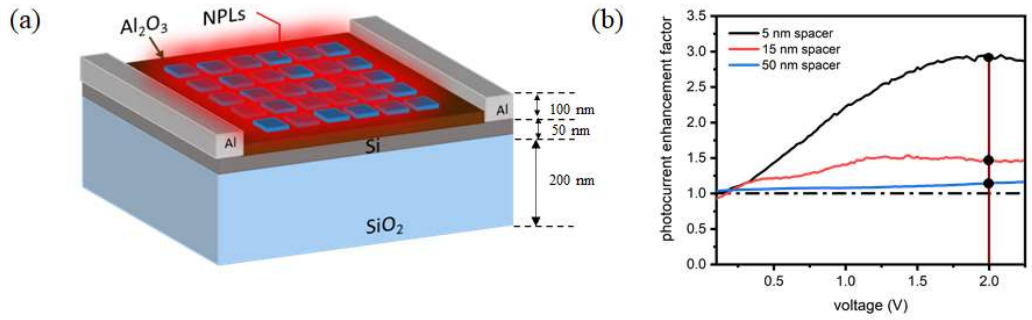

Figure 4.12: (a) Schematic of our proof-of-concept device. b) Photocurrent enhancement due to the presence of NPLs atop an ultrathin Si photodetector with respect to the negative control group device with no NPLs. Photocurrent enhancement factor as a result of the NPL deposition for the spacer thicknesses of 5, 15, and 50 nm. Reproduced with permission from Ref. [83] Copyright 2021, Wiley.

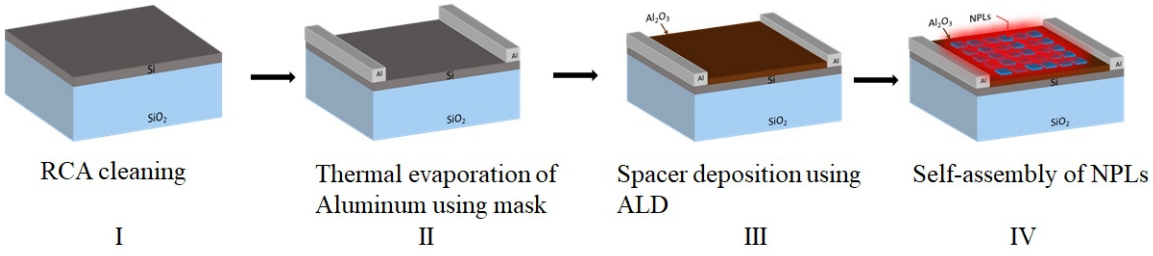

Figure 4.13: The process flow for fabricating our simple photodetector device. Reproduced with permission from Ref. [83] Copyright 2021, Wiley.

Photocurrent measurements were performed at room temperature. The dark current and photocurrent were measured under the 1 Sun AM1.5G condition by using a home-built 2-point electrical probe station equipped with a semiconductor device analyzer (Keysight B1500A) and a solar simulator (Newport 67005).

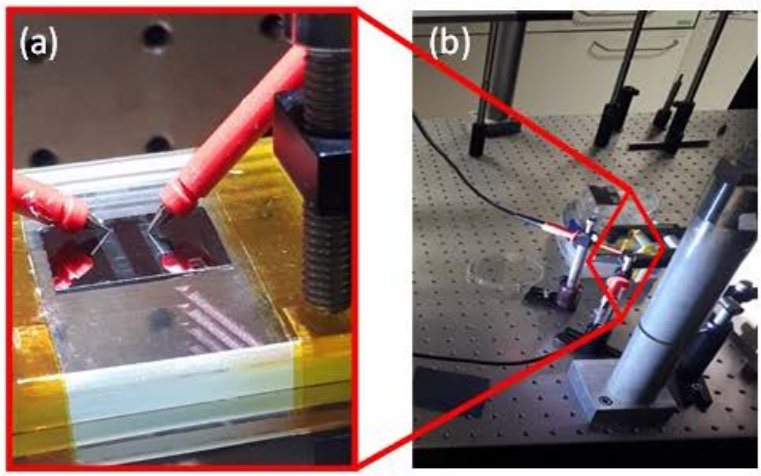

Figure 4.14: (a) Device under test using 2-point probes in contact with the Al Schottky contacts. (b) Photocurrent measurement setup configuration. Reproduced with permission from Ref. [83] Copyright 2021, Wiley.

Figure 4.14 shows the setup used for photocurrent measurement. Figure 4.12b presents the photocurrent enhancement factor for the spacer thicknesses of 5, 15, and 50 nm. The enhancement factor is calculated taking the ratio of the photocurrent before and after NPL deposition. We observe an overall improvement in the photocurrent for all spacer thickness with the best performance for the 5 nm thick one. This case has a maximum enhancement of 3 times (300 %) at 2 V bias. These results demonstrate that photosensitization of the silicon using NPLs can enhance photocurrent. Improving the optical response of silicon can greatly benefit photovoltaic and other optoelectronic applications.

4.3 Summary

In summary, we experimentally studied the 2D-3D donor-acceptor system where we investigated the effect of the indirect-bandgap silicon substrate on the emission kinetics of the colloidal quasi-2D quantum wells. We systematically tuned the separation between the self-assembled NPL monolayer and the substrate surface by depositing the Al_2O_3 spacer layer using ALD. FRET was found to be dominant for the modification of the PL decays. Our experimental results revealed that the photosensitization of silicon with a monolayer of quasi-2D nano-emitters results in energy transfer rates inversely proportional to the distance between the NPLs and the silicon substrate. The experimental results were further corroborated using a full numerical electromagnetic solution, which demonstrated that the d^{-1} dependence is due to electric field delocalization owing to the strong in-plane dipoles in the NPLs. These findings indicate that such face-down oriented NPL assembly is highly favorable for strong NRET-based photosensitization on Si towards enhanced light-harvesting.

Chapter 5

Modified Emission Kinetics of Colloidal Quantum Wells in the Vicinity of Metal Nanoparticles

More than a hundred years have passed since the introduction of the Mie theory. In recent times, the focus has shifted on controlling optical energy at the nanoscale using sub-wavelength metallic and dielectric structures. The older studies focused on far-field behavior, but with the advancement in computation capability, combined with nanofabrication and the understanding of nano-optics, optical near-field can also be exploited for a wide range of modern optoelectronic applications including biosensors and photovoltaics.

The emission kinetics of quantum emitters can be modified by engineering their environment. Fermi's Golden rule, discussed in Chapter 2 (Section 2.4), reveals that the decay rate of the emitter can be amended by placing it in the proximity of a medium with increased electromagnetic local density of the states. The setting could consist of a cavity or a resonator. The Purcell factor, conveying the modification in the emission of a classical emitter, is given by [130, 131]:

$$F = \frac{6}{\pi^2}\left(\frac{\lambda}{2n}\right)^3 \frac{Q}{V} \tag{5.1}$$

where n is the refractive index, λ is the emission wavelength, Q-factor is the quality factor of the resonant structure for the mode, and V is the optical mode volume. Dielectrics and metals are the two such material categories conducive to providing such a photonic environment [132, 133]. Dielectric materials are used to build cavities that can enhance light-emitter interaction. Using these cavities, we can increase Q-factor and thus increase the Purcell factor in Equation 5.1. Metallic structures support localized surface plasmonic resonances (LSPR) in volumes much smaller than the diffraction limits, but possess poor Q-factor due to intrinsic losses in metals [134–136]. Thus, the Purcell factor is enhanced because of the reduced mode volume in Equation 5.1. Metal nanoparticles (MNPs) are preferred over continuous metal films because of the large surface-to-volume ratio and larger local field enhancement due to LSPR [137].

These enhanced fields, at the vicinity of the metal surface, can enhance the fluorescence of emitters through coupling as explained in Section 2.3.2.1 [138]. Plasmonic nanostructures such as MNPs, ultra-thin metal films, metal nano-islands, and roughened surfaces of thin metal films have demonstrated the capability to enhance fluorescence [139–141]. Fluorophores detection is dependent on their quantum yield, photostability, and autofluorescence [141] and metal enhanced fluorescence (MEF) has emerged as an appealing tool for fluorescence spectroscopy. Enhancement in the fluorescence emission and reduction in their lifetime aid in improved fluorophore detectability.

The electromagnetic field produced by these metallic nanostructures is the strongest at the surface and decreases exponentially in the perpendicular direction away from the surface. Therefore, the fluorescence-plasmon coupling is distance-dependent. The EM field enhancement factor (EF) is expressed as [142]:

$$EF = \frac{|\boldsymbol{E}(\boldsymbol{r},\omega)|^2}{|\boldsymbol{E}_0(\omega)|^2}\frac{g^{ph}(\boldsymbol{r},\omega')}{g_0^{ph}(\omega')} \tag{5.2}$$

where $\boldsymbol{E}$ is the electric field vector in the presence of the metal nanostructures,

$\boldsymbol{E}_0$ is the electric field vector in homogeneous medium, g^{ph} is the LDOS in the presence of the metal nanostructures, and g_0^{ph} is the local DOS (LDOS) in the homogeneous environment. The first term expresses the enhancement coming from an increase in the absorption at the frequency ω due to the increased local electric field and the second term represents the one originating from the modification in the DOS, e.g., due to the presence of a resonator, at the emitter's emission frequency ω'.

Given Equation 5.2, the enhancement should be most substantial near the metal particle. However, in reality, when the emitter is in the proximity, quenching is more pronounced due to the nonradiative processes that also accelerate. Also, we need to realize that lossy metals could reduce the enhancement due to the Purcell effect and may even result in quenching. Studies have shown that, using metals, fluorescence intensity can be quenched or enhanced and both radiative and nonradiative decay rates can be modified. Fluorescence-plasmon coupling is strongly distance-dependent.

5.1 Experimental Results and Discussion

The optical response of the MNPs depends on the material, size, shape, density of the NPs in the film, surrounding, and the substrate material [93, 143–145]. Silver (Ag) and gold (Au) have LSPR in the visible range among noble metals. Au is commonly used because of its chemical stability [146]. In this thesis, Au nano-islands were fabricated to investigate the modification in the photoluminescence decay kinetics of colloidal quantum wells (CQWs) via plasmonic coupling. The substrate used was quartz to nullify the possibility of FRET to the substrate that could also modify the decay of our quantum emitters through plasmonic interactions.

Au films were deposited using a thermal evaporator. The evaporation rate was kept very low during the deposition ($0.1 - 0.5$ Å/s). Subsequently, rapid thermal annealing (RTA) was applied, which created nano-islands. The Au nano-island

films were characterized using UV-Visible absorption spectroscopy.

A low-cost but high throughput method to produce metal nanostructures is based on using thermal dewetting. In the first step, an ultra-thin film is deposited on the substrate at a very low deposition rate ($\approx 0.1 - 0.2$ Å/s). In the next step, islands are formed through thermal dewetting (agglomeration), whereby using the annealing process, the thin film is broken into islands because of the Ostwald ripening and coalescence process [147–149]. The ultrathin metal films are unstable due to the high surface-to-volume ratio. Films dewet and voids are created to minimize the surface energies. When the thermal annealing is applied, these voids widen to create random nano-islands with diminished surface coverage (Figure 5.1a). The thickness of the film, annealing temperature, and substrate control the dewetting process. The annealing temperatures are kept well below the melting point of the metal [150, 151].

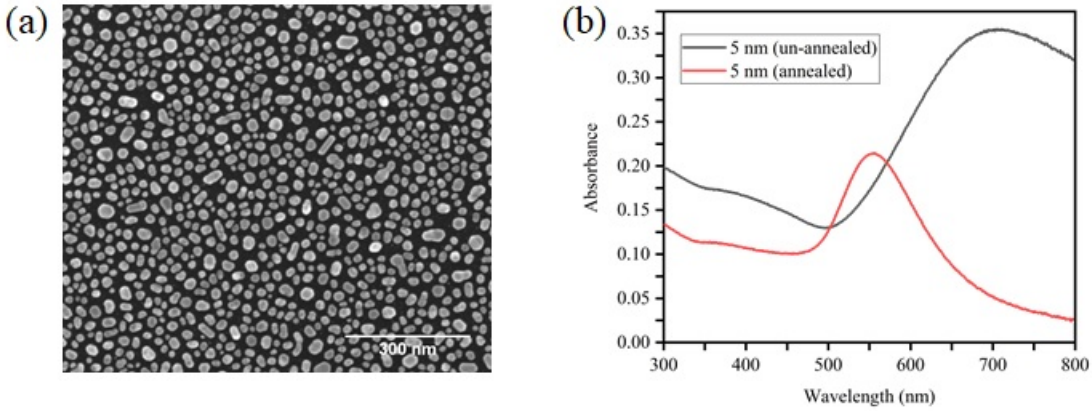

Figure 5.1: (a) SEM image of our Au nano-island structure on a silicon substrate. The mass-thickness of the as-deposited film was 5 nm deposited at a rate of 0.1Å/s. Post-deposition annealing was applied at 300 °C for 10 minutes. (b) Absorption spectra of an un-annealed discontinuous thin film vs. an annealed nano-island film.

The surface diffusivity of the metals affects the dewetting. Au has a very high diffusivity. Thus it is easy to form Au nano-islands [152]. Analysis of the absorption spectra of the as-deposited Au films shows that the films are discontinuous below the nominal thickness of 10 nm [153]. Figure 5.2a shows an SEM image of a 10 nm Au-evaporated sample where the grooves are visible.

Ultra-thin Au films (1-3 nm) feature nano-structures without annealing. Figure 5.2b shows the LSPR spectra of Au-evaporated samples of 1 nm and 2 nm in thickness, respectively. The extinction peaks at 550 nm and 580 nm are attributed to the plasmonic resonances of MNPs. For thicknesses (5 nm, 6 nm, and 8 nm) in Figure 5.3, the minimum optical density is present around 500 nm, followed by a large plateau in the near-infrared, a signature of semi-continuous plasmonic samples [154].

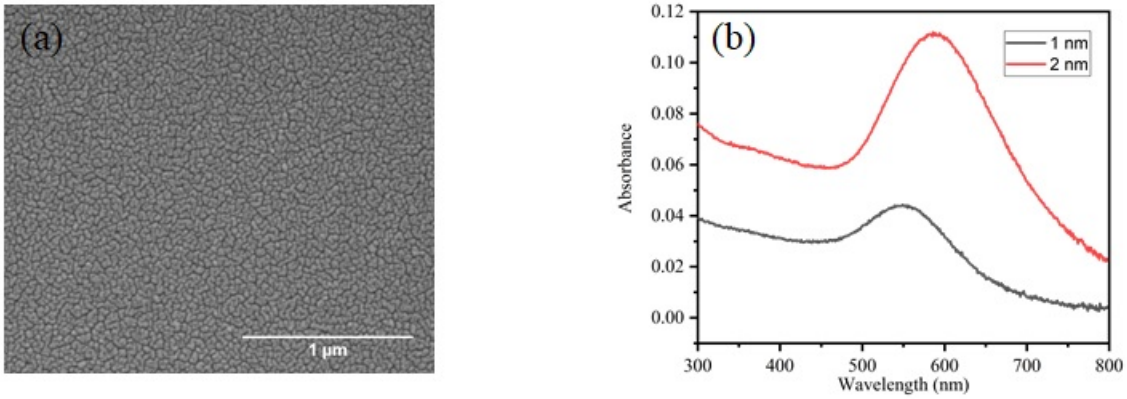

Figure 5.2: (a) SEM image of a 10 nm thick Au film as-deposited on quartz substrate. Evaporation was carried out at 0.5Å/s. 10 nm Au/Pd conductive film was coated on top to prevent the charging during SEM imaging. (b) Absorption spectra of the as-deposited ultra-thin 1-2 nm Au films.

The mass-thickness of the evaporated Au film and the annealing temperature are the fundamental parameters that define the LSPR properties and morphology of the nano-islands formed. With an increase in the nominal thickness, the nano-island size expands, resulting in a redshift in the LSPR wavelength and a rise in the LSPR intensity as shown in Figure 5.3 [155, 156].

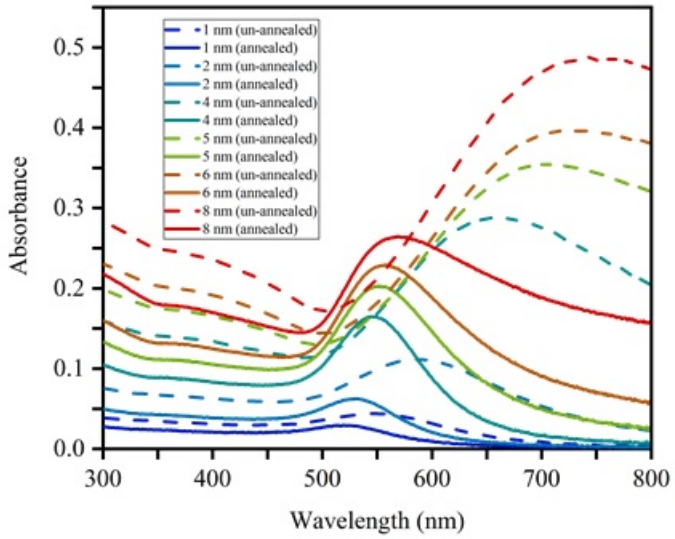

Figure 5.3: Absorption spectra of thermally evaporated Au films with different initial mass-thicknesses before (dotted lines) and after (solid lines) annealing. The annealing was applied at 300 °C for 10 minutes.

The absorption cross-section (C_{abs}) is proportional to:

$$\frac{\varepsilon_m^{3/2} Im(\varepsilon_p)}{[Re(\varepsilon_p) + 2\varepsilon_m]^2 + [Im(\varepsilon_p)]^2} \tag{5.3}$$

where ε_p is the complex dielectric constant of the metal nanoparticle, and ε_m is the dielectric constant of the surrounding environment. For most metals, $Re(\varepsilon_p)$ decreases with wavelength while $Im(\varepsilon_p)$ increases. Therefore, from Equation 5.3 with an increase in the permittivity of the surrounding medium, there is a redshift in the peak of absorption spectra, which becomes broader and the intensity increases (Figure 5.4).

The mechanism of improving the properties of chromophores using MNPs can be extended to the CQWs as well. CQWs exhibit exceptional optical and electronic properties. We can further modify their emission characteristics using plasmonic materials for optoelectronic applications. Here our goal is to modify fluorescence intensity and lifetimes using MNPs. Besides, CQWs exhibit large oscillator strengths making them ideally suited for such plasmonic coupling based hybrid structures. There are many studies of CQDs coupling with plasmonic

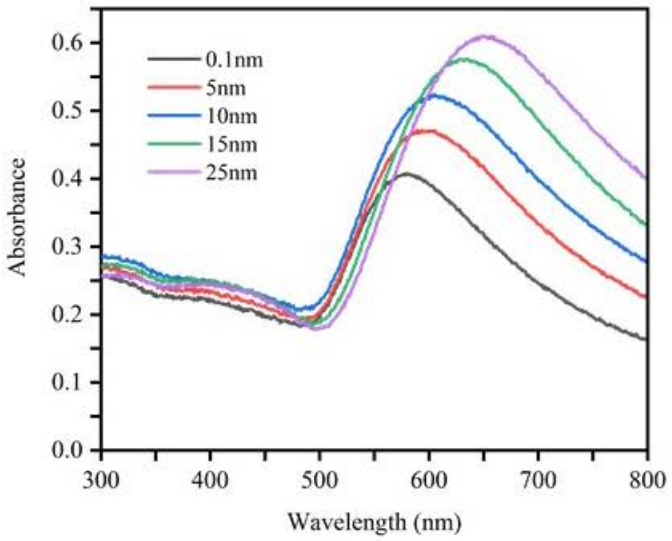

Figure 5.4: Absorption spectra of thermally evaporated Au films with initial mass-thickness of 8 nm, annealed at 650 °C for 3 minutes, followed by Al_2O_3 deposition of varying thicknesses using ALD at 200 °C.

structures [63,64,157–161]. Some studies involving CQWs do exist but they have mostly focused on the strong coupling [162, 163].

In this thesis work, the mass-thickness of 8 nm was selected to create Au MNPs after analyzing the LSPR wavelength and intensity. Dewetting was applied at 650 °C because the higher temperatures favor the creation of more homogeneous nanostructures than the lower temperatures [164, 165]. Figure 5.5a shows the SEM image of the Au film after annealing. The SEM image taken at a tilt angle of 50 ° (Figure 5.5b) depicts the round morphology of the resulting NPs, which is a signature of annealed metal-island films [146].

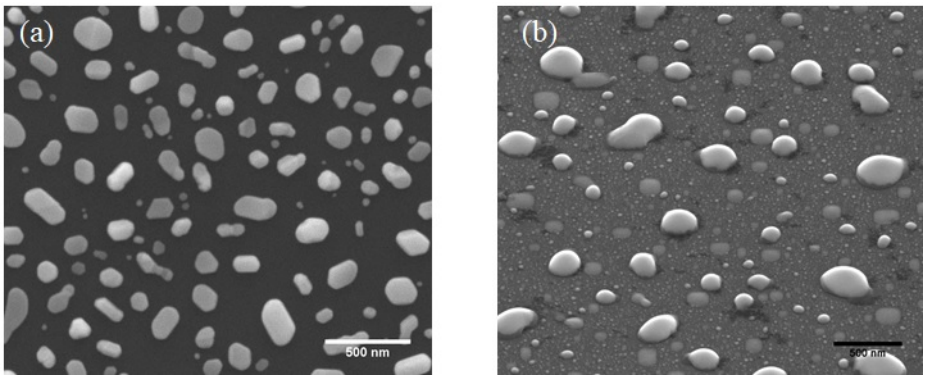

Figure 5.5: SEM images of Au nano-island films: (a) image taken without tilt and (b) image taken at 50 ° tilt angle.

CdSe/ZnS core/shell NPLs were used to study the plasmon-exciton coupling. The NPLs were synthesized using the hot-injection method with their emission centered around 610 nm in solution. The NPLs were dispersed in hexane solvent. The optical characteristics are shown in Figure 5.6a. Al_2O_3 spacer was deposited using atomic layer deposition (ALD) at 200 °C. The dielectric spacer thicknesses were confirmed using ellipsometry. The NPL solution was spin-coated onto the Al_2O_3/Au/quartz substrates. The reference sample was prepared by spin-coating NPLs directly on top of the quartz substrate.

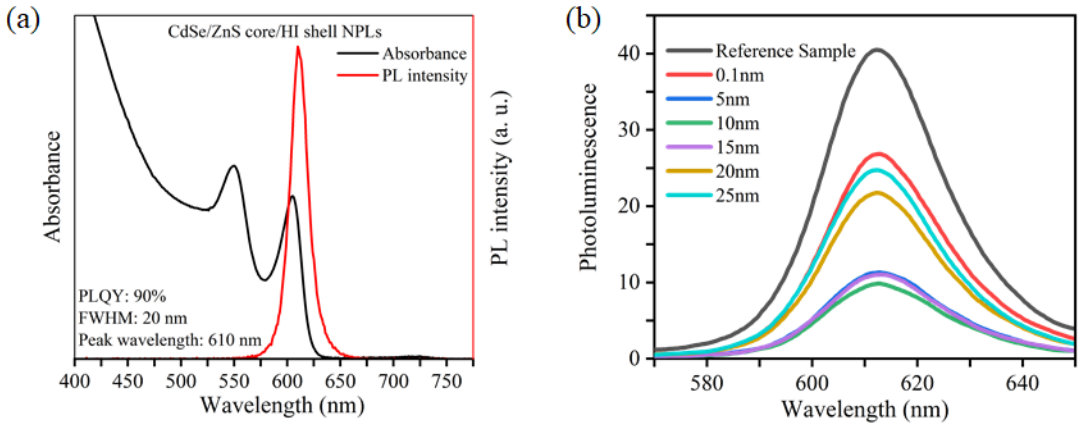

Figure 5.6: (a) Absorption and photoluminescence (PL) spectra of CdSe/ZnS NPLs. (b) PL spectra of solid films of the NPLs-Au assembly with varying thicknesses of the Al_2O_3 separation layer.

Standard PL spectrometer was used to measure the PL response of our samples. Figure 5.6b displays the PL emitted by the fabricated NPL/plasmonic structures. The emission from the NPL/plasmonic structures shows quenching relative to the reference sample for all spacer thicknesses. The effect of NPLs-MNPs interaction on NPL decay kinetics was further investigated by measuring the decay lifetime of the hybrid structures. Figure 5.7 shows the time-resolved fluorescence (TRF) decays measured at the peak emission wavelength of the NPLs using pulsed excitation at 375 nm. Decay kinetics exhibit a trend of lifetime shortening with the decrease in the spacer thickness. There is distance-dependent energy transfer taking place from NPLs to the Au nano-island film.

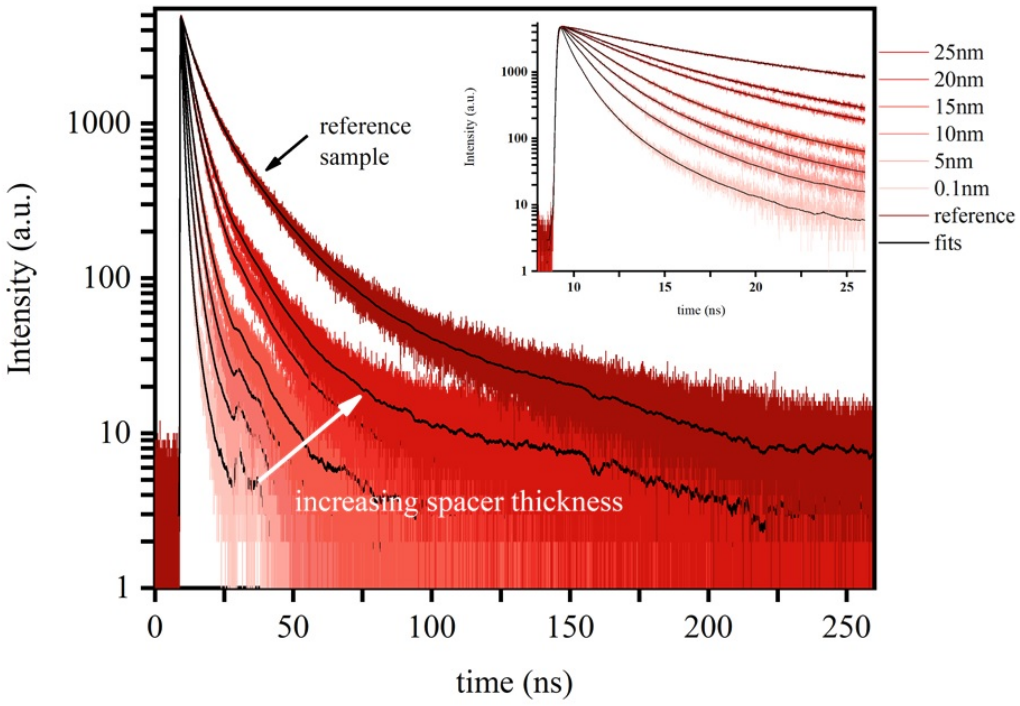

Figure 5.7: Time-resolved fluorescence decay curves of the solid films of the NPLs-Au assembly, collected at the donor PL emission peak of 610 nm with varying thicknesses of the Al_2O_3 separation layer. The solid black lines represent the fits of the curves. Inset shows the zoom-in representation of the same decay curves.

Decay lifetimes were extracted by using four-exponential decay fitting curves as:

$$I(t) = A_1 e^{(-t/\tau_1)} + A_2 e^{(-t/\tau_2)} + A_3 e^{(-t/\tau_3)} + A_4 e^{(-t/\tau_4)} \quad (5.4)$$

where A_i and τ_i are the amplitude and lifetime of the i^{th} decay component. The details of the contribution of the fluorescence decay components are given in Table 5.1. The amplitude-average lifetime (τ_{avg}) of the reference sample is 9.81 ns. For the minimum spacer thickness of 1 Å, τ_{avg} decreases by more than one order and is in the picosecond range (0.76 ns).

Table 5.1: TRF decay parameters when using CdSe/ZnS NPLs in the vicinity of Au NPs with systematically varied alumina spacer.

Sample (spacer thickness)	A_1	τ_1 (ns)	$A_1 * \tau_1$(%)	A_2	τ_2 (ns)	$A_2 * \tau_2$(%)	A_3	τ_3 (ns)	$A_3 * \tau_3$(%)	A_4	τ_4 (ns)	$A_4 * \tau_4$(%)	τ_{avg} (ns)
0.1	14.98	13.29	0.20	283.10	2.93	3.81	2144.00	1.09	28.83	4996.00	0.45	67.17	0.76
5	53.41	12.04	0.80	963.90	2.74	14.50	1086.00	1.53	16.34	4543.00	0.85	68.36	1.32
10	82.21	13.64	1.29	1473.90	3.17	23.10	2572.00	1.23	40.31	2252.00	1.23	35.30	1.84
15	10.05	38.60	0.16	213.80	10.84	3.49	2022.90	3.38	32.98	3886.00	1.59	63.37	2.56
20	36.89	40.09	0.61	559.20	11.27	9.32	2442.40	4.32	40.71	2961.00	2.15	49.35	4.12
25	52.80	46.21	0.89	823.20	12.12	13.88	3164.40	4.35	53.35	1890.00	2.26	31.87	5.13
reference	211.42	47.70	3.68	1973.80	14.57	34.33	2731.00	5.64	47.49	834.00	2.64	14.50	9.81

In addition, CdSe/CdZnS NPLs were also used to study the plasmon-exciton coupling. These NPLs were synthesized using the hot-injection method and their peak emission was at 646 nm in solution(Figure 5.8a).

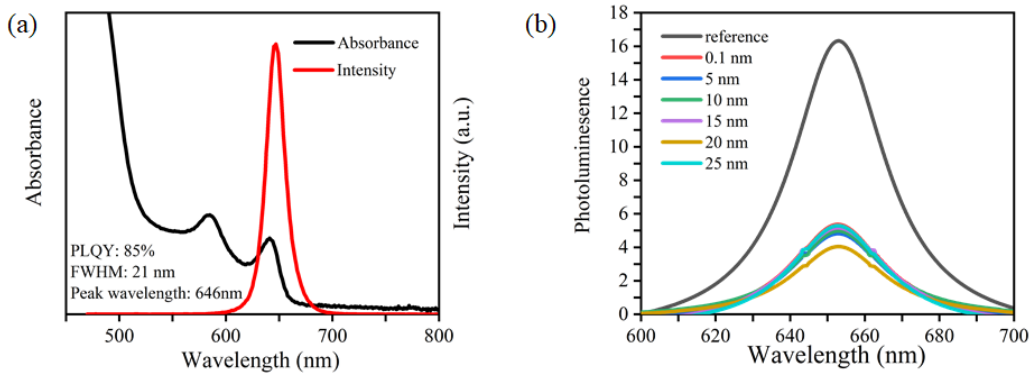

Figure 5.8: (a) Absorption and PL spectra of CdSe/CdZnS NPLs. (b) PL spectra of solid films of the NPLs-Au assembly with varying thicknesses of the Al_2O_3 separation layer.

Figure 5.8b displays the PL emitted by the fabricated NPL/plasmonic structures. This NPL/plasmonic system also showed quenching relative to the reference sample for all spacer thicknesses. NPL decay kinetics were investigated by measuring the decay lifetime of the samples. Figure 5.9 shows the TRF decays

measured at the peak emission wavelength of the NPLs. This set also exhibits a trend of lifetime decreasing with thinner spacer.

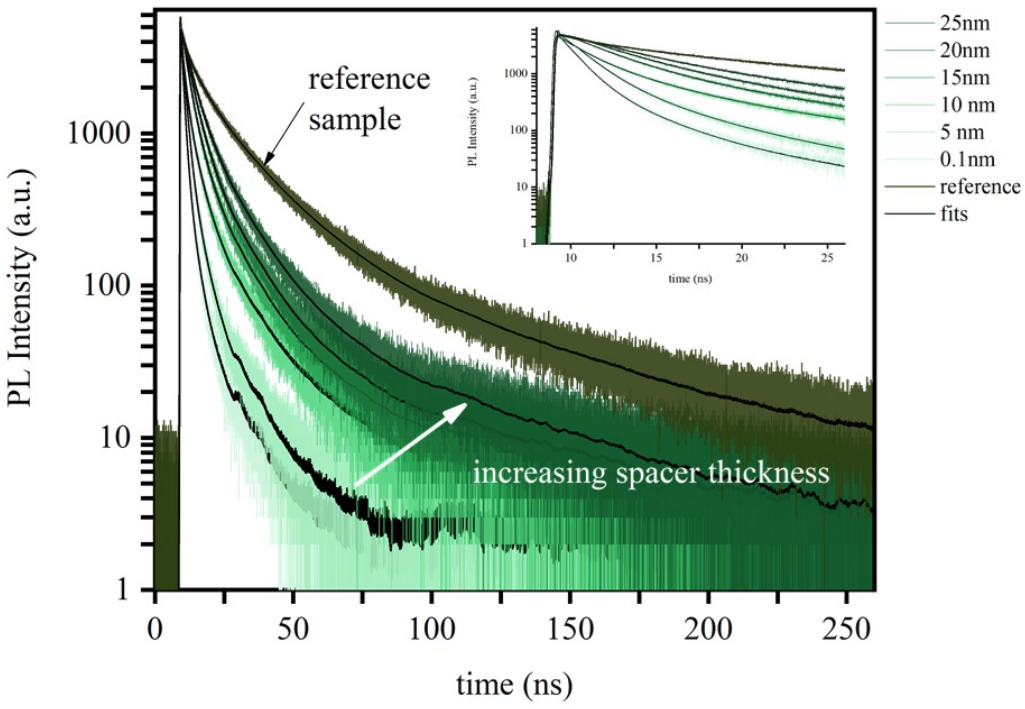

Figure 5.9: Time-resolved fluorescence decay curves of the solid films of the NPLs-Au assembly, collected at the donor PL emission peak of 650 nm with varying thicknesses of the Al_2O_3 separation layer. Inset shows the zoom-in representation of the same decay curves.

Here also decay lifetimes were extracted by using four-exponential decay fitting curves. The details of the contribution of the fluorescence decay components are given in Table 5.2. τ_{avg} of the reference sample is 12.42 ns. For the minimum spacer thickness of 1 Å, τ_{avg} decreases to 1.48 ns.

Table 5.2: TRF decay parameters when using CdSe/CdZnS NPLs in the vicinity of Au NPs with systematically varied alumina spacer.

Sample (spacer thickness)	A_1	τ_1 (ns)	$A_1 * \tau_1$(%)	A_2	τ_2 (ns)	$A_2 * \tau_2$(%)	A_3	τ_3 (ns)	$A_3 * \tau_3$(%)	A_4	τ_4 (ns)	$A_4 * \tau_4$(%)	τ_{avg} (ns)
0.1	21.48	22.50	0.37	149.20	6.72	2.58	961.10	2.66	16.64	4646.00	0.98	80.41	1.48
5	14.08	27.53	0.23	71.10	14.07	1.15	1023.60	4.27	16.50	5094.00	1.43	82.13	2.10
10	70.48	34.62	1.27	463.70	10.71	8.39	1774.60	4.05	32.10	3220.00	1.49	58.24	3.51
15	72.30	39.49	1.16	222.70	16.49	3.57	1431.00	7.48	22.91	4520.00	2.71	72.37	4.72
20	119.56	37.05	1.96	858.70	11.67	14.06	691.60	7.54	11.32	4438.00	3.54	72.66	5.79
25	197.33	37.90	3.28	11.60	21.30	0.19	1906.60	10.89	31.70	3900.00	3.89	64.83	7.26
reference	412.80	50.07	7.13	2220.10	17.01	38.35	1900.20	6.18	32.82	1256.00	1.36	21.70	12.42

All the experiments reported thus far use Al_2O_3 spacer. Since we only observed quenching, we also studied with the spacer made of SiO_2. Silica spacer was deposited using electron-beam evaporation. For comparing the two spacers, we kept the spacer thickness constant at 15 nm. Three different NPLs at different peak emissions were used in this study: (a) 5 ML CdSe core NPLs at PL emission peak of 552 nm (Figure 5.10a), (b) CdSe/CdS core/ shell NPLs. 4 ML CdSe core was used with 1ML CdS shell grown around it. The PL emission peak was at 602 nm (Figure 5.10b), and (c) CdSe/CdS core/ shell NPLs. 4 ML CdSe core was used with 2 ML CdS shell grown around it. The PL emission peak was at 628 nm (Figure 5.10c).

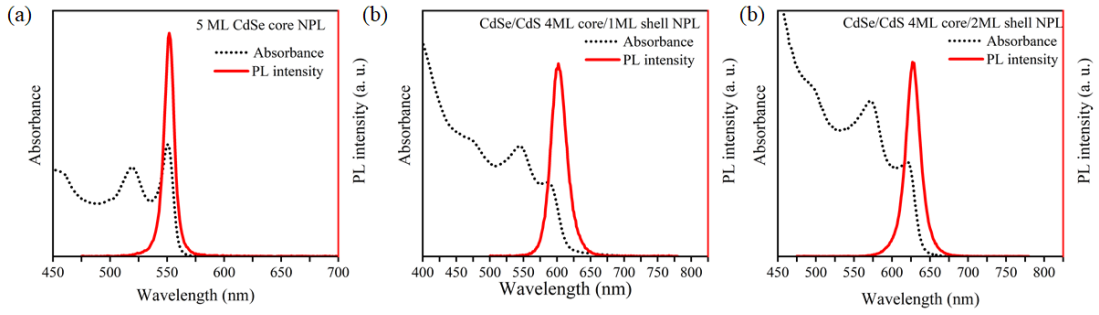

Figure 5.10: (a) Absorption and PL spectra of 5 ML CdSe core NPLs. (b) Absorption and PL spectra of CdSe/CdS 4 ML / 1 ML shell NPLs. (c)Absorption and PL spectra of CdSe/CdS 4 ML / 2 ML shell NPLs.

The as-deposited thickness of Au film was 8 nm. Annealing was undertaken at 650 °C for 15 minutes. The UV-visible spectra when using different spacer thicknesses are given in Figure 5.11. Compared to LSPR wavelengths shown in Figure 5.4, there is a blue shift occuring because of the extended annealing time [166]. Prolonged heating at high temperatures further ensures shape and structure regularity [145]. Enhancement is observed with the NPLs with emission

peaking at 602 nm and 628 nm when the silica spacer is used as compared to the alumina spacer (Figure 5.12). The enhancement factors are 1.67 (Figure 5.12b) and 2.9 (Figure 5.12c) respectively. The reason could be the higher refractive index of alumina, reducing the extent of the evanescent field [167].

(a)

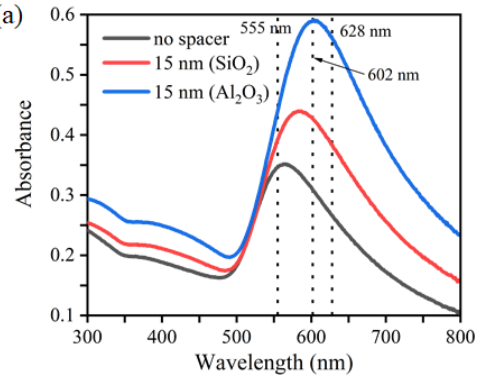

(b)

Sample	Peak wavelength (nm)
No spacer	565
15 nm (SiO_2)	584
15 nm (Al_2O_3)	603

Figure 5.11: (a) Absorption spectra of our thermally-evaporated Au films, post-deposition annealed at 650 °C for 15 minutes, followed by spacer deposition. The vertical lines show the PL maxima of NPLs used. (b) LSPR peak shifts with spacers of different materials having the same spacer thickness.

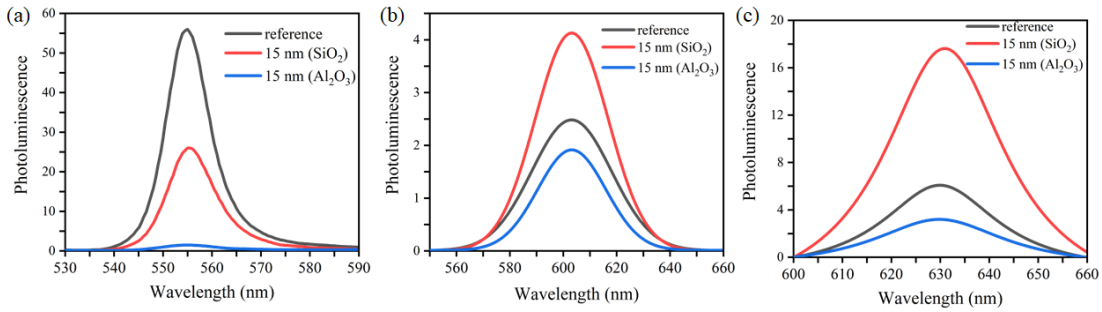

Figure 5.12: PL spectra of solid films of the NPLs-Au assembly with different heterostructures of NPLs (a) 5 ML CdSe core NPLs with an emission peak at 555 nm, (b) CdSe/CdS 4 ML / 1 ML shell NPLs with an emission peak at 602 nm, and (c) CdSe/CdS 4 ML / 2 ML shell NPLs with an emission peak at 628 nm.

Building on the discussion presented in Chapter 2 (Section 2.3.2.1) regarding MEF, we can increase the PL of CQWs either by increasing the excitation rate of the CQWs and/or by enhancing their emission rate [168]. The effect of the environment on the fluorophore decay kinetics can be summarized mathematically

using the following expression [56]:

$$\sigma(\omega) = \frac{4\pi^2\omega}{nc}|\boldsymbol{\mu}|^2\rho(\omega) \tag{5.5}$$

where $\sigma(\omega)$ is the absorption cross-section of the two-level system, $\boldsymbol{\mu}$ is the transition dipole of the emitter, and ρ is the DOS at the transition frequency ω. The total transition rate R is given by:

$$R = \sigma I_{exc} \tag{5.6}$$

where I_{exc} is the excitation intensity. An increase in I_{exc} results in a rise in the excited population, increasing the fluorescence intensity. This does not modify the decay kinetics of the fluorophore. This situation arises when the plasmon-enhanced EM field overlaps with the absorption spectrum of the emitter. However, the change in the emitter's absorption cross-section influences the emitter's decay kinetics. This modification is produced as a consequence of the exciton-plasmon coupling and can change both nonradiative and radiative decay rates of the fluorophores. This is achieved when the PL emission spectrum overlaps with the LSPR peak [169].

Another aspect we need to bear in mind is that in the resultant electromagnetically coupled system of fluorophore and MNPs, fluorophores have additional channels available for deexcitation. The total decay rate can be expressed as [56, 170]:

$$\frac{\gamma_{total}}{\gamma_0} = 1 + \frac{3}{2}Im\frac{\boldsymbol{\mu}.\boldsymbol{E}(\boldsymbol{r},\omega_0)}{|\boldsymbol{\mu}|^2|\boldsymbol{k}|^3} \tag{5.7}$$

where γ_0 is the free space decay rate, $\boldsymbol{k}$ is the free space wave vector, $\boldsymbol{\mu}$ is the emitter's transition dipole moment, and $\boldsymbol{E}(\boldsymbol{r},\omega_0)$ is the reflected wave at the emitter's location. The total decay rate is due to the sum of radiative and non radiative decay rate. By multipole expansion of Equation 5.7, we can separate the two contributions.

Studies suggest that ideally both excitation and emission rates are enhanced when the LSPR peak lies in the middle of absorption and PL emission maxima of the fluorophore. However, as can be seen, our CQWs do not have a strong Stoke's shift. One key point to remember is that we excite our samples with a 375

nm pulsed laser. At this wavelength our plasmonic structures are off-resonance and do not appear to interact much with the incident light. Therefore, we can safely rule out the direct excitation of the LSPR via irradiance from the incident laser light source. As a consequence, there is no contribution to PL modification via direct excitation.

Our CQWs show strong absorption at the excitation wavelength. In our system the LSPR is excited entirely through the emission from CQWs. We know from our TRF results that there is a modification of the decay kinetics of our CQWs. We plot the absorption and PL spectra of the CQWs together with the LSPR response of our plasmonic structures to explain the quenching and enhancement we observe in our system.

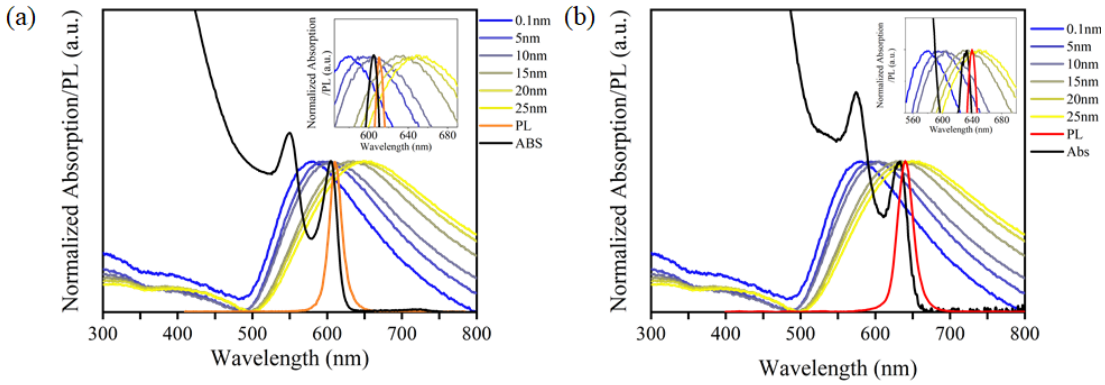

Figure 5.13: Overlap of the absorption and PL spectra of NPLs with the absorption spectra of Au nano-islands with Al_2O_3 spacer thicknesses between 0.1 and 25 nm: (a) CdSe/ZnS NPLs with an emission peak at 610 nm and (b) CdSe/CdZnS NPLs with an emission peak at 650 nm. Insets show the zoomed-in portion of the graph where the peaks overlap.

CdSe/ZnS CQWs exhibit peak emission at $\sim$ 610 nm and CdSe/CdZnS, at $\sim$ 650 nm. Hence, there is no resonant coupling present in the system. Figure 5.13a shows that CdSe/ZnS CQWs' emission peak is redshifted compared to the LSPR maxima of 0.1, 5, and 10 nm spacer thicknesses. This condition is conducive for coupling to the scattered light from Au NPs. We expected fluorescence enhancement; however, we observed quenching. The possible reason could be that the spacer thicknesses are thin and in this regime, of close proximity,

the enhancement of nonradiative recombination prevails over the enhancement of radiative recombination. This is the reason that we see the fastest decay rates for these spacer thicknesses. For the other spacer thicknesses, CQWs' PL maximum is blue-shifted compared to LSPR maxima where the Au NPs are absorbing more than scattering. This could be the reason that despite being farther away from the Au NPs where we expect the enhancement of the nonradiative processes to be weaker in magnitude and result in fluorescence enhancement, we see even more quenched fluorescence. We also then used CdSe/CdZnS NPLs with a PL maximum at 650 nm, which is redshifted compared to all the samples' LSPR wavelength peaks (Figure 5.13b). Similarly, we observe quenching in all these samples.

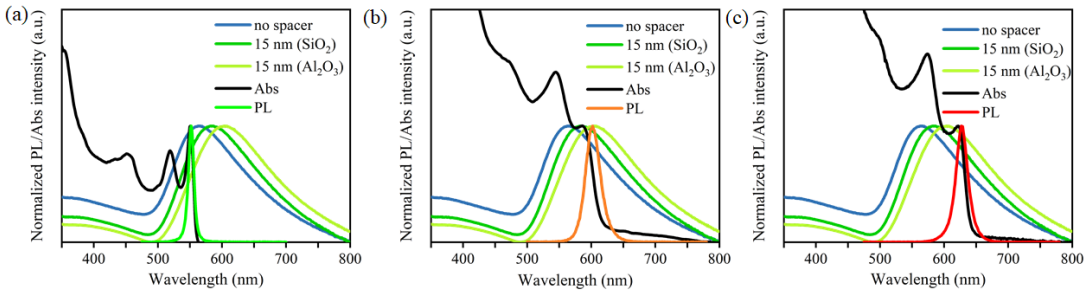

Figure 5.14: Overlap of the absorption and PL spectra of NPLs with the absorption spectra of Au nano-islands with Al_2O_3 spacer and SiO_2 with thickness of 15 nm: (a) 5 ML CdSe core NPLs with an emission peak at 555 nm, (b) CdSe/CdS 4 ML / 1 ML shell NPLs with peak emission at 602 nm, and (c) CdSe/CdS 4 ML / 2 ML shell NPLs with an emission peak at 628 nm.

In another set to study the NPL maxima location compared to the LSPR resonances, we used three different NPLs with peak emissions at $\sim$ 555 nm, $\sim$ 602 nm, and $\sim$ 628 nm, respectively. We fixed the spacer thickness at 15 nm. Figure 5.14 shows that PL maximum was blue-shifted, kept on resonance, and redshifted compared to the LSPR peak with this configuration. Similarly, we observed quenching. Quenching in Figure 5.14a could be explained because there is a minimal overlap between the absorption spectra of NPLs with that of LSPR wavelength. However, in the other two cases, there should have been an enhancement. We replaced the dielectric material and experimented with SiO_2 spacer, and we indeed observed enhancement.

One drawback of making metal nano-islands is the lack of control over the size, shape, and density of the fabricated particles. This gives rise to variation in the plasmonic field over the large-scale area. This variation makes it challenging to obtain reproducible fluorescence enhancements. We can benefit from recent advancements in fabrication tools to create metallic structures with control over their features. Electron beam lithography (EBL), which deploys a focused electron beam to transfer the pattern on the substrate, allows for the fabrication of metallic arrays with full control over the shape, size, and inter-particle distance of the patterned nanostructures [90].

In this thesis, we also fabricate Ag nanoprism patterned structures for studying the modification of emission kinetics of CdSe/CdZnS NPLs with a peak emission at 633 nm. Here FDTD simulations were carried out to choose the best plasmonic structure for our system. The metal selected was silver (Ag) because of its superior LSPR performance. We used triangular morphology [63, 160]. We performed simulations with lattice geometries ranging from square to triangular and hexagonal lattice structures with different edge lengths and inter-particle separation with TE and TM polarized illumination. In the end, we adopted a hexagonal lattice structure because this shows maximum electric field enhancement. After considering the practical limitations, we used a height of 40 nm for our Ag nanoprisms and an edge length of 200 nm with a particle separation of 100 nm (Figure 5.15). The simulations suggested more electric field enhancement for lesser inter-particle separation. However, it was difficult to fabricate nanostructures with spacing shorter than 100 nm.

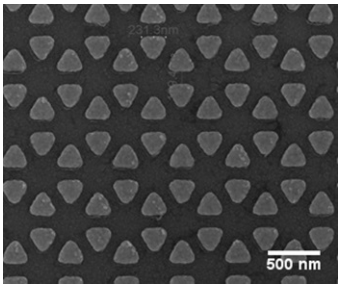

Figure 5.15: SEM image of our Ag nanoprism array with hexagonal unit cell.

The details of the fabrication stages involved in producing NPLs/Ag/substrate

structure are shown in Figure 5.16. A thick layer of polymethylmethacrylate (PMMA-A2), a positive resist, was spin-coated on the clean substrate. Subsequently, baking was carried out at 180 °C for 300 s drying the PMMA resist. This was followed by spin-coating 20 nm of Espacer chemical on the top of the resist. Espacer is a conductive polymer that prevents the charging of the sample during the EBL process.

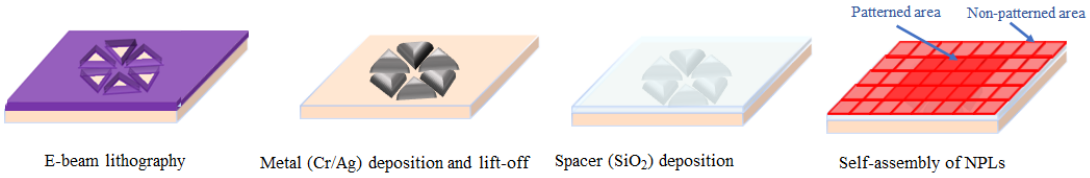

Figure 5.16: Steps involved in forming NPL/Au hybrid structure using EBL technique.

Subsequently the samples were put in the EBL instrument and the patterns were written using an optimized recipe. The exposed samples were developed by dipping in methyl isobutyl ketone: isopropyl alcohol (MIBK: IPA) with a 1:2 ratio for 45 s, followed by immersing in fresh IPA for 15 s, and lastly, samples were submerged in DI water for 30 s. After development, the adhesive layer of 5 nm of chromium (Cr) was deposited, followed by 40 nm of Ag using thermal evaporation. SiO_2 dielectric spacer was deposited using RF sputtering to create a controlled separation between the NPLs and metal nanostructures. Finally, we deposited NPLs using the self-assembly technique in face-down orientation.

The μ-PL measurements were carried out using a confocal microscope. The excitation source was a 405 nm laser. Figure 5.17a shows the fluorescence image of the sample. It can be seen from the image that PL was enhanced in the area where Ag arrays are present as compared to the area where there are no plasmonic nanostructures exhibiting metal enhanced fluorescence. This shows the plasmon-NPL coupling. Figure 5.17b displays the PL intensity obtained for different spacer thicknesses. The experimental data exhibits the maximum PL intensity at a spacing of 10 nm with an enhancement factor of 60. These emission spectra do not show any shift in the emission due to plasmon-NPL coupling. Further systematic studies are required to understand the observed

enhancement.

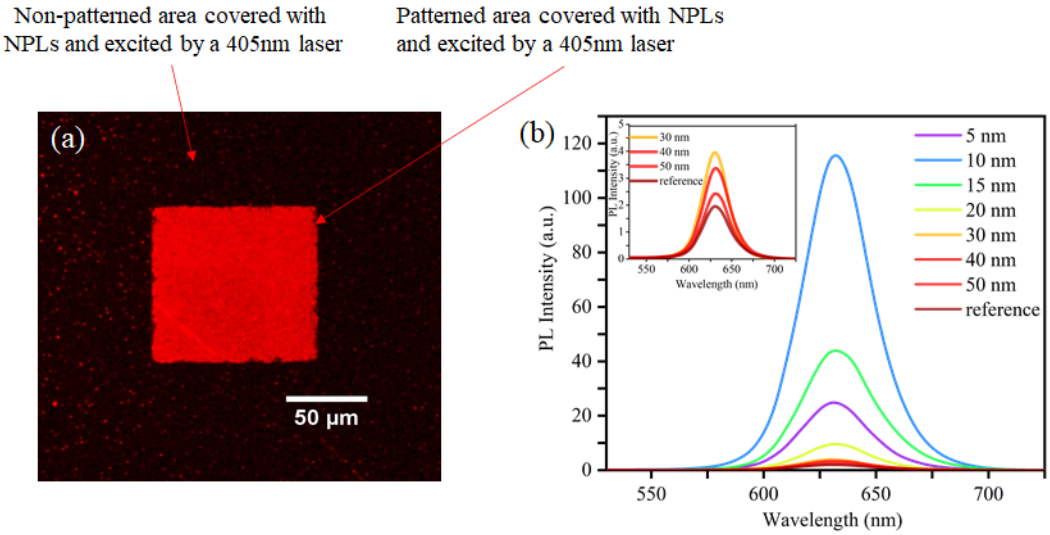

Figure 5.17: (a) Confocal microscope image showing the fluorescence intensity of the NPL film deposited on the quartz substrate with Ag nanoprism array present. The patterned area covered 100 × 100 μm^2. (b) PL spectra of solid films of the NPLs-Ag assembly with varying thicknesses of the SiO_2 separation layer. Inset zooms-in to PL intensity of the reference sample.

5.2 Numerical Results

Finite-difference time-domain (FDTD) simulations were carried out to calculate absorption spectra of our nano-island nanostructures. Nano-island structure was modeled by importing the SEM image (Figure 5.5a). We extended the structure vertically in the z-direction (Figure 5.18). This is an approximation because we know that thermally dewetted Au nano-islands are hemispherical (Figure 5.5b) and do not have sharp corners.

To determine the height of these structures, we swept the height from 20 to 80 nm. The simulated results best matched the experimental results when height was approximately 62 nm (Figure 5.19a). Once height was determined, we added an alumina spacer on top and numerically obtained LSPR spectra of our simulated Au nano-islands (Figure 5.19b). Optical properties of the materials involved here

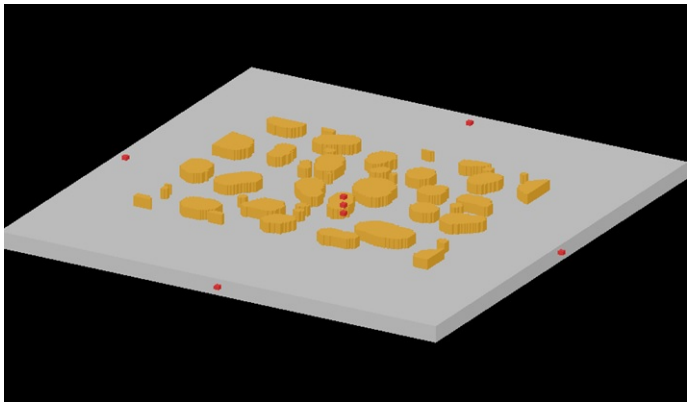

Figure 5.18: Perspective view of the Au nano-island/quartz structure.

were obtained using an ellipsometer. Table 5.3 shows the comparison of LSPR wavelength between the simulated and measured results.

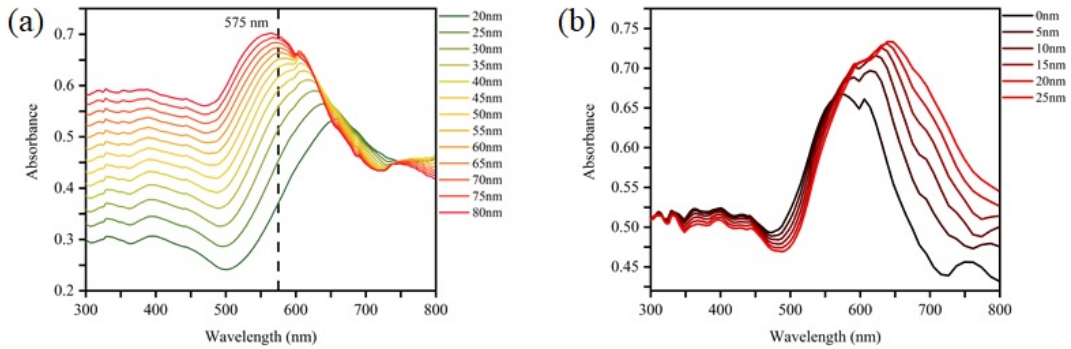

Figure 5.19: (a) Simulated absorption spectra of Au nano-island structure as a function of the height varied from 20 to 80 nm. (b) Simulated absorption spectra of Al_2O_3/ Au/quartz structure with varying thicknesses of the dielectric spacer.

We carried out FDTD simulations to check the magnitude of electric field intensities produced in the vicinity of the Au nanostructures. We placed planar 2D monitors parallel to the substrate surface at the heights where NPLs would be deposited to record the electric field intensities these NPL emitters would experience. Figure 5.20 displays electric field distributions at our excitation wavelength, NPL emission peaks as well as LSPR peak. There is no surprise that the maximum field intensity is closest to the particles and its strength decreases as the monitor is placed further away. Another aspect we notice is that, near the structures, the electric field is confined around the hot spots and is zero elsewhere.

Table 5.3: Comparison of the LSPR wavelength: Simulation vs. measurement (all values are in nm)

Al_2O_3 thickness (nm)	LSPR maxima (simulation)	LSPR maxima (measurement)
0	576.5	-
0.1	-	579.0
5	614.0	597.0
10	622.1	604.8
15	630.2	635.2
20	638.7	644.1
25	643.5	651.8

As we move away from the nanostructures, the electric field distribution is more delocalized in space.

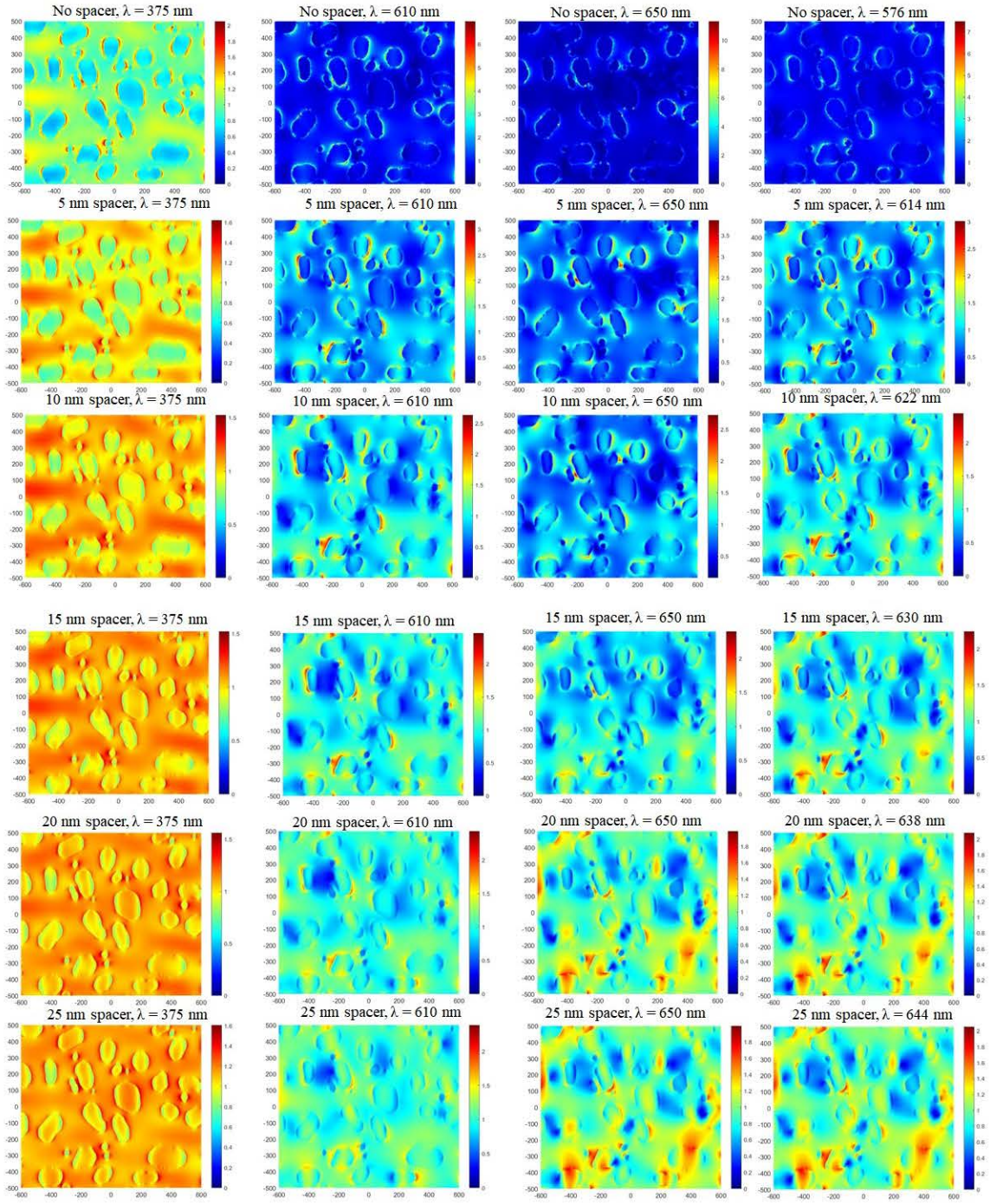

Figure 5.20: Electric field maps extracted from the field monitors placed at separation ranging from 0 to 25 nm away from the top surface of Au nano-structures. Electric field intensity distributions are shown for a variety of laser excitation wavelength, PL emission peaks of NPLs and LSPR resonance wavelengths. Here x- and y-spans are in nm.

In addition, FEM based simulations were performed to obtain the optical cross-section of our proposed nanoprism system. Figure 5.21a shows the simulation model setup. The simulated extinction spectrum is displayed in Figure 5.21b, which shows the overlap of LSPR with the PL emission peak of our NPLs. In simulation modeling, edges were rounded to best model the fabricated samples.

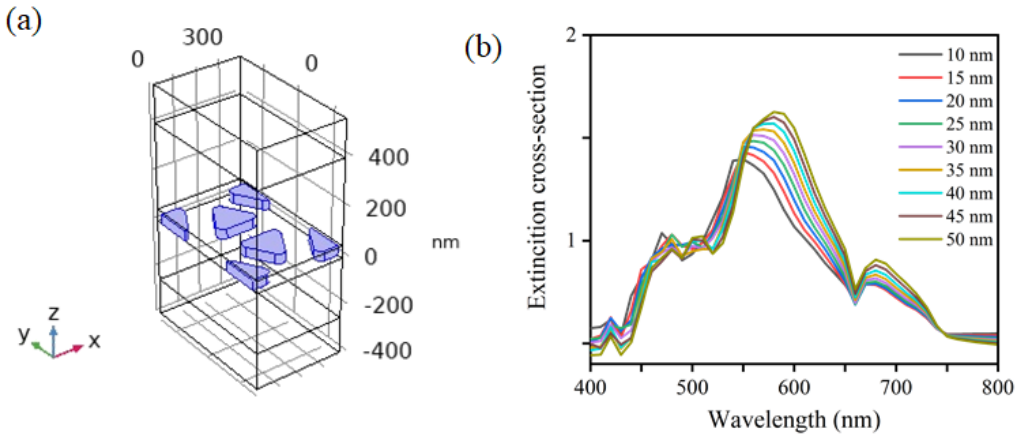

Figure 5.21: (a) Schematic illustration of the simulation setup used for finding the optical cross-sections of Ag nanoprism arrays. (b) Extinction cross-section of the Ag/substrate system with SiO_2 dielectric spacer on top.

5.3 Summary

In summary, here we experimentally demonstrated the modification of emission kinetics of CQWs using plasmonic nanostructures. We fabricated random gold nano-islands and ordered silver nanopatterns on quartz substrates to produce plasmonically coupled emission of CQWs by exploiting the LSPR of these metal nanostructures. We obtained distance-dependent modification of the lifetimes of these CQWs when coupled them with random gold nano-islands and we mainly observed quenching. Only by changing the dielectric spacer and carefully tuning the CQW emission peak, we recorded a 3-fold PL enhancement at a spacer thickness of 15 nm. The finite difference time domain method was used to calculate absorption spectra and electric field intensity distribution of the modeled gold nano-islands. In addition, we also fabricated arrays of silver nanoprisms to enhance

the CQW fluorescence in hexagonal lattice pattern. We used the self-assembly method to deposit our CQWs in face-down orientation onto the nanopatterned substrates. Silica spacer was used to adjust the fluorophore-plasmonic nanostructure separation. We observed a 60-fold increase in PL intensity when we used this CQW-silver nanoprism array configuration.

Chapter 6

Conclusion

In this thesis, we proposed and demonstrated the well-controlled modification of the emission kinetics of the CQWs. It is well-documented that energy transfer mechanisms affect the lifetimes of the excited fluorophores. Different interactions define how energy transfer occurs, depending on the distance between the donor and the acceptor in a hybrid system. Our objective was to use the Förster resonance energy transfer (FRET), a nonradiative energy transfer (NRET) process that prevails when the donor and acceptor are close to each other, within tens of nanometers, because of its high efficiency in transferring excitation energy.

In part of this thesis work, we use bulk silicon as the acceptor, along with CQWs acting as the donors. The hybrid system selected here was interesting on several accounts. It served the main objective of studying the modification of fluorescence emission of the CQWs. Another aspect was that the hybrid structure consisted of 2D donor-3D acceptor geometry, which had not been analyzed before. Besides, knowing that silicon, an indirect band-gap material, was a poor absorber of light, this hybrid structure could be used for photosensitization of silicon. Previously, photosensitization of silicon had been shown with other colloidal nanocrystals (NCs) classes but not with quasi-2D CQWs.

We used the self-assembly method to deposit the CQWs on the substrates.

This technique allowed us to cover the entire substrate with the CQWs without any voids, thus forming a 2D thin film of these 2D CQWs. Also, the method gave us control over the orientation of the deposited thin films. We used the face-down configuration. Since FRET takes place through dipole-dipole interaction, the self-assembly method allowed us to take advantage of the anisotropy of the CQWs and utilize the strong in-plane exciton dipole moment for this interaction. We varied the separation between CQWs and the substrate using the dielectric spacer. We found that the FRET exhibits a distance scaling of d^{-1} in our system. This is the first account of distance scaling having an inverse relationship. This finding is in line with the view that as the dimension of the acceptor layer increases, the FRET rate becomes increasingly less sensitive to the distance. We also demonstrated that photosensitization of the silicon using CQWs enhances the photocurrent in the silicon layer. This is the first account of the CQWs' sensitization of the silicon layer.

Another approach adopted to modify the emission kinetics of the CQWs was to use lossy noble metal nanostructures. We used the random gold nano-islands and the patterned periodic silver nanoprisms to alter the emission kinetics using the enhanced near-field electric field localization of these nanostructures. We observed the distance-dependent modification in the lifetimes of the CQWs in the presence of the gold nano-islands. Quenching of the photoluminescence (PL) suggests the dominance of NRET in the system. By carefully tuning the resonances and spacer thickness, we did observe an enhancement of approximately three-folds. Using the silver patterned arrays, we observed a sixty-fold enhancement in the PL intensity. Patterned metal nanostructures provide the control that random nano-islands lack.

CQWs have shown excellent optoelectronic properties that are ideally suited for light-harvesting applications. There is a need to harness those properties to fill the void in optoelectronic applications. In our proof-of-concept demonstration, a single monolayer of CQWs was used. It would be exciting to optimize the CQWs sensitized silicon photoconductor device. Also, much research has focused on the interaction between quantum dots and surface plasmons in weak and strong coupling regimes. There is a lack of research on the CQWs coupling with surface

plasmons, particularly in the weak regime.

Bibliography

[1] A. Szemjonov, M. Tasso, S. Ithurria, I. Ciofini, F. Labat, and T. Pauporté, "Ligand exchange on CdSe nanoplatelets for the solar light sensitization of TiO_2 and Zn0 nanorod arrays," *Journal of Photochemistry and Photobiology A: Chemistry*, vol. 368, pp. 182–189, 2019.

[2] F. Fan, P. Kanjanaboos, M. Saravanapavanantham, E. Beauregard, G. Ingram, E. Yassitepe, M. M. Adachi, O. Voznyy, A. K. Johnston, G. Walters, G.-H. Kim, Z.-H. Lu, and E. H. Sargent, "Colloidal $CdSe_{1-x}S_x$ Nanoplatelets with Narrow and Continuously-Tunable Electroluminescence," *Nano Letters*, vol. 15, no. 7, pp. 4611–4615, 2015.

[3] J. Maskoun, N. Gheshlaghi, F. Isik, S. Delikanli, O. Erdem, E. Y. Erdem, and H. V. Demir, "Optical Microfluidic Waveguides and Solution Lasers of Colloidal Semiconductor Quantum Wells," *Advanced Materials*, vol. 33, no. 10, p. 2007131, 2021.

[4] S. Foroutan-Barenji, O. Erdem, S. Delikanli, H. B. Yagci, N. Gheshlaghi, Y. Altintas, and H. V. Demir, "Single-Mode Lasing from a Single 7 nm Thick Monolayer of Colloidal Quantum Wells in a Monolithic Microcavity," *Laser and Photonics Reviews*, vol. 15, no. 4, p. 2000479, 2021.

[5] N. Gheshlaghi, S. Foroutan-Barenji, O. Erdem, Y. Altintas, F. Shabani, M. H. Humayun, and H. V. Demir, "Self-Resonant Microlasers of Colloidal Quantum Wells Constructed by Direct Deep Patterning," *Nano Letters*, vol. 21, no. 11, pp. 4598–4605, 2021.

[6] J. Yu, M. Sharma, M. Li, S. Delikanli, A. Sharma, M. Taimoor, Y. Altintas, J. R. McBride, T. Kusserow, T.-C. Sum, H. V. Demir, and C. Dang, "Low-Threshold Lasing from Copper-Doped CdSe Colloidal Quantum Wells," *Laser and Photonics Reviews*, vol. 15, no. 6, p. 2100034, 2021.

[7] M. Pelton, "Carrier Dynamics, Optical Gain, and Lasing with Colloidal Quantum Wells," *Journal of Physical Chemistry C*, vol. 122, no. 20, pp. 10659–10674, 2018.

[8] F. Zhang, S. Wang, L. Wang, Q. Lin, H. Shen, W. Cao, C. Yang, H. Wang, L. Yu, Z. Du, J. Xue, and L. S. Li, "Super color purity green quantum dot light-emitting diodes fabricated by using CdSe/CdS nanoplatelets," *Nanoscale*, vol. 8, no. 24, pp. 12182–12188, 2016.

[9] B. Liu, Y. Altintas, L. Wang, S. Shendre, M. Sharma, H. Sun, E. Mutlugun, and H. V. Demir, "Record High External Quantum Efficiency of 19.2 % Achieved in Light-Emitting Diodes of Colloidal Quantum Wells Enabled by Hot-Injection Shell Growth," *Advanced Materials*, vol. 32, no. 8, p. 1905824, 2020.

[10] J. C. Van Der Bok, D. M. Dekker, M. L. Peerlings, B. B. Salzmann, and A. Meijerink, "Luminescence Line Broadening of CdSe Nanoplatelets and Quantum Dots for Application in w-LEDs," *Journal of Physical Chemistry C*, vol. 124, no. 22, pp. 12153–12160, 2020.

[11] R. Liang, M. Wei, D. G. Evans, and X. Duan, "Inorganic nanomaterials for bioimaging, targeted drug delivery and therapeutics," *Chemical Communications*, vol. 50, no. 91, pp. 14071–14081, 2014.

[12] F. P. García de Arquer, D. V. Talapin, V. I. Klimov, Y. Arakawa, M. Bayer, and E. H. Sargent, "Semiconductor quantum dots: Technological progress and future challenges," *Science*, vol. 373, no. 6555, p. eaaz8541, 2021.

[13] H. M. Gil, T. W. Price, K. Chelani, J.-S. G. Bouillard, S. D. Calaminus, and G. J. Stasiuk, "NIR-quantum dots in biomedical imaging and their future," *iScience*, vol. 24, no. 3, p. 102189, 2021.

[14] A. Kumari, A. Sharma, R. Sharma, U. Malairaman, and R. R. Singh, "Biocompatible and fluorescent water based NIR emitting CdTe quantum dot probes for biomedical applications," *Spectrochimica Acta - Part A: Molecular and Biomolecular Spectroscopy*, vol. 248, p. 119206, 2021.

[15] L. E. Brus, "Electron-electron and electron-hole interactions in small semiconductor crystallites: The size dependence of the lowest excited electronic state," *The Journal of Chemical Physics*, vol. 80, no. 9, pp. 4403–4409, 1984.

[16] A. I. Ekimov, A. L. Efros, and A. A. Onushchenko, "Quantum size effect in semiconductor microcrystals," *Solid State Communications*, vol. 56, no. 11, pp. 921–924, 1985.

[17] C. B. Murray, D. J. Norris, and M. G. Bawendi, "Synthesis and Characterization of Nearly Monodisperse CdE (E = S, Se, Te) Semiconductor Nanocrystallites," *Journal of the American Chemical Society*, vol. 115, no. 19, pp. 8706–8715, 1993.

[18] X. Peng, L. Manna, W. Yang, J. Wickham, E. Scher, A. Kadavanich, and A. P. Alivisatos, "Shape Control of CdSe Nanocrystals," *Nature*, vol. 404, pp. 59–61, 2000.

[19] S. Ithurria and B. Dubertret, "Quasi 2D colloidal CdSe platelets with thicknesses controlled at the atomic level," *Journal of the American Chemical Society*, vol. 130, no. 49, pp. 16504–16505, 2008.

[20] J. Mal, Y. V. Nancharaiah, E. D. Van Hullebusch, and P. N. Lens, "Metal chalcogenide quantum dots: Biotechnological synthesis and applications," *RSC Advances*, vol. 6, no. 47, pp. 41477–41495, 2016.

[21] D. Kim, Y. K. Lee, D. Lee, W. D. Kim, W. K. Bae, and D. C. Lee, "Colloidal Dual-Diameter and Core-Position-Controlled Core/Shell Cadmium Chalcogenide Nanorods," *ACS Nano*, vol. 11, no. 12, pp. 12461–12472, 2017.

[22] Y. Min, E. Im, G.-T. Hwang, J.-W. Kim, C.-W. Ahn, J.-J. Choi, B.-D. Hahn, J.-H. Choi, W.-H. Yoon, D.-S. Park, D. C. Hyun, and G. D. Moon, "Heterostructures in two-dimensional colloidal metal chalcogenides: Synthetic fundamentals and applications," *Nano Research*, vol. 12, no. 8, pp. 1750–1769, 2019.

[23] T. K. Kormilina, S. A. Cherevkov, A. V. Fedorov, and A. V. Baranov, "Cadmium Chalcogenide Nano-Heteroplatelets: Creating Advanced Nanostructured Materials by Shell Growth, Substitution, and Attachment," *Small*, vol. 13, no. 41, p. 1702300, 2017.

[24] M. D. Tessier, P. Spinicelli, D. Dupont, G. Patriarche, S. Ithurria, and B. Dubertret, "Efficient exciton concentrators built from colloidal core/crown CdSe/CdS semiconductor nanoplatelets," *Nano Letters*, vol. 14, no. 1, pp. 207–213, 2014.

[25] B. Ji, E. Rabani, A. L. Efros, R. Vaxenburg, O. Ashkenazi, D. Azulay, U. Banin, and O. Millo, "Dielectric Confinement and Excitonic Effects in Two-Dimensional Nanoplatelets," *ACS Nano*, vol. 14, no. 7, pp. 8257–8265, 2020.

[26] M. D. Tessier, C. Javaux, I. Maksimovic, V. Loriette, and B. Dubertret, "Spectroscopy of single CdSe nanoplatelets," *ACS Nano*, vol. 6, no. 8, pp. 6751–6758, 2012.

[27] M. D. Tessier, B. Mahler, B. Nadal, H. Heuclin, S. Pedetti, and B. Dubertret, "Spectroscopy of colloidal semiconductor core/shell nanoplatelets with high quantum yield," *Nano Letters*, vol. 13, no. 7, pp. 3321–3328, 2013.

[28] Y. Altintas, U. Quliyeva, K. Gungor, O. Erdem, Y. Kelestemur, E. Mutlugun, M. V. Kovalenko, and H. V. Demir, "Highly Stable, Near-Unity Efficiency Atomically Flat Semiconductor Nanocrystals of CdSe/ZnS Hetero-Nanoplatelets Enabled by ZnS-Shell Hot-Injection Growth," *Small*, vol. 15, no. 8, p. 1804854, 2019.

[29] A. Yeltik, S. Delikanli, M. Olutas, Y. Kelestemur, B. Guzelturk, and H. V. Demir, "Experimental Determination of the Absorption Cross-Section and Molar Extinction Coefficient of Colloidal CdSe Nanoplatelets," *Journal of Physical Chemistry C*, vol. 119, no. 47, pp. 26768–26775, 2015.

[30] S. Ithurria, M. D. Tessier, B. Mahler, R. P. S. M. Lobo, B. Dubertret, and A. L. Efros, "Colloidal nanoplatelets with two-dimensional electronic structure," *Nat. Mater*, vol. 10, pp. 936–941, 2011.

[31] Q. Li, Q. Liu, R. D. Schaller, and T. Lian, "Reducing the Optical Gain Threshold in Two-Dimensional CdSe Nanoplatelets by the Giant Oscillator Strength Transition Effect," *Journal of Physical Chemistry Letters*, vol. 10, no. 7, pp. 1624–1632, 2019.

[32] E. Baghani, S. K. Oleary, I. Fedin, D. V. Talapin, and M. Pelton, "Auger-limited carrier recombination and relaxation in CdSe colloidal quantum wells," *Journal of Physical Chemistry Letters*, vol. 6, no. 6, pp. 1032–1036, 2015.

[33] B. Guzelturk, Y. Kelestemur, M. Olutas, S. Delikanli, and H. V. Demir, "Amplified Spontaneous Emission and Lasing in Colloidal Nanoplatelets," *ACS Nano*, vol. 8, no. 7, pp. 6599–6605, 2014.

[34] J. Yu and R. Chen, "Optical properties and applications of two-dimensional CdSe nanoplatelets," *InfoMat*, vol. 2, no. 5, pp. 905–927, 2020.

[35] M. Sharma, S. Delikanli, and H. V. Demir, "Two-Dimensional CdSe-Based Nanoplatelets: Their Heterostructures, Doping, Photophysical Properties, and Applications," *Proceedings of the IEEE*, vol. 108, no. 5, pp. 655–675, 2020.

[36] S. Lu, Z. Lingley, T. Asano, D. Harris, T. Barwicz, S. Guha, and A. Madhukar, "Photocurrent induced by nonradiative energy transfer from nanocrystal quantum dots to adjacent silicon nanowire conducting channels: Toward a new solar cell paradigm," *Nano Letters*, vol. 9, no. 12, pp. 4548–4552, 2009.

[37] S. Chanyawadee, R. T. Harley, M. Henini, D. V. Talapin, and P. G. Lagoudakis, "Photocurrent enhancement in hybrid nanocrystal quantum-dot p-i-n photovoltaic devices," *Physical Review Letters*, vol. 102, no. 7, p. 077402, 2009.

[38] M. T. Nimmo, L. M. Caillard, W. De Benedetti, H. M. Nguyen, O. Seitz, Y. N. Gartstein, Y. J. Chabal, and A. V. Malko, "Visible to near-infrared sensitization of silicon substrates via energy transfer from proximal nanocrystals: Further insights for hybrid photovoltaics," *ACS Nano*, vol. 7, no. 4, pp. 3236–3245, 2013.

[39] A. Yeltik, B. Guzelturk, P. L. Hernandez-Martinez, A. O. Govorov, and H. V. Demir, "Phonon-Assisted Exciton Transfer into Silicon using Nanoemitters: The Role of Phonons and Temperature Effects in Förster Resonance Energy Transfer," *ACS Nano*, vol. 7, no. 12, pp. 10492–10501, 2013.

[40] H. M. Nguyen, O. Seitz, W. Peng, Y. N. Gartstein, Y. J. Chabal, and A. V. Malko, "Efficient radiative and nonradiative energy transfer from proximal CdSe/ZnS nanocrystals into silicon nanomembranes," *ACS Nano*, vol. 6, no. 6, pp. 5574–5582, 2012.

[41] T. Förster, "Energiewanderung und fluoreszenz," *Naturwissenschaften*, vol. 33, pp. 166–175, 1946.

[42] B. Guzelturk and H. V. Demir, "Near-Field Energy Transfer Using Nanoemitters For Optoelectronics," *Advanced Functional Materials*, vol. 26, no. 45, pp. 8158–8177, 2016.

[43] D. L. Dexter, "A theory of sensitized luminescence in solids," *The Journal of Chemical Physics*, vol. 21, no. 5, pp. 836–850, 1953.

[44] H. M. Nguyen, O. Seitz, Y. N. Gartstein, Y. J. Chabal, and A. V. Malko, "Energy transfer from colloidal nanocrystals into Si substrates studied via photoluminescence photon counts and decay kinetics," *Journal of the Optical Society of America B*, vol. 30, no. 9, pp. 2401–2408, 2013.

[45] D. L. Dexter, "Two ideas on energy transfer phenomena: Ion-pair effects involving the OH stretching mode, and sensitization of photovoltaic cells," *Journal of Luminescence*, vol. 18, pp. 779–784, 1979.

[46] R. R. Chance, A. Prock, and R. Silbey, "Molecular fluorescence and energy transfer near interfaces," in *Advances in Chemical Physics* (S. A. Rice and I. Prigogine, eds.), vol. 37, pp. 1–65, Wiley, 1978.

[47] A. P. Alivisatos, M. F. Arndt, S. Efrima, D. H. Waldeck, and C. B. Harris, "Electronic energy transfer at semiconductor interfaces. I. Energy transfer from two-dimensional molecular films to Si(111)," *The Journal of Chemical Physics*, vol. 86, no. 11, pp. 6540–6549, 1987.

[48] L. Novotny and B. Hecht, *Principles of Nano-Optics*. Cambridge University, 2006.

[49] J. R. Lakowicz, *Principles of fluorescence spectroscopy*. Springer, 2006.

[50] K. M. Mayer and J. H. Hafner, "Localized surface plasmon resonance sensors," *Chemical Reviews*, vol. 111, no. 6, pp. 3828–3857, 2011.

[51] T. Liebermann and W. Knoll, "Surface-plasmon field-enhanced fluorescence spectroscopy," *Colloids and Surfaces A: Physicochemical and Engineering Aspects*, vol. 171, no. 1-3, pp. 115–130, 2000.

[52] I. A. Milekhin, K. V. Anikin, M. Rahaman, E. E. Rodyakina, T. A. Duda, B. M. Saidzhonov, R. B. Vasiliev, V. M. Dzhagan, A. G. Milekhin, S. A. Batsanov, A. K. Gutakovskii, A. V. Latyshev, and D. R. Zahn, "Resonant plasmon enhancement of light emission from CdSe/CdS nanoplatelets on Au nanodisk arrays," *Journal of Chemical Physics*, vol. 153, no. 16, p. 164708, 2020.

[53] K. H. Drexhage, "Influence of a dielectric interface on fluorescence decay time," *Journal of Luminescence*, vol. 1-2, pp. 693–701, 1970.

[54] J. R. Lakowicz, "Radiative decay engineering 5: Metal-enhanced fluorescence and plasmon emission," *Analytical Biochemistry*, vol. 337, no. 2, pp. 171–194, 2005.

[55] A. I. Dragan, E. S. Bishop, J. R. Casas-Finet, R. J. Strouse, J. McGivney, M. A. Schenerman, and C. D. Geddes, "Distance Dependence of Metal-Enhanced Fluorescence," *Plasmonics*, vol. 7, no. 4, pp. 739–744, 2012.

[56] N. S. Abadeer, M. R. Brennan, W. L. Wilson, and C. J. Murphy, "Distance and plasmon wavelength dependent fluorescence of molecules bound to silica-coated gold nanorods," *ACS Nano*, vol. 8, no. 8, pp. 8392–8406, 2014.

[57] H. Qin, D. Ma, and J. Du, "Distance dependent fluorescence quenching and enhancement of gold nanoclusters by gold nanoparticles," *Spectrochimica Acta - Part A: Molecular and Biomolecular Spectroscopy*, vol. 189, pp. 161–166, 2018.

[58] A. Raja, A. Montoya-Castillo, J. Zultak, X. X. Zhang, Z. Ye, C. Roquelet, D. A. Chenet, A. M. Van Der Zande, P. Huang, S. Jockusch, J. Hone, D. R. Reichman, L. E. Brus, and T. F. Heinz, "Energy Transfer from Quantum Dots to Graphene and MoS_2: The Role of Absorption and Screening in Two-Dimensional Materials," *Nano Letters*, vol. 16, no. 4, pp. 2328–2333, 2016.

[59] L. Kubie and B. A. Parkinson, "Photosensitization of Single-Crystal Oxide Substrates with Quantum Confined Semiconductors," *Langmuir*, vol. 35, no. 18, pp. 5997–6004, 2019.

[60] A. Yeltik, M. Olutas, M. Sharma, K. Gungor, and H. V. Demir, "Nonradiative Energy Transfer between Doped and Undoped Flat Semiconductor Nanocrystals of Colloidal Quasi-2D Nanoplatelets," *The Journal of Physical Chemistry C*, vol. 123, no. 2, pp. 1470–1476, 2019.

[61] N. Taghipour, P. L. H. Martinez, A. Ozden, M. Olutas, D. Dede, K. Gungor, O. Erdem, N. K. Perkgoz, and H. V. Demir, "Near-Unity Efficiency Energy Transfer from Colloidal Semiconductor Quantum Wells of CdSe/CdS Nanoplatelets to a Monolayer of MoS_2," *ACS Nano*, vol. 12, no. 8, pp. 8547–8554, 2018.

[62] O. Erdem, K. Gungor, B. Guzelturk, I. Tanriover, M. Sak, M. Olutas, D. Dede, Y. Kelestemur, and H. V. Demir, "Orientation-Controlled Nonradiative Energy Transfer to Colloidal Nanoplatelets: Engineering Dipole Orientation Factor," *Nano Letters*, vol. 19, no. 7, pp. 4297–4305, 2019.

[63] P. P. Pompa, L. Martiradonna, A. Della Torre, F. Della Sala, L. Manna, M. de Vittorio, F. Calabi, R. Cinagolani, and R. Rinaldi, "Metal-enhanced fluorescence of colloidal nanocrystals with nanoscale control," *Nature Nanotechnology*, vol. 1, no. 2, pp. 126–130, 2006.

[64] K. Okamoto, S. Vyawahare, and A. Scherer, "Surface-plasmon enhanced bright emission from CdSe quantum-dot nanocrystals," *Journal of the Optical Society of America B*, vol. 23, no. 8, pp. 1674–1678, 2006.

[65] I. M. Soganci, S. Nizamoglu, E. Mutlugun, O. Akin, and H. V. Demir, "Localized plasmon-engineered spontaneous emission of CdSe/ZnS nanocrystals closely-packed in the proximity of Ag nanoisland films for controlling emission linewidth, peak, and intensity," *Optics Express*, vol. 15, no. 22, p. 14289, 2007.

[66] O. Bitton, S. N. Gupta, and G. Haran, "Quantum dot plasmonics: From weak to strong coupling," *Nanophotonics*, vol. 8, no. 4, pp. 559–575, 2019.

[67] L. Trotsiuk, A. Muravitskaya, O. Kulakovich, D. Guzatov, A. Ramanenka, Y. Kelestemur, H. V. Demir, and S. Gaponenko, "Plasmon-enhanced fluorescence in gold nanorod-quantum dot coupled systems," *Nanotechnology*, vol. 31, no. 10, p. 105201, 2020.

[68] H. Bronstein, C. B. Nielsen, B. C. Schroeder, and I. McCulloch, "The role of chemical design in the performance of organic semiconductors," *Nature Reviews Chemistry*, vol. 4, no. 2, pp. 66–77, 2020.

[69] A. Eatemadi, H. Daraee, H. Karimkhanloo, M. Kouhi, N. Zarghami, A. Akbarzadeh, M. Abasi, Y. Hanifehpour, and S. W. Joo, "Carbon nanotubes: properties, synthesis, purification, and medical applications," *Nanoscale Research Letters*, vol. 9, no. 1, p. 393, 2014.

[70] H. Wu, F. Meng, L. Li, S. Jin, and G. Zheng, "Dislocation-driven CdS and CdSe nanowire growth," *ACS Nano*, vol. 6, no. 5, pp. 4461–4468, 2012.

[71] D. V. Talapin, J.-S. Lee, M. V. Kovalenko, and E. V. Shevchenko, "Prospects of colloidal nanocrystals for electronic and optoelectronic applications," *Chemical Reviews*, vol. 110, no. 1, pp. 389–458, 2010.

[72] B. Güzeltürk, *Excitonics of Colloidal Nanocrystals for Next-Generation Optoelectronics*. Phd thesis, Bilkent University, Turkey, 2016.

[73] D. S. Kumar, B. J. Kumar, and H. Mahesh, "Quantum Nanostructures (QDs): An Overview," in *Synthesis of Inorganic Nanomaterials: Advances and Key Technologies*, ch. 3, pp. 59–88, Woodhead Publishing, 2018.

[74] M. Fox, *Optical Properties of Solids*. New York, NY: Oxford University Press, 2001.

[75] K. Güngör, *Colloidal Photonics of Semiconductor Nanocrystals: From Polarized Color Conversion to Efficient Solar Concentration*. Phd thesis, Bilkent University, Turkey, 2018.

[76] Y. Kelestemur, B. Guzelturk, O. Erdem, M. Olutas, T. Erdem, C. F. Usanmaz, K. Gungor, and H. V. Demir, "CdSe/$CdSe_{1-x}Te_x$ Core/Crown Heteronanoplatelets: Tuning the Excitonic Properties without Changing the Thickness," *Journal of Physical Chemistry C*, vol. 121, no. 8, pp. 4650–4658, 2017.

[77] B. Mahler, B. Nadal, C. Bouet, G. Patriarche, and B. Dubertret, "Core/shell colloidal semiconductor nanoplatelets," *Journal of the American Chemical Society*, vol. 134, no. 45, pp. 18591–18598, 2012.

[78] Y. Kelestemur, B. Guzelturk, O. Erdem, M. Olutas, K. Gungor, and H. V. Demir, "Platelet-in-Box Colloidal Quantum Wells: CdSe/CdS@CdS Core/Crown@Shell Heteronanoplatelets," *Advanced Functional Materials*, vol. 26, no. 21, pp. 3570–3579, 2016.

[79] S. Ithurria and D. V. Talapin, "Colloidal Atomic Layer Deposition (c-ALD) using self-limiting reactions at nanocrystal surface coupled to phase transfer

between polar and nonpolar media," *Journal of the American Chemical Society*, vol. 134, no. 45, pp. 18585–18590, 2012.

[80] O. Erdem, *Colloidal Optoelectronics of Self-Assembled Quantum Well Superstructures*. Phd thesis, Bilkent University, Turkey, 2020.

[81] Y. Gao, M. C. Weidman, and W. A. Tisdale, "CdSe Nanoplatelet Films with Controlled Orientation of their Transition Dipole Moment," *Nano Letters*, vol. 17, no. 6, pp. 3837–3843, 2017.

[82] H. Min, J. Zhou, X. Bai, L. Li, K. Zhang, T. Wang, X. Zhang, Y. Li, Y. Jiao, X. Qi, and Y. Fu, "Approach to Fabricating a Compact Gold Nanoparticle Film with the Assistance of a Surfactant," *Langmuir*, vol. 33, no. 27, pp. 6732–6738, 2017.

[83] M. H. Humayun, P. L. Hernandez-Martinez, N. Gheshlaghi, O. Erdem, Y. Altintas, F. Shabani, and H. V. Demir, "Near-Field Energy Transfer into Silicon Inversely Proportional to Distance Using Quasi-2D Colloidal Quantum Well Donors," *Small*, vol. 2103524, 2021.

[84] T. Förster, "Energy migration and fluorescence," *Journal of Biomedical Optics*, vol. 17, no. 1, p. 011002, 2012.

[85] R. S. Swathi and K. L. Sebastian, "Distance dependence of fluorescence resonance energy transfer," *Journal of Chemical Sciences*, vol. 121, no. 5, pp. 777–787, 2009.

[86] A. L. Rogach, T. A. Klar, J. M. Lupton, A. Meijerink, and J. Feldmann, "Energy transfer with semiconductor nanocrystals," *Journal of Materials Chemistry*, vol. 19, no. 9, pp. 1208–1221, 2009.

[87] P. L. Hernández-Martínez, A. O. Govorov, and H. V. Demir, "Generalized theory of Förster-type nonradiative energy transfer in nanostructures with mixed dimensionality," *Journal of Physical Chemistry C*, vol. 117, no. 19, pp. 10203–10212, 2013.

[88] P. L. Hernández-Martínez, A. O. Govorov, and H. V. Demir, "Förster-Type nonradiative energy transfer for assemblies of arrayed nanostructures: Confinement dimension vs stacking dimension," *Journal of Physical Chemistry C*, vol. 118, no. 9, pp. 4951–4958, 2014.

[89] W. Knoll, "Interfaces and thin films as seen by bound electromagnetic waves," *Annual Review of Physical Chemistry*, vol. 49, no. 1, pp. 569–638, 1998.

[90] E. Hutter and J. H. Fendler, "Exploitation of localized surface plasmon resonance," *Advanced Materials*, vol. 16, no. 19, pp. 1685–1706, 2004.

[91] M. M. Miller and A. A. Lazarides, "Sensitivity of metal nanoparticle plasmon resonance band position to the dielectric environment as observed in scattering," *Journal of Optics A: Pure and Applied Optics*, vol. 8, no. 4, p. S239, 2006.

[92] P. Mulvaney, "Surface plasmon spectroscopy of nanosized metal particles," *Langmuir*, vol. 12, no. 3, pp. 788–800, 1996.

[93] K. L. Kelly, E. Coronado, L. L. Zhao, and G. C. Schatz, "The Optical Properties of Metal Nanoparticles: The Influence of Size, Shape, and Dielectric Environment," *Journal of Physical Chemistry B*, vol. 107, pp. 668–677, 2003.

[94] K. A. Willets and R. P. Van Duyne, "Localized surface plasmon resonance spectroscopy and sensing," *Annual Review of Physical Chemistry*, vol. 58, pp. 267–297, 2007.

[95] A. J. Haes and R. P. Van Duyne, "A unified view of propagating and localized surface plasmon resonance biosensors," *Analytical and Bioanalytical Chemistry*, vol. 379, no. 7, pp. 920–930, 2004.

[96] Y. Li, *Plasmonic Optics: Theory and Applications*. SPIE Press, 2017.

[97] K. Ray, R. Badugu, and J. R. Lakowicz, "Distance-dependent metal-enhanced fluorescence from Langmuir-Blodgett monolayers of Alkyl-NBD

derivatives on silver island films," *Langmuir*, vol. 22, no. 20, pp. 8374–8378, 2006.

[98] S. Pawar, A. Bhattacharya, and A. Nag, "Metal-Enhanced Fluorescence Study in Aqueous Medium by Coupling Gold Nanoparticles and Fluorophores Using a Bilayer Vesicle Platform," *ACS Omega*, vol. 4, no. 3, pp. 5983–5990, 2019.

[99] M. Pelton, "Modified spontaneous emission in nanophotonic structures," *Nature Photonics*, vol. 9, no. 7, pp. 427–435, 2015.

[100] E. M. Purcell, "Spontaneous Emission Probabilities at Radio Frequencies," *Phys. Rev*, vol. 69, p. 674, 1946.

[101] W. L. Barnes, "Fluorescence near interfaces: The role of photonic mode density," *Journal of Modern Optics*, vol. 45, no. 4, pp. 661–699, 1998.

[102] W. C. Chew, *Waves and Fields in Inhomogeneous Media*. Wiley-IEEE Press, 1999.

[103] N. Alderman, L. Danos, L. Fang, M. C. Grossel, and T. Markvart, "Light harvesting in silicon(111) surfaces using covalently attached protoporphyrin IX dyes," *Chemical Communications*, vol. 53, no. 89, pp. 12120–12123, 2017.

[104] L. Danos, N. R. Halcovitch, B. Wood, H. Banks, M. P. Coogan, N. Alderman, L. Fang, B. Dzurnak, and T. Markvart, "Silicon photosensitisation using molecular layers," *Faraday Discussions*, vol. 222, pp. 405–423, 2020.

[105] E. Mutlugun, I. M. Soganci, and H. V. Demir, "Photovoltaic nanocrystal scintillators hybridized on Si solar cells for enhanced conversion efficiency in UV," *Optics Express*, vol. 16, no. 6, p. 3537, 2008.

[106] B. Güzeltürk, E. Mutlugün, X. Wang, K. L. Pey, and H. V. Demir, "Photovoltaic nanopillar radial junction diode architecture enhanced by integrating semiconductor quantum dot nanocrystals as light harvesters," *Applied Physics Letters*, vol. 97, no. 9, p. 093111, 2010.

[107] X. Fan, W. Zheng, and D. J. Singh, "Light scattering and surface plasmons on small spherical particles," *Light: Science and Applications*, vol. 3, p. e179, 2014.

[108] C. Bohren and D. Huffman, *Absorption and Scattering of Light by Small Particles*. John Wiley & Sons, Inc, 1998.

[109] G. Mie, "Beiträge zur Optik trüber Medien, speziell kolloidaler Metallösungen," *Annalen der Physik*, vol. 330, pp. 377–445, 1908.

[110] M. Wahl, "Modern TCSPC Electronics: Principles and Acquisition Modes," in *Advanced Photon Counting. Springer Series on Fluorescence (Methods and Applications)* (P. Kapusta, M. Wahl, and R. Erdmann, eds.), Springer, 2015.

[111] M. Olutas, B. Guzelturk, Y. Kelestemur, K. Gungor, and H. V. Demir, "Highly Efficient Nonradiative Energy Transfer from Colloidal Semiconductor Quantum Dots to Wells for Sensitive Noncontact Temperature Probing," *Advanced Functional Materials*, vol. 26, no. 17, pp. 2891–2899, 2016.

[112] R. M. Clegg, "Fluorescence resonance energy transfer," *Current opinion in biotechnology*, vol. 6, no. 1, pp. 103–110, 1995.

[113] A. L. Rogach, "Fluorescence energy transfer in hybrid structures of semiconductor nanocrystals," *Nano Today*, vol. 6, no. 4, pp. 355–365, 2011.

[114] X. Liu and J. Qiu, "Recent advances in energy transfer in bulk and nanoscale luminescent materials: From spectroscopy to applications," *Chemical Society Reviews*, vol. 44, no. 23, pp. 8714–8746, 2015.

[115] S. Ithurria and B. Dubertret, "Quasi 2D colloidal CdSe platelets with thicknesses controlled at the atomic level," *Journal of the American Chemical Society*, vol. 130, no. 49, pp. 16504–16505, 2008.

[116] S. Ithurria, G. Bousquet, and B. Dubertret, "Continuous transition from 3D to 1D confinement observed during the formation of CdSe nanoplatelets," *Journal of the American Chemical Society*, vol. 133, no. 9, pp. 3070–3077, 2011.

[117] H. Halim, J. Simon, I. Lieberwirth, V. Mailänder, K. Koynov, and A. Riedinger, "Water-dispersed semiconductor nanoplatelets with high fluorescence brightness, chemical and colloidal stability," *Journal of Materials Chemistry B*, vol. 8, no. 1, pp. 146–154, 2020.

[118] A. W. Achtstein, A. Antanovich, A. Prudnikau, R. Scott, U. Woggon, and M. Artemyev, "Linear Absorption in CdSe Nanoplates: Thickness and Lateral Size Dependency of the Intrinsic Absorption," *Journal of Physical Chemistry C*, vol. 119, no. 34, pp. 20156–20161, 2015.

[119] E. Lhuillier, S. Pedetti, S. Ithurria, B. Nadal, H. Heuclin, and B. Dubertret, "Two-Dimensional colloidal metal chalcogenides semiconductors: Synthesis, spectroscopy, and applications," *Accounts of Chemical Research*, vol. 48, no. 1, pp. 22–30, 2015.

[120] L. Gaudreau, K. J. Tielrooij, G. E. D. K. Prawiroatmodjo, J. Osmond, F. J. G. De Abajo, and F. H. L. Koppens, "Universal distance-scaling of nonradiative energy transfer to graphene," *Nano Letters*, vol. 13, no. 5, pp. 2030–2035, 2013.

[121] L. Fang, K. S. Kiang, N. P. Alderman, L. Danos, and T. Markvart, "Photon tunneling into a single-mode planar silicon waveguide," *Optics Express*, vol. 23, no. 24, p. A1528, 2015.

[122] O. Erdem, S. Foroutan, N. Gheshlaghi, B. Guzelturk, Y. Altintas, and H. V. Demir, "Thickness-Tunable Self-Assembled Colloidal Nanoplatelet Films Enable Ultrathin Optical Gain Media," *Nano Letters*, vol. 20, no. 9, pp. 6459–6465, 2020.

[123] Y. Altintas, K. Gungor, Y. Gao, M. Sak, U. Quliyeva, G. Bappi, E. Mutlugun, E. H. Sargent, and H. V. Demir, "Giant Alloyed Hot Injection Shells Enable Ultralow Optical Gain Threshold in Colloidal Quantum Wells," *ACS Nano*, vol. 13, no. 9, pp. 10662–10670, 2019.

[124] V. M. Agranovich, Y. N. Gartstein, and M. Litinskaya, "Hybrid resonant organic-inorganic nanostructures for optoelectronic applications," *Chemical Reviews*, vol. 111, no. 9, pp. 5179–5214, 2011.

[125] P. L. Hernández-Martínez and A. O. Govorov, "Exciton energy transfer between nanoparticles and nanowires," *Physical Review B - Condensed Matter and Materials Physics*, vol. 78, no. 3, p. 035314, 2008.

[126] V. M. Agranovich, G. C. La Rocca, and F. Bassani, "Efficient electronic energy transfer from a semiconductor quantum well to an organic material," *Journal of Experimental and Theoretical Physics Letters*, vol. 66, no. 11, pp. 748–751, 1997.

[127] A. O. Govorov, J. Lee, and N. A. Kotov, "Theory of plasmon-enhanced Förster energy transfer in optically excited semiconductor and metal nanoparticles," *Physical Review B*, vol. 76, no. 12, p. 125308, 2007.

[128] D. E. Aspnes and A. A. Studna, "Dielectric functions and optical parameters of Si, Ge, GaP, GaAs, GaSb, InP, InAs, and InSb from 1.5 to 6.0 eV," *Physical Review B*, vol. 27, no. 2, p. 985, 1983.

[129] R. R. Chance, A. Prock, and R. Silbey, "Comments on the classical theory of energy transfer. II. Extension to higher multipoles and anisotropic media," *The Journal of Chemical Physics*, vol. 65, no. 7, pp. 2527–2531, 1976.

[130] C. Sauvan, J. P. Hugonin, I. S. Maksymov, and P. Lalanne, "Theory of the spontaneous optical emission of nanosize photonic and plasmon resonators," *Physical Review Letters*, vol. 110, no. 23, p. 237401, 2013.

[131] S. V. Gaponenko and H. V. Demir, *Applied nanophotonics*. Cambridge University Press, 2018.

[132] S. I. Bozhevolnyi and J. B. Khurgin, "Fundamental limitations in spontaneous emission rate of single-photon sources," *Optica*, vol. 3, no. 12, p. 1418, 2016.

[133] S. Kumar, C. Wu, D. Komisar, Y. Kan, L. F. Kulikova, V. A. Davydov, V. N. Agafonov, and S. I. Bozhevolnyi, "Fluorescence enhancement of a single germanium vacancy center in a nanodiamond by a plasmonic Bragg cavity," *Journal of Chemical Physics*, vol. 154, no. 4, p. 044303, 2021.

[134] M. S. Tame, K. R. McEnery, . K. Özdemir, J. Lee, S. A. Maier, and M. S. Kim, "Quantum plasmonics," *Nature Physics*, vol. 9, no. 6, pp. 329–340, 2013.

[135] F. Wang and Y. R. Shen, "General properties of local plasmons in metal nanostructures," *Physical Review Letters*, vol. 97, no. 20, p. 206806, 2006.

[136] J. A. Schuller, E. S. Barnard, W. Cai, Y. C. Jun, J. S. White, and M. L. Brongersma, "Plasmonics for extreme light concentration and manipulation," *Nature Materials*, vol. 9, no. 3, pp. 193–204, 2010.

[137] Sudheer, P. Mondal, V. N. Rai, and A. K. Srivastava, "A study of growth and thermal dewetting behavior of ultra-thin gold films using transmission electron microscopy," *AIP Advances*, vol. 7, no. 7, p. 075303, 2017.

[138] N. H. T. Tran, K. T. L. Trinh, J. H. Lee, W. J. Yoon, and H. Ju, "Reproducible Enhancement of Fluorescence by Bimetal Mediated Surface Plasmon Coupled Emission for Highly Sensitive Quantitative Diagnosis of Double-Stranded DNA," *Small*, vol. 14, no. 32, p. 1801385, 2018.

[139] K. Aslan, Z. Leonenko, J. R. Lakowicz, and C. D. Geddes, "Annealed silver-island films for applications in metal-enhanced fluorescence: Interpretation in terms of radiating plasmons," *Journal of Fluorescence*, vol. 15, no. 5, pp. 643–654, 2005.

[140] J. Zhang, E. Matveeva, I. Gryczynski, Z. Leonenko, and J. R. Lakowicz, "Metal-enhanced fluoroimmunoassay on a silver film by vapor deposition," *Journal of Physical Chemistry B*, vol. 109, no. 16, pp. 7969–7975, 2005.

[141] E. Klantsataya, A. François, H. Ebendorff-Heidepriem, B. Sciacca, A. Zuber, and T. M. Monro, "Effect of surface roughness on metal enhanced fluorescence in planar substrates and optical fibers," *Optical Materials Express*, vol. 6, no. 6, pp. 2128–2138, 2016.

[142] S. V. Gaponenko, *Introduction to Nanophotonics*. Cambridge University Press, 2010.

[143] P. Royer, J. P. Goudonnet, R. J. Warmack, and T. L. Ferrell, "Substrate effects on surface-plasmon spectra in metal-island films," *Physical Review B*, vol. 35, no. 8, p. 3753, 1987.

[144] K. Jia, J.-L. Bijeon, P.-M. Adam, and R. E. Ionescu, "Large Scale Fabrication of Gold Nano-Structured Substrates Via High Temperature Annealing and Their Direct Use for the LSPR Detection of Atrazine," *Plasmonics*, vol. 8, no. 1, pp. 143–151, 2013.

[145] K. Grochowska, K. Siuzdak, J. Karczewski, M. Szkoda, and G. Śliwiński, "Properties of Thermally Dewetted Thin Au Films on ITO-Coated Glass for Biosensing Applications," *Plasmonics*, vol. 12, no. 6, pp. 1939–1946, 2017.

[146] R. J. Warmack and S. L. Humphrey, "Observation of two surface-plasmon modes on gold particles," *Physical Review B*, vol. 34, no. 4, p. 2246, 1986.

[147] N. Kaiser, "Review of the fundamentals of thin-film growth," *Applied Optics*, vol. 41, no. 16, pp. 3053–3060, 2002.

[148] E. Thouti, N. Chander, V. Dutta, and V. K. Komarala, "Optical properties of Ag nanoparticle layers deposited on silicon substrates," *Journal of Optics (United Kingdom)*, vol. 15, no. 3, p. 035005, 2013.

[149] T. Chung, Y. Lee, M.-S. Ahn, W. Lee, S.-I. Bae, C. S. H. Hwang, and K.-H. Jeong, "Nanoislands as plasmonic materials," *Nanoscale*, vol. 11, no. 18, pp. 8651–8664, 2019.

[150] S. Badilescu, D. Raju, S. Bathini, and M. Packirisamy, "Gold nano-island platforms for localized surface plasmon resonance sensing: A short review," *Molecules*, vol. 25, no. 20, p. 4661, 2020.

[151] P. Potejanasak and S. Duangchan, "Gold Nanoisland Agglomeration upon the Substrate Assisted Chemical Etching Based on Thermal Annealing Process," *Crystals*, vol. 10, p. 533, 2020.

[152] W. M. Abbott, S. Corbett, G. Cunningham, A. Petford-Long, S. Zhang, J. F. Donegan, and D. McCloskey, "Solid state dewetting of thin plasmonic

films under focused cw-laser irradiation," *Acta Materialia*, vol. 145, pp. 210–219, 2018.

[153] A. B. Tesler, B. M. Maoz, Y. Feldman, A. Vaskevich, and I. Rubinstein, "Solid-state thermal dewetting of just-percolated gold films evaporated on glass: Development of the morphology and optical properties," *Journal of Physical Chemistry C*, vol. 117, no. 21, pp. 11337–11346, 2013.

[154] T. Karakouz, B. M. Maoz, G. Lando, A. Vaskevich, and I. Rubinstein, "Stabilization of gold nanoparticle films on glass by thermal embedding," *ACS Applied Materials and Interfaces*, vol. 3, no. 4, pp. 978–987, 2011.

[155] M. Lončarić, J. Sancho-Parramon, H. Zorc, S. Šegota, P. Dubček, and S. Bernstorff, "Optical and structural characterization of gold island films on glass substrates," *Thin Solid Films*, vol. 591, pp. 204–209, 2015.

[156] A. G. Al-Rubaye, A. Nabok, and A. Tsargorodska, "Spectroscopic ellipsometry study of gold nanostructures for LSPR bio-sensing applications," *Sensing and Bio-Sensing Research*, vol. 12, pp. 30–35, 2017.

[157] O. Kulakovich, N. Strekal, A. Yaroshevich, S. Maskevich, S. Gaponenko, I. Nabiev, U. Woggon, and M. Artemyev, "Enhanced Luminescence of CdSe Quantum Dots on Gold Colloids," *Nano Letters*, vol. 2, no. 12, pp. 1449–1452, 2002.

[158] J. H. Song, T. Atay, S. Shi, H. Urabe, and A. V. Nurmikko, "Large enhancement of fluorescence efficiency from CdSe/ZnS quantum dots induced by resonant coupling to spatially controlled surface plasmons," *Nano Letters*, vol. 5, no. 8, pp. 1557–1561, 2005.

[159] Y.-H. Chan, J. Chen, S. E. Wark, S. L. Skiles, D. H. Son, and J. D. Batteas, "Using patterned arrays of metal nanoparticles to probe plasmon enhanced luminescence of CdSe quantum dots," *ACS Nano*, vol. 3, no. 7, pp. 1735–1744, 2009.

[160] Y. Wang, Y. Jin, T. Zhang, Z. Huang, H. Yang, J. Wang, K. Jiang, S. Fan, and Q. Li, "Emission Enhancement from CdSe/ZnS Quantum Dots Induced by Strong Localized Surface Plasmonic Resonances without Damping," *Journal of Physical Chemistry Letters*, vol. 10, no. 9, pp. 2113–2120, 2019.

[161] Y. Zhai, Q. Wang, Z. Qi, C. Li, J. Xia, and X. Li, "Experimental investigation of energy transfer between CdSe/ZnS quantum dots and different-sized gold nanoparticles," *Physica E: Low-Dimensional Systems and Nanostructures*, vol. 88, pp. 109–114, 2017.

[162] I. Shlesinger, H. Monin, J. Moreau, J.-P. Hugonin, M. Dufour, S. Ithurria, B. Vest, and J.-J. Greffet, "Strong Coupling of Nanoplatelets and Surface Plasmons on a Gold Surface," *ACS Photonics*, vol. 6, no. 11, pp. 2643–2648, 2019.

[163] J. M. Winkler, F. T. Rabouw, A. A. Rossinelli, S. V. Jayanti, K. M. McPeak, D. K. Kim, B. Le Feber, F. Prins, and D. J. Norris, "Room-Temperature Strong Coupling of CdSe Nanoplatelets and Plasmonic Hole Arrays," *Nano Letters*, vol. 19, no. 1, pp. 108–115, 2019.

[164] X. Zhang, J. Zhang, H. Wang, Y. Hao, X. Zhang, T. Wang, Y. Wang, R. Zhao, H. Zhang, and B. Yang, "Thermal-induced surface plasmon band shift of gold nanoparticle monolayer: Morphology and refractive index sensitivity," *Nanotechnology*, vol. 21, no. 46, p. 465702, 2010.

[165] H. Sun, M. Yu, G. Wang, X. Sun, and J. Lian, "Temperature-dependent morphology evolution and surface plasmon absorption of ultrathin gold island films," *Journal of Physical Chemistry C*, vol. 116, no. 16, pp. 9000–9008, 2012.

[166] B. Chen, M. Mokume, C. Liu, and K. Hayashi, "Structure and localized surface plasmon tuning of sputtered Au nano-islands through thermal annealing," *Vacuum*, vol. 110, pp. 94–101, 2014.

[167] F. Bonnie, M. D. Arnold, G. B. Smith, and A. R. Gentle, "Modes of interaction between nanostructured metal and a conducting mirror as a function

of separation and incident polarization," *Nanostructured Thin Films VI*, vol. 8818, p. 881809, 2013.

[168] K. Munechika, Y. Chen, A. F. Tillack, A. P. Kulkarni, I. J.-L. Plante, A. M. Munro, and D. S. Ginger, "Spectral control of plasmonic emission enhancement from quantum dots near single silver nanoprisms," *Nano Letters*, vol. 10, no. 7, pp. 2598–2603, 2010.

[169] V. Krivenkov, P. Samokhvalov, I. Nabiev, and Y. P. Rakovich, "Synergy of excitation enhancement and the purcell effect for strong photoluminescence enhancement in a thin-film hybrid structure based on quantum dots and plasmon nanoparticles," *Journal of Physical Chemistry Letters*, vol. 11, no. 19, pp. 8018–8025, 2020.

[170] D. V. Guzatov and V. V. Klimov, "Radiative decay engineering by triaxial nanoellipsoids," *Chemical Physics Letters*, vol. 412, no. 4-6, pp. 341–346, 2005.